

Ivan David Rojas Castro

# Design of a 10MW Wind Turbine Rotor Blade for Testing of a Scaled-down Floating Offshore Support Structure

# Design of a 10MW Wind Turbine Rotor Blade for Testing of a Scaled-down Floating Offshore Support Structure

By

Ivan David Rojas Castro

in partial fulfilment of the requirements for the degree of

**Master of Science**  
in Sustainable Energy Technology

of the Faculty of Electrical Engineering Mathematics, and Computer Science  
at the Delft University of Technology,  
to be defended publicly on October 25, 2017 at 02:00 PM,  
at the Faculty of Aerospace Engineering (Wind Energy Research Group).

Supervisors:	Dr.ir. A.C. (Axelle) Viré	TU Delft
	Ir. T.J. (John) Huisman	MARIN
Thesis committee:	Prof. dr. G.J.W. (Gerard) van Bussel	TU Delft
	Prof. dr. A.P. (Riaan) van 't Veer	TU Delft
	Dr.ir. M. (Matteo) Pini	TU Delft

Cover photo: Retrieved from DNV GL [1]

An electronic version of this thesis is available at <http://repository.tudelft.nl/>.



# Abstract

The main goal of this Master's thesis is to develop a reliable methodology that renders in the design of a scaled-down thrust-matched 10MW wind turbine rotor blade, for its further implementation in the testing of a floating offshore support structure.

Floating offshore wind energy has been drawing attention for the past two decades due to its ability to offer access to exceptional wind resources available far-offshore, where deeper waters are often encountered. For this reason, floating foundations are continuously under improvement, given the increase in size of the offshore wind turbines, which entails the need to test their behaviour under the expected operating conditions. However, doing so at large-scale is costly and time-consuming. Therefore, developers of the floating structures have turned to model-scale testing as the most suitable option for this purpose, before moving into a construction stage. These are generally carried out in a wind/wave tank, and for that, MARIN (Maritime Research Institute Netherlands) has been involved in several projects of this nature.

For a particular testing campaign to be successful, it is necessary to guarantee that the structure is accurately loaded by wind, waves and sea currents, which effectively determine its performance. Therefore, the final purpose of this work is to design a wind turbine rotor blade, that when mounted onto a rotating hub, reproduces the scaled-down thrust aerodynamic force of the DTU 10MW Reference Wind Turbine. This is due to the fact that the thrust is responsible for a large fraction of the overturning moment of the floating device.

Nevertheless, down-scaling in a floating setting brings some challenges, represented by the so-called Reynolds effects, which degrade the aerodynamic performance when the Froude-based approach is implemented. Additionally, when the rotor blades are rotating, the surrounding air tends to flow towards the blade root and tip, rendering in a 3-D flow that induces stall delay and anticipation, which modifies the aerodynamic behaviour of individual aerofoils. Likewise, the motions of the floating platform have an effect on the aerodynamics, given the sudden change in the angle of attack. All of the above, in addition to the common industry practices, are addressed and taken into consideration for the aerodynamic design.

For that purpose, a design methodology is implemented that integrates several design tools oriented to perform BEMT (Blade Element Momentum Theory) calculations, with the aim of predicting the aerodynamic performance of the turbine. This tool comprises RFOIL for incorporating the rotational effects into the aerofoil analysis; AirfoilPrep for extrapolating the aerodynamic coefficients to a more complete range; FAST to perform the BEMT computations; and PropArt (developed by MARIN) to optimise with the use of a Non-dominated Sorting Genetic Algorithm (NSGA-II) and handle the geometry over several iterations. In addition, the resulting performance is validated with ReFRESKO (MARIN's in-house CFD-3-D code).

From these BEMT-based optimisations, four blade geometries are obtained yielding from the combination of scenarios, in which either only thrust is matched or both thrust and power are considered, and whether the optimisation only considers chord and twist or thickness as well. The performance of the geometry with the optimisation of the thrust without thickness incorporation is selected for validation. The outcome from the CFD calculation was as expected, matching the thrust and its non-dimensional coefficient.

# Acknowledgements

I would like to extend my warmest gratitude to my dear parents, who have always been there for me with their love, thoughtful words and support, and who have always been proud of my accomplishments. I owe them everything that I am.

I remember carrying out my internship at 2-B Energy, when I got in touch with Dr.ir. Axelle Viré seeking for a graduation project related to offshore wind support structures. Since I already had held conversations with MARIN regarding a thesis topic, it all came together easily when she suggested working with them on floating wind turbines, given their vast experience on the subject. For making it possible, for her trust, and for her valuable insights on wind turbine design, I am always grateful.

In addition, I would like to express my gratitude towards my daily supervisor at MARIN, Ir. John Huisman, who took this project from the beginning as his own and supported me with the implementations of PropArt and ReFRESCO. Without his guidance, support, critical views and insights during our weekly meetings this work would not have been possible.

Special thanks go to the Wind Energy Research Group at TU Delft (Prof. Gerard, Dr. Michiel, Sylvia, Ir. Nando, Dr. Wim, Ir. Sebastián, Dr. René and Ir. Delphine) for hosting this thesis, for sharing the passion in Wind Energy, for all the help and support. I would also like to thank Prof. Alvaro Pinilla for his valuable support and endorsement.

Moreover, my gratitude goes to MARIN (Erik-Jan, Sebastien, Guilherme, Patrick, Joost, Menno and Simon) for providing me with the proper tools, support, feedback and enjoyable working environment. Likewise, I would like to thank my fellow students of rooms 6.08 (at the Wind Energy Department of TU Delft) and 2.26 (at the Offshore Department of MARIN) for helping me understand the use of some tools, for the lunches and for the memories.

During this 2-year journey in Delft, I was given the opportunity to meet wonderful people, from whom I learned a lot. To them, who I consider my dear friends, thank you for being there for me. In addition, I am very grateful to Mariana, who from the distance kept me motivated and encouraged me to go on. Furthermore, I would like to thank my family for following my achievements. And last, but by no means least, thank you God for bringing me to The Netherlands to pursue this dream and for taking me back home safe to start a new chapter.

*Ivan David Rojas Castro  
Delft, October 2017*

# Contents

Abstract.....	i
Acknowledgements .....	ii
Contents.....	iii
List of Tables.....	v
List of Figures.....	vi
Glossary.....	ix
1 Introduction.....	1
1.1 Motivation.....	1
1.2 Problem definition .....	3
1.3 Research Objectives .....	4
1.4 Report Outline .....	5
2 Theoretical Background.....	7
2.1 Scaling methodologies .....	7
2.1.1 Wind tunnel-oriented .....	7
2.1.2 Froude-scaling .....	8
2.1.3 Scaling effects.....	8
2.1.4 Politecnico di Milano .....	9
2.1.5 Aerodynamic Scaling.....	9
2.1.6 Final Remark.....	10
2.2 Aerodynamics of Wind Turbine Rotor Design.....	10
2.2.1 Blade Element Momentum Theory .....	10
2.2.2 Rotational Effects and Stall Delay .....	15
2.3 Impact of Floating Dynamics on Aerodynamic Design.....	18
2.3.1 Floating platform motions .....	18
2.3.2 Aerodynamic Effects of Floating Dynamics .....	18
3 Benchmark study on Model-scale Blade Design .....	21
3.1 Rotor designs.....	21
3.1.1 University of Maine.....	21
3.1.2 MARIN Stock Wind Turbine.....	24
3.1.3 Politecnico di Milano .....	27
3.1.4 DTU Wind .....	30
3.2 Testing methods.....	33
3.2.1 Wind / Wave Basin .....	33
3.2.2 Politecnico di Milano – Wind Tunnel.....	35
3.2.3 Technical University of Munich – Upward Moorings .....	36
3.2.4 Ideol - Drag Disc .....	36
3.2.5 CENER - Ducted fan .....	37
3.2.6 IHC – Multi-fan .....	39
3.2.7 MARIN - Winch-controlled.....	39
3.2.8 Final Remark.....	40
4 Methodology for Rotor Blade Design .....	41
4.1 Problem Definition and Optimisation Model.....	41
4.2 Design Procedure .....	42
4.3 Design Tools .....	43
4.3.1 RFOIL .....	44
4.3.2 AirfoilPrep .....	46
4.3.3 FAST.....	48
4.3.4 PropArt.....	50
4.3.5 Integrated Design Tool.....	53
4.4 Tools for Design Check .....	56
4.4.1 Rhinoceros.....	56

4.4.2	HEXPRESS .....	57
4.4.3	ReFRESHCO 3-D .....	57
4.4.4	Tecplot & Paraview .....	58
4.4.5	Validation of the Tools for Design Check.....	58
5	Model-scale Rotor Blade Development.....	63
5.1	Design Constraints .....	63
5.2	Design Inputs and Assumptions .....	63
5.2.1	Geometry .....	63
5.2.2	Environmental Conditions .....	67
5.2.3	Simulation Parameters .....	69
5.3	Validation Inputs.....	73
5.3.1	Geometry .....	73
5.3.2	Computational Domain.....	73
5.3.3	Grid Refinement .....	74
5.3.4	CFD Calculation Parameters.....	75
6	Optimal Model-scale Rotor Blade Geometry: Results and Discussion .....	77
6.1	Geometries Generated with the Integrated Design Tool .....	77
6.1.1	Blade Geometry No. 1.....	77
6.1.2	Blade Geometry No. 2.....	80
6.1.3	Blade Geometry No. 3.....	82
6.1.4	Blade Geometry No. 4.....	84
6.1.5	Selection of Optimal Blade Geometry.....	86
6.2	Validation of Selected Blade Geometry .....	87
7	Conclusions and Recommendations.....	91
7.1	Concluding Remarks .....	91
7.1.1	Theoretical Objectives .....	91
7.1.2	Practical Objectives.....	91
7.1.3	Design Objectives .....	92
7.2	Recommendations for future research .....	93
	Bibliography .....	95
	Appendix A Figures Full-Scale CFD Pre- & Post-processing .....	101
	Preprocessing with HEXPRESS .....	101
	Meshing of the Domain and Viscous Layer .....	101
	Meshing of the Blades .....	103
	Post-processing with Tecplot.....	103
	Flow over pressure and suction sides.....	103
	Flow over the blade at specific stations.....	103
	Appendix B FAST Inputs Optimisation.....	105
	Appendix C RFOIL Actions.....	107
	Appendix D FAST Input Files .....	109
	FAST v8.12 General Input File .....	109
	FAST AeroDyn v.14.04 Input File .....	110
	FAST Aerofoil Input File.....	111
	FAST ElastoDyn Input File .....	112
	FAST InflowWind Input File .....	115

# List of Tables

Table 2.1 Froude scaling factors [12].....	8
Table 2.2 Scaling factors for Froude-scaling and Aerodynamic-scaling [16] .....	10
Table 2.3 3-D Correction models for aerofoil characteristics [22].....	17
Table 2.4 Variations in simulated aerodynamic parameters from floating with respect to onshore setting [29] .....	20
Table 3.1 Key parameters of the DTU 10 MW and the NREL 5MW Reference Wind Turbines [30, 32] .....	21
Table 4.1 Implemented Tools in the Design Loop.....	43
Table 4.2 Inboard and outboard aerofoils simulation conditions .....	45
Table 4.3 FAST validation simulation parameters.....	49
Table 4.4 Design integrated tool validation parameters .....	53
Table 4.5 Chord and twist parametrisation ranges.....	54
Table 4.6 Meshing Refinement Parameters.....	59
Table 4.7 Inflow and RNA operational parameters for full-scale CFD calculations.....	60
Table 5.1 Properties of the SG604x aerofoils series for small wind turbines [76] .....	64
Table 5.2 Aerofoil distributions for full- and model-scale.....	66
Table 5.3 Blade Chord and twist parametrisation for model-scale .....	66
Table 5.4 Ncrit based on testing ambient condition [79] .....	70
Table 5.5 Outcomes grid refinement study for MSWT [70] .....	74
Table 5.6 Inflow and RNA operational parameters for model-scale CFD calculations.....	75
Table 5.7 Convergence parameters for CFD calculations.....	75
Table 6.1 Blade geometries from integrated design tool .....	77
Table 6.2 Description selected blade geometry .....	86

# List of Figures

Figure 1.1 Types of Offshore Wind Support Structures [7].....	2
Figure 1.2 Sources of loading acting on Floating Offshore Wind Turbines [10].....	3
Figure 2.1 Scheme of rotor analysis as an actuator disc [18].....	12
Figure 2.2 Scheme Aerofoil nomenclature [18].....	12
Figure 2.3 Representation of forces on an aerofoil [18].....	13
Figure 2.4 Blade discretisation for HAWT blade element analysis [17].....	14
Figure 2.5 Vector diagram for HAWT blade element analysis [18].....	14
Figure 2.6 Lift and drag coefficients for aerofoil NACA 0012 [18].....	15
Figure 2.7 Events of stall delay [20].....	16
Figure 2.8 3-Dimensional flow over an experimental wind turbine blade [19].....	16
Figure 2.9 Degrees of Freedom of a rigid FOWT [26].....	18
Figure 2.10 Transition from windmill to propeller state during rotor wake interaction [26].....	19
Figure 2.11 Comparison of aerodynamic performance for floating vs. onshore setting for the NREL 5MW.....	20
Figure 3.1 Comparison of Power and Thrust coefficients vs. TSR for target, first & second blade design from UMaine [12].....	22
Figure 3.2 Comparison of Thrust and Power coefficients vs. TSR for target, first and third blade design from UMaine [36].....	23
Figure 3.3 Representative distributions for geo-sim blade from NREL 5MW & re-design UMaine.....	24
Figure 3.4 Geometries of the AG04 aerofoil used in the MSWT and UMaine blade designs.....	25
Figure 3.5 Representative distributions for MSWT & UMaine blade designs.....	26
Figure 3.6 Comparison of Thrust and Power coefficients vs. TSR for MSWT and NREL 5MW obtained with BEMT, CFD and testing [39].....	26
Figure 3.7 Chord and Twist Angle Distributions for “Froude-scaled” rotor [45].....	27
Figure 3.8 Comparison Aerodynamic coefficients vs. TSR for Full- and Model-scale [45].....	28
Figure 3.9 Representative Distributions for DTU 10MW (geo-sim) and PoliMi Model-scale [15].....	29
Figure 3.10 Reynolds numbers at every blade station for Full- and Model-scale [15].....	29
Figure 3.11 Comparison of Thrust coefficients vs. Wind Speed for Full- and Model-scale at different wind speed scaling factors [15].....	30
Figure 3.12 Reynolds number regime for full- and model-scale DTU 10MW 1/60.....	31
Figure 3.13 Aerofoils employed in DTU 1/60 model blade design.....	31
Figure 3.14 Representative distributions for the DTU 10MW at 1/60th and full-scale blade designs.....	32
Figure 3.15 Thrust coefficient of the 1/60th model of the DTU 10MW blade for various pitch settings [50].....	32
Figure 3.16 Side view of wind/wave basin for FOWT testing [45].....	33
Figure 3.17 Wind / Wave FOWT testing setups.....	34
Figure 3.18 Side view of MARIN’s Offshore Basin [33].....	34
Figure 3.19 Top view of MARIN’s Offshore Basin [52].....	34
Figure 3.20 Exploded view of the wind generator for FOWT Testing in the Wave Basin [35].....	34
Figure 3.21 Wind velocity as percentage of maximum and Turbulence intensity in plane at MARIN’s Offshore Basin [39].....	35
Figure 3.22 PoliMi Wind Tunnel [15].....	35
Figure 3.23 Testing model with upward ceiling moorings [16].....	36
Figure 3.24 Dynamic response full- vs. aerodynamic-scaled model [16].....	36
Figure 3.25 FOWT test setting with drag disc [53].....	37
Figure 3.26 Thrust force behaviour for a rotor- vs. a disc-based FOWT test [53].....	37
Figure 3.27 Platform motions vs. Wave frequency upon wind/wave effect [53].....	37
Figure 3.28 Ducted-fan-based FOWT test [45].....	38

Figure 3.29 Software-in-the-Loop for fan control [45] [54].....	38
Figure 3.30 Ducted-fan-based representative floating platform motions [55] .....	38
Figure 3.31 TELWIND FOWT support structure concept [56] .....	39
Figure 3.32 IHCantabria Multi-fan FOWT testing concept [56].....	39
Figure 3.33 Representation of a 6-wire winch-driven load control system [57].....	40
Figure 3.34 SIL for 6-wire winch-driven load-control system [57].....	40
Figure 4.1 Flowchart implemented for wind turbine rotor blade design for testing of FOWTs	43
Figure 4.2 Layouts of XFOIL and RFOIL analyses of the NACA 4415 aerofoil .....	44
Figure 4.3 Comparison aerodynamic coefficients for inboard and outboard aerofoils using RFOIL vs. XFOIL.....	45
Figure 4.4 Validation of RFOIL for modified Drela’s AG04 aerofoil .....	46
Figure 4.5 Validation of AirfoilPrep extrapolation feature for FFA-W3-241 aerofoil .....	47
Figure 4.6 Validation of FAST aerodynamics for the DTU 10MW .....	49
Figure 4.7 Bézier parametrisation of representative variables for DTU 10MW .....	50
Figure 4.8 Pareto-optimal front [64] .....	51
Figure 4.9 Representative distributions of the DTU 10MW in PropArt.....	51
Figure 4.10 FFA-W3 aerofoils with Gurney flaps [32] .....	52
Figure 4.11 Implemented FFA-W3 aerofoils in PropArt.....	52
Figure 4.12 DTU 10MW 3-D blade design [32] .....	52
Figure 4.13 DTU 10MW rotor blades representation using PropArt.....	52
Figure 4.14 DTU Full-scale Reynolds regime .....	54
Figure 4.15 Optimisation progression of the DTU 10MW at full-scale.....	54
Figure 4.16 Optimised Blade Geometry based on the DTU 10MW using the Integrated design tool.....	55
Figure 4.17 DTU 10MW rotor blades representation using PropArt.....	56
Figure 4.18 Visualisation of flow around MSWT and NREL 5MW rotor blades simulated with ReFRESH [42, 70].....	57
Figure 4.19 Visualisation of wake developed behind the NREL 5MW rotor simulated with ReFRESH [42, 70].....	57
Figure 4.20 DTU 10MW RNA model on Rhinoceros.....	58
Figure 4.21 DTU 10MW RNA and Cylindrical Domain meshed with HEXPRESS .....	59
Figure 4.22 Dimensionless Wall Distance for Full-scale CFD Simulations.....	60
Figure 4.23 Visualisation of flow around DTU 10MW for TSR 7.5 with Tecplot.....	61
Figure 4.24 Validation of ReFRESH vs. BEMT for the DTU 10MW.....	61
Figure 5.1 SG604x aerofoil series for HAWT application [77].....	64
Figure 5.2 Polars SG604x aerofoil series at $Re = 50,000$ .....	65
Figure 5.3 Relative thickness distribution for DTU 10MW and model-scale current design..	66
Figure 5.4 Up-scaled elliptical nozzle wind outlet area of influence [39].....	68
Figure 5.5 Wind profile at MARIN’s Offshore Basin .....	69
Figure 5.6 Model-scale Reynolds regime .....	70
Figure 5.7 Parameters for the incorporation of rotational effects at model-scale.....	70
Figure 5.8 Sensitivity Analysis on the dimensionless free-stream velocity for low-Reynolds aerofoils .....	70
Figure 5.9 Representation of AeroDyn14’s input parameters [38].....	72
Figure 5.10 Fixed control strategy DTU 10MW [32].....	72
Figure 5.11 3-D Computational Domain for CFD Calculations [70, 80] .....	74
Figure 6.1 Optimisation progression for simulation No. 1.....	78
Figure 6.2 3-D Representation of the selected rotor blade geometry from simulation No. 1.	78
Figure 6.3 Representative distributions of blade geometry No. 1.....	79
Figure 6.4 Aerodynamic performance of a rotor with blade geometry No. 1.....	79
Figure 6.5 Optimisation progression for simulation No. 2.....	80
Figure 6.6 3-D Representation of the selected rotor blade geometry from simulation No. 2.	80
Figure 6.7 Representative distributions of blade geometry No. 2.....	81
Figure 6.8 Aerodynamic performance of a rotor with blade geometry No. 2.....	81
Figure 6.9 Optimisation progression for simulation No. 3.....	82

Figure 6.10 3-D Representation of the selected rotor blade geometry from simulation No. 382  
Figure 6.11 Representative distributions of blade geometry No. 3..... 83  
Figure 6.12 Aerodynamic performance of a rotor with blade geometry No. 3..... 83  
Figure 6.13 Optimisation progression for simulation No. 4..... 84  
Figure 6.14 3-D Representation of the selected rotor blade geometry from simulation No. 484  
Figure 6.15 Representative distributions of blade geometry No. 4..... 85  
Figure 6.16 Aerodynamic performance of a rotor with blade geometry No. 4..... 85  
Figure 6.17 Dimensionless Wall Distance for Modell-scale CFD Simulations ..... 87  
Figure 6.18 Visualisation of the flow for the model-scale wind turbine at 3 TSRs..... 88  
Figure 6.19 Aerodynamic performance of Blade Geometry No. 3 and the DTU 10MW with  
ReFRESKO and RFOIL-FAST ..... 89

# Glossary

## List of Acronyms and Abbreviations

.dat	Data File Extension
.ppg	Propagate (PropArt) File Extension
.stl	Stereolithographic File Extension
.txt	Text File Extension
2-D	Two-dimensional
3-D	Three-dimensional
A.o.A.	Angle of Attack
A/S (AS)	Aktieselskab (Aksjeselskap): Danish (and Norwegian) Stock-based company
AEP	Annual Energy Production
AFM	Absolute Formulation Method
AR	Aspect Ratio
ASME	American Society of Mechanical Engineers
BEM(T)	Blade Element Momentum (Theory)
CAD	Computer-aided Design
CAE	Computer-aided Engineering
CENER	Renewable Energy Centre of Spain
CFD	Computational Fluid Dynamics
DeepCWind	Consortium of universities, non-profits, utilities, and industry leaders to consolidate the State of Maine at the USA as national leader in the Floating Offshore Wind Technology
deg	degrees
DHI	Danish Hydraulic Institute
DNV – GL	Det Norske Veritas – Germanischer Lloyd
D.o.F.	Degrees of Freedom
DOS	Disk Operating System
Dr.	Doctor
DTU	Denmark Technical University
e.g.	exempli gratia (for example)
ECN	Energy Research Centre of the Netherlands
et al	and others
EU	European Union
FAST	Fatigue, Aerodynamics, Structure and Turbulence
FOW(T)	Floating Offshore Wind (Turbine)
GVPM	Galleria del Vento Politecnico di Milano
GWEC	Global Wind Energy Council
HAWC2	Horizontal Axis Wind turbine simulation Code 2nd generation
HAWT	Horizontal Axis Wind Turbine
i.e.	id est (that is)
IEC	International Electrotechnical Commission
IEEE	Institute of Electrical and Electronics Engineers
IHC	Environmental Hydraulic Institute of the University of Cantabria in Spain
INNWIND	Programme for Innovative Wind Conversion Systems (10-20MW) For Offshore Applications
Ir.	Ingenieur
IRENA	International Renewable Energy Agency
LCoE	Levelised Cost of Energy
LHEEA	Research Laboratory in Hydrodynamics, Energetics and Atmospheric Environment of the École Centrale de Nantes in France
M.Sc.	Master of Science

MARIN	Maritime Research Institute Netherlands
MARINTEK	Norwegian Marine Technology Research Institute
MSWL	Mean Still Water Level
MSWT	MARIN Stock Wind Turbine
NACA	National Advisory Committee for Aeronautics
NASA	National Aeronautical & Space Administration
NLR	Netherlands Aerospace Centre
NREL	National Renewable Energy Laboratory
NSGA	Non-dominated Sorting Genetic Algorithm
NURBS	Non-Uniform Rational Basis Spline
OC3	Offshore Code Comparison Collaboration
OC4	Offshore Code Comparison. Collaboration Continuation
OWE	Offshore Wind Energy
p.p.	pages
PoliMi	Politecnico di Milano
rad	Radians
RANS	Reynolds-Averaged Navier Stokes Equations
ReFresco	Reliable & Fast RANS Equations (solver for) Ships (and) Constructions Offshore.
RNA	Rotor-Nacelle Assembly
RPM	Rotations per Minute
SD	Selig-Donovan
SG	Selig-Giguere
SIL	Software-in-the-Loop
SWE	Stuttgart Wind Energy research group
TLP	Tension Leg Platform
TSR	Tip Speed Ratio
TU Delft	Delft University of Technology
TUM	Technical University of Munich
UIUC	University of Illinois at Urbana-Champaign
UK	United Kingdom
UMaine	University of Maine
USA	United States of America
VACC	Viscous Solution Acceleration
VAWT	Vertical Axis Wind Turbine
VRS	Vortex Ring State
vs	versus
w/	with
wo/	without

### Latin symbols

$a$	Axial induction factor	$[-]$
$a'$	Tangential induction factor	$[-]$
$A$	Rotor area	$[m^2]$
$A, B, C$	Inflow, pressure and outflow sides of computational domain	
$A_1, A_2, B_1, B_2$	Polar extrapolation parameters	$[-]$
$a, b, d, h, n$	3-D flow correction factors	$[-]$
$B$	Number of blades	$[-]$
$c$	Chord length	$[m]$
$C_n$	Normal equivalent force coefficient	$[-]$
$C_p$	Pressure coefficient	$[-]$
$C_p$	Power coefficient	$[-]$
$C_T$	Thrust coefficient	$[-]$

$C_t$	Tangential equivalent force coefficient	[–]
$dF$	Force differential	[N]
$D$ or $F_D$	Drag Force	[N]
$f_0$	Dimensionless free-stream velocity	[–]
$f_{aero}$	Aerodynamic force output in the software-in-the-loop	[N]
$Fr$	Froude number	[–]
$F_N$	Normal projected force	[N]
$F_T$	Tangential projected force	[N]
$g$	Acceleration of Gravity	[m/s]
$k$	Reduced frequency related to flow unsteadiness	[m/s]
$K_{FA}$	Restoring force of the platform	[N]
$l$	Blade span	[m]
$L$	Characteristic length dimension	[m]
$L$ or $F_L$	Lift force	[N]
$L_2$	Norm of residuals between consecutive iterations	[–]
$L_\infty$	Norm of maximum residual between iterations	[–]
$M$	Characteristic mass dimension	[kg]
$N$	Number of discretisation nodes	[–]
$N_{crit}$	Testing condition criterion for XFOIL/RFOIL	[–]
$p$	Pressure	[Pa]
$P$	Aerodynamic power	[W] [kW] [MW] [GW]
$P, \dot{P}$	Platform response representative parameter	[–]
$Q$	Aerodynamic torque	[N · m]
$r$	Radial position	[m]
$R$	Rotor radius	[m]
$Re$	Reynolds number	[–]
$S$	Blade span	[m]
$t$	Blade thickness	[m]
$T$	Characteristic time dimension	[s]
$T$	Aerodynamic thrust force	[N] [kN]
$U$	Inflow velocity	[m/s]
$u_*$	Friction velocity near the wall	[m/s]
$V$	Characteristic velocity	[m/s]
$x$	Horizontal coordinate along the aerofoil's chordline	[m]
$x, y, z$	Coordinate axes	
$X_{FA}$	Restoring distance of the platform	[m]
$X_P$	Platform surge excursion	[m]
$x_{tr}$	Coordinate for flow transition along the aerofoil surface	[m]
$y$	Vertical coordinate of the aerofoil's locus of points	[m]
$y$	Distance to the closest wall	[m]
$y^+$	Non-dimensional wall distance	[–]
$Z_P$	Platform heave excursion	[m]

### Greek symbols

$\alpha$	Angle of attack on an aerofoil	[deg]
$\beta$ or $\theta_T$	Blade twist angle	[deg] [rad]
$\Delta$	Unidimensional variation	
$\theta_P$	Platform pitch	[deg]
$\theta_{p,0}$	Blade pitch angle	[deg]
$\theta_p$	Section pitch angle	[deg]
$\lambda$	Scaling factor	[–]

$\Lambda$	Modified non-dimensional rotation speed in Du & Selig 3-D flow correction model	$[-]$
$\mu$	Dynamic viscosity of the fluid	$[Pa \cdot s]$
$\nu$	Kinematic viscosity of the fluid	$[m^2/s]$
$\pi$	Pi number	$[-]$
$\rho$	Density of the fluid	$[kg/m^3]$
$\varphi$	Inflow angle	$[deg]$
$\omega$	Rotational speed of the wake	$[rpm]$
$\omega$	Oscillation natural frequency	$[rad/s]$
$\Omega$	Rotational speed of the rotor	$[rpm]$
		$[rad/s]$

## Subscripts

$\infty$	Upstream
<i>bottom</i>	Referent to the pressure side of the aerofoil
<i>cut – in</i>	At cut-in wind speed
<i>cut – out</i>	At cut-out wind speed
<i>F</i>	Associated with full-scale
<i>hub</i>	Related to the rotor hub
<i>i</i>	Index over the blade sections
<i>L</i>	Relative to characteristic length
<i>M</i>	Associated with model-scale
<i>max</i>	Maximum value
<i>min</i>	Minimum value
<i>n</i> and <i>n – 1</i>	Indices of the current and previous blade nodes
<i>n</i>	Normal to the rotor
<i>ptfm</i>	Related to the platform
<i>r</i>	At a certain radial position
<i>ref</i>	Reference value
<i>rel</i>	Relative
<i>t</i>	Tangential to the rotor
<i>top</i>	Referent to the suction side of the aerofoil
<i>tran</i>	In a transient state from laminar to turbulent flow
<i>turb</i>	In a turbulence flow
<i>T</i>	Relative to characteristic time dimension
<i>V</i>	Relative to characteristic velocity

# 1 Introduction

In this chapter, the introduction to this work is presented. For this purpose, in section 1.1 the reader is taken on a journey through the background of floating offshore wind energy and the cause that motivated this project. Then, the problem to be addressed is made known in section 1.2, which results in a set of objectives described in section 1.3. Finally, for meeting the aforementioned goals, the document outline is given in section 1.4.

## 1.1 Motivation

Nowadays, wind energy, and especially Offshore Wind Energy (OWE) has gained lots of attention from all types of stakeholders; it has become a green and renewable solution to the world's increasing demand for energy, which so far has been mainly supplied by fossil fuels. There are numerous advantages for its wide implementation, such as the access to better wind resources, i.e. stronger and undisturbed, thanks to the lack of obstacles at sea. As of today, the global installed capacity of offshore wind reaches 14.4 GW [2], and according to the International Renewable Energy Agency (IRENA) in its *Innovation Outlook: Offshore Wind 2016*, by 2030 this number can grow up to 100 GW [3].

One of the main challenges that the OWE industry faces is the high raw costs associated with the support structures, which are proportional to the water depth of the site for the installation of the wind turbine, and more generally the wind farm. For this reason, floating offshore wind energy (FOW) has risen as an alternative for its implementation in locations, where the seabed is more than 50 m below the Mean Still Water Level (MSWL). This is a breaking point from the feasibility side, since the cost of steel makes the Levelised Cost of Energy (LCoE) high compared to shallow-waters installations.

Furthermore, to the end of lowering the LCoE, the OWE industry has been pushing wind turbine manufacturers to increase the size of the rotors and the power generating capacity of these machines. This is to accomplish a higher energy yield per unit of area. Therefore, to date, turbines of up to 9.5 MW have been constructed, and it is expected to grow to 20 MW by 2050 as predicted by DNV-GL [1]. These large turbines require special designs of support structure, either fixed or floating, due to the high aerodynamic loads that are translated as overturning moments at the base of the structure.

Floating offshore wind poses significant advantages with respect to bottom-fixed support structures. First and most important, the quality of the wind resource is exceptional. For instance, according to Holtslag, at 20 m high, the wind speeds increase from 6 m/s onshore to 12 m/s, and at 250 m high, from 7 to 17 m/s respectively [4]. This means that larger turbines are suitable for implementation far offshore. Furthermore, many deep-water sites are located far offshore (> 30 km), which means less visual, noise and economic constraints for shore residents. On the other hand, there are significant amount of farther locations for FOW wide implementation. For instance, 2/3 of the North Sea alone has water depths larger than 50 m. Moreover, the installation is simpler and is more environment-friendly since less intervention is done to the seabed [5].

There are several concepts of foundations employed in FOW technology, which have been inherited from the Oil & Gas industry and are categorised into three types depending on their source of stability. From these, variations are derived, which pose the idea of installing multiple turbines on a single structure. The comparison between bottom-fixed and floating structures is depicted in Figure 1.1.

First, when the stability is achieved by means of pre-tensioned tethers, it is called *mooring line stabilised*. This is featured by the Tension-Leg Platform (TLP), which is positioned below the MSWL, such that the buoyancy force keeps the mooring lines tensioned, thus preserving the floating condition of the platform. There are many variants in the design of the structure itself. However, this particular type of floating support structure presents challenges during the installation since a pre-ballasting is carried out prior to installing the mooring lines. Nevertheless, the vertical motion and two rotational degrees of freedom are restrained due to the pretension of the lines, which decreases the accelerations in the nacelle.

Second, when the stability is achieved as a result of the restoring effects of buoyancy, it is called *buoyancy stabilised*. In this type, the Semi-Submersible (or Semi-Sub) is commonly encountered, of which the Barge is a derivation. This structure comprises large hulls connected with braces between each other and anchored to the seabed with catenary mooring lines. This foundation is greatly sensitive to motions when compared to the previous type since the mooring lines only restrict the degrees of freedom up to certain extent. For this reason, a dynamic ballast concept has been developed, which pumps water between hulls in order to counteract the effect of waves, resulting in more subtle motions. Nevertheless, its installation is the easiest among all three types.

Finally, an alternative option is to place a ballast in order to lower the centre of gravity of the structure to achieve stability, this is called *ballast stabilised*, and the spar-buoy falls into this category. These are long cylindrical-shaped foundations which are connected to the tower via a transition piece and are suitable for depths larger than 100 m. In principle, the spar buoy can float by itself in an upright position. Analogue to the semi-sub, it reproduces all of the 6 degrees of freedom [6].

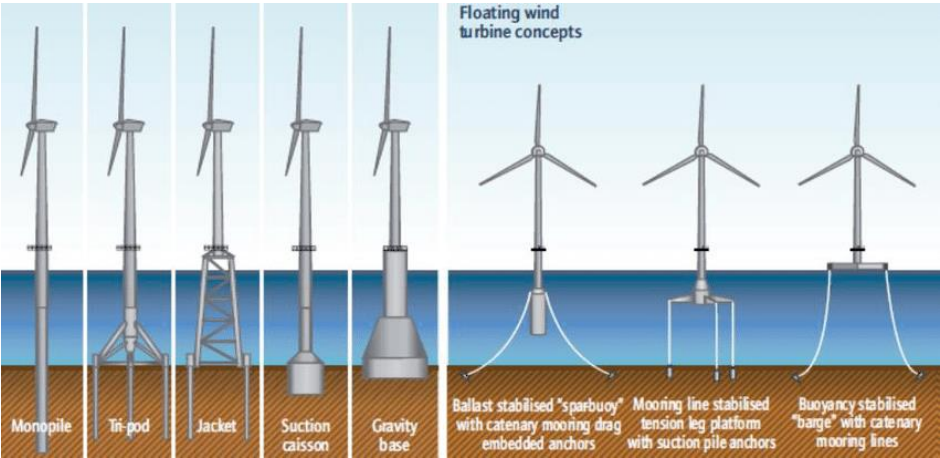


Figure 1.1 Types of Offshore Wind Support Structures [7]

Historically, floating offshore wind energy at full-scale ( $\geq 1.0$  MW) has been around since 2009, when the Hywind, a 2.3 MW spar-buoy demonstrator was placed in Norway by Statoil; its implementation opened the opportunity for other ventures. For instance, and to name a few, two years later in Portugal was installed the WindFloat, a semi-submersible with a 2.0 MW wind turbine mounted. The same year 2011, Japan deployed a 2.0 MW semi-submersible floating offshore wind turbine (FOWT) [8]. Following the trend, Japan installed a 7.0 MW turbine on top of a V-shaped semi-submersible, hence accomplishing the largest FOWT ever installed.

In addition, during the development of the present work, Statoil commissioned and began operations of the Hywind wind farm, the first of its kind, with a total installed capacity of 30 MW, powered by five 6.0 MW FOWTs, with permission to extend to 92 MW. This is the beginning for the extensive development of floating offshore wind since many new farms have

been approved. In Scotland alone, two projects of 12 and 50 MW have been granted permission to move forward. WindFloat has two wind farm projects under development of 25 and 30 MW in Portugal and USA respectively. France, on the other hand, is currently working on four pilot projects, one of which is a 24 MW wind farm to be commissioned by 2020, adding up to 237 MW of total FOW installed capacity [9]. So far, the implementation has been with Horizontal Axis Wind Turbines (HAWTs), yet it is possible to install Vertical Axis Wind Turbines (VAWTs); however, for the sake of this work only HAWTs are considered.

These large-scale implementations promote innovation, research and development of floating support structures, to the end of making this technology competitive and affordable for green energy generation. In addition, prior to placing a FOWT at sea, rigorous testing in a controlled environment is required. For this reason, several research institutes around the globe, which are specialised in hydrodynamics are constantly involved in projects in which they are asked to evaluate the performance of certain floating platform under specific conditions. The continued growth of the field and of the turbines are the main drivers of this project.

### 1.2 Problem definition

FOWTs are the subject of various sources of loading, namely wind, waves and sea currents, as depicted in Figure 1.2. For this reason, it is important to consider them thoroughly during the design stage. With regard to the floating structure, as seen before, it is sensitive to the motions resulting from the action of waves, in addition to the overturning moments generated as a consequence of wind loading on the rotor, nacelle and the tower. Therefore, prior to moving forward with the construction of full-scale FOWT platforms, manufacturers are interested in knowing the expected behaviour, when the turbine is mounted and operating.

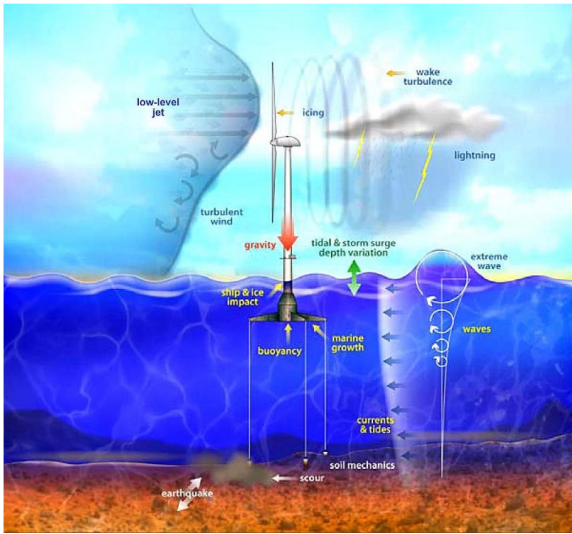


Figure 1.2 Sources of loading acting on Floating Offshore Wind Turbines [10]

Model-scale testing, in contrast to full-scale, allows to evaluate the performance of FOWTs and are significantly easier and less costly to carry out. To this end, setting the proper scaling rule is crucial for the success of the tests. In the case of floating structures, commonly the Froude approach is employed, since it scales properly the gravity-based forces, such as the ones coming from waves. Nevertheless, wind tunnels operate on a Reynolds-based approach, which poses high wind speeds. Both methods display considerable differences in the achieved testing wind speed since the Froude-based methodology yields in low values, therefore low-Reynolds numbers, degrading the aerodynamic performance of a scaled-down wind turbine rotor. These discrepancies require further study, in order to find a consistent methodology that represents well both conceptions in a wind/wave testing facility.

Furthermore, several numerical studies performed on rotating blades indicate the presence of 3-Dimensional flow, which up until now many blade design exercises and tools do not consider. This is because this involves complexities in the flow such as separation bubbles, yielding in stall delay and anticipation. Therefore, for an accurate representation of the aerodynamic performance of the blade, this issue urges further examination.

Moreover, when the FOWT moves back and forth upon the influence of wind and waves, the air flow experienced by the rotor changes and with it the instantaneous aerodynamic performance of the blade, thus resulting in unsteadiness of the surrounding flow. Hence the impact of floating dynamics on the aerodynamic design of the rotor blade is worthwhile to be investigated.

With an understanding of the above, and taking into account the design methodologies implemented by various research institutes for similar exercises, it is relevant to establish a new procedure that yields in a design of a rotor blade. This method must be adaptable to any turbine size and floating foundation topology.

Finally, the resulting blade must be able to reproduce the non-dimensional aerodynamic performance of a reference turbine accurately, for which in this case the DTU 10MW is considered, as it is the most recent. Likewise, the blade must comply with manufacturing constraints. Nonetheless, the design needs to be further validated on its performance before reaching the manufacturing and further testing stages.

### 1.3 Research Objectives

From the problems to be solved, specific research objectives are traced for this project under three categories and introduced as follows:

#### *Theoretical Objectives*

- Investigate the scaling methodologies available and find the most suitable that decreases the impact of the Reynolds effects on the wind turbine rotor blade design, when a Froude-based approach is implemented.
- Determine how important the incorporation of rotational effects into the aerodynamic performance of an aerofoil is in the wind turbine rotor blade design process.
- Establish the significance of considering the effect of floating dynamics into the aerodynamic performance of the rotor blade during the design process.

#### *Practical Objectives*

- Define a reliable methodology for carrying out the aerodynamic design of a scaled-down wind turbine rotor blade, to be used in the testing of a floating foundation in a wind/wave basin.
- Find and integrate reliable aerodynamic-based design tools capable of working together in an automated way for the purpose of designing a wind turbine rotor blade.

#### *Design Objectives*

- Determine the shape of the optimal geometry of a scaled-down wind turbine rotor blade that reproduces the non-dimensional aerodynamic performance of the full-scale DTU 10MW Reference Wind Turbine.
- Validate the aerodynamic performance of the designed wind turbine rotor blade, with the use of an alternative method.

## 1.4 Report Outline

For the purpose of meeting the aforementioned objectives, this document follows the structure indicated below:

Chapter 2 describes briefly the theory behind the design of the wind turbine rotor blade. First, several scaling methodologies are studied, and the most suitable is selected. Furthermore, the blade aerodynamic theory is investigated, contextualising into the Blade Element Momentum Theory. Then, the rotational effects and the 3-Dimensional flow are studied, and the concept of stall is examined. Finally, to conclude the theoretical questions, the impact of floating dynamics on the aerodynamic design is examined.

In chapter 3, similar model-scale blade design exercises are introduced with the purpose of getting the reader acquainted with the industry practices in this respect and to establish a starting point for the design methodology to be implemented. Moreover, these designs came along with several testing procedures, since they have been carried out in various research institutes around the world with different approaches.

Furthermore, chapter 4 treats in detail the design methodology, subjected to analysis in this work. To this end, the optimisation model is presented, which will be the driver for reproducing the non-dimensional aerodynamic performance of the baseline wind turbine. In addition, both the design (BEMT-based) and the validation tools (Computational Fluid Dynamics, CFD-based) are described, and a validation exercise is illustrated in order to establish their suitability and reliability individually and when working together.

Complementary to the previous, chapter 5 describes the inputs and constraints taken into account individually and globally for the model-scale design of the wind turbine rotor blade suitable for this particular application. Likewise, the same is carried out for the validation tools.

Upon completion of the simulations run with the integration of the design tools, in chapter 6 four blade geometries are studied, and the most appropriate is selected, in order to be validated. This geometry is then analysed with MARIN's in-house CFD code, yielding in an aerodynamic response, which is further compared with the one obtained via BEMT.

Finally, chapter 7 displays the concluding remarks on all related to this work, and recommendations are provided in order to be taken into account for future design exercises of this type.

## 2 Theoretical Background

In this chapter, the reader is presented with the theory necessary to understand the rotor design methodology to be further proposed and implemented. As indicated in chapter 1, when Reynolds-scaled turbines are tested in wind/wave basins, the aerodynamic performance is poor, due to the so-called scaling effects; therefore, new methodologies have been developed to cope with this, which are further introduced and assessed in section 2.1. Finally, the aerodynamics behind the rotor's performance is explained, and the effect of the floating dynamics on it is investigated in section 2.2.

### 2.1 Scaling methodologies

#### 2.1.1 Wind tunnel-oriented

Model-scale testing has proven to be an effective technique to predict the performance of a full-scale rotor or entire turbine before constructing it, given that the dimensions, and therefore the associated costs are too large to allow full-scale testing. In this sense, commonly these tests are performed in a wind tunnel setting, in which the wind inflow is controlled in order to provide the rotor with a steady and uniform flow. This wind speed is determined in a way that the Reynolds number is kept constant for both full- and model-scale, taking into account that the down-scaling of the length is linear by a factor (scale)  $\lambda$ . For example, if  $\lambda = 50$  then the model will be 50 times smaller than the full-scale turbine. Equations (2.1) - (2.3) aid in establishing the wind speed for testing purposes:

First, the widely known dimensionless Reynolds number that correlates the inertial forces and the viscous forces of Newtonian fluids follows the expression below [11]:

$$Re = \frac{\rho \cdot V \cdot L}{\mu}, \quad (2.1)$$

where  $\rho$  is the density of the fluid in which the object is immersed,  $V$  and  $L$  are the characteristic velocity and length respectively, and  $\mu$  is the fluid's dynamic viscosity. In order to determine the wind speed for the wind tunnel, the Reynolds numbers for both full- and model-scale (subscripts F and M respectively) are equated and the down-scaled length is re-defined.

$$V_M \cdot L_M = V_M \cdot \left(\frac{L_F}{\lambda}\right) = V_F \cdot L_F \quad (2.2)$$

As it is evident in the following equation, it is taken into account that since the fluid is the same (air), its properties are cancelled out.

$$V_M = V_F \cdot \lambda \quad (2.3)$$

The result is that the wind tunnel model should experience a wind velocity  $\lambda$  times larger. This is appropriate if  $\lambda$  is such that the capabilities of the wind tunnel are not exceeded and when only the aerodynamic performance is of interest. However, since the turbine subjected to study in this work is placed onto a floating platform, which means that wave-induced motions have a significant governing effect on the platform's behaviour, these need to be taken into account. For this reason, the following scaling methodology is introduced: the basin-oriented or so-called Froude-scaling.

### 2.1.2 Froude-scaling

This methodology is named after the dimensionless parameter - the Froude number – defined by equation (2.4) that correlates inertial with gravity-driven forces, such as the ones from waves of free-surface flows. Hence, it is used for hydraulic model testing of elements floating in a free-surface fluid in motion [11].

$$Fr = \frac{V}{\sqrt{g \cdot L}} \quad (2.4)$$

with  $g$  being the gravity acceleration constant. As expected, the principle behind the similitude is to keep the dimensionless number constant. Therefore, similar to the procedure followed in section 2.1.1 for the Reynolds-scaling, it is possible to find the wind speed to be experienced at the wind/wave basin, as shown by equations (2.5) and (2.6):

$$\frac{V_M}{\sqrt{g \cdot L_M}} = \frac{V_M}{\sqrt{g \cdot \left(\frac{L_F}{\lambda}\right)}} = \frac{V_F}{\sqrt{g \cdot L_F}} \quad (2.5)$$

$$V_M = \frac{V_F}{\sqrt{\lambda}} \quad (2.6)$$

Consequently, many other variables can be scaled accordingly as shown in Table 2.1:

Table 2.1 Froude scaling factors [12]

Variable	Dimensions	Scale Factor
Area	$L^2$	$\lambda^2$
Volume	$L^3$	$\lambda^3$
Mass	$M$	$\lambda^3$
Time	$T$	$\lambda^{0.5}$
Frequency	$T^{-1}$	$\lambda^{-0.5}$
Acceleration	$LT^{-2}$	1
Force	$MLT^{-2}$	$\lambda^3$
Moment	$ML^2T^{-2}$	$\lambda^4$
Power	$ML^2T^{-3}$	$\lambda^{3.5}$
Mass moment of inertia	$ML^2$	$\lambda^5$
Area moment of inertia	$L^4$	$\lambda^4$

### 2.1.3 Scaling effects

When down-scaling a rotor for testing purposes, three scaling laws must be satisfied in order to ensure complete aerodynamic similarity; these are: geometric, kinematic and dynamic [13, 14]. The geometric similarity entails that the model dimensions are achieved based on a scale factor ( $\lambda$ ). Furthermore, the kinematic similarity is obtained when the Tip Speed Ratio (TSR), defined in the equation (2.7) is kept constant for full- and model-scale. Here  $\Omega$  is the rotational speed of the rotor,  $R$  is the radius and  $V$  is the inflow wind speed. Finally, the dynamic similarity requires the local Reynolds numbers to be maintained as well [14], in order to keep the non-dimensional performance.

$$TSR = \frac{\Omega \cdot R}{V} \quad (2.7)$$

Given the importance of incorporating the wave forces in the testing of Floating Offshore Wind Turbines (FOWT), Froude-based scaling is needed. Therefore, it is nearly impossible to satisfy all three laws simultaneously since, as opposed to the Reynolds-scaling, the wind speed is much lower. This means that the Reynolds number will also be lower than the one encountered in the full-scale operating conditions, sometimes such that a transition from turbulent to laminar flow is achieved [12]. Consequently, the mismatch in the aerodynamic performance is generally called scaling-effect. Thus, in order to cope with this, two efforts have been introduced with the purpose of scaling the wind speed in a different manner, one done by the Politecnico di Milano in Italy and the second by the Technical University of Munich (TUM) in Germany.

### 2.1.4 Politecnico di Milano

The scaling methodology proposed by Politecnico di Milano entails introducing a specific scale factor for the wind speed, lower than the one corresponding to the length ( $\lambda_V < \lambda_L$ ), making the testing wind speed higher than the Froude-scaled one. In this case, the aerodynamic loads are scaled with the factor  $\lambda_L^2 \cdot \lambda_V^2$  as seen in the following derivation:

From hydromechanics, it is known that the force ( $T$ ) acting upon a solid element, e.g. a rotor disc, of cross section area  $A$  is its product with the pressure difference  $\Delta p$  as seen in equation (2.8). The first term is proportional to  $L^2$ , whereas from the application of Bernoulli's equation, the second term is proportional to  $V^2$ . Therefore, to find the equivalent scaling factor, is necessary to take into account that the testing method is based on a wind tunnel as opposed to a wind/wave basin [15], which means that the velocity is scaled according to equation (2.3). Equation (2.9) illustrates the steps followed to determine the corresponding scaling factor, which is finally described by equation (2.10).

$$T = A\Delta p \quad (2.8)$$

$$\frac{T_F}{T_M} = \frac{L_F^2 \cdot V_F^2}{L_M^2 \cdot V_M^2} = \frac{L_F^2 \cdot V_F^2}{(L_F^2/\lambda_L^2) \cdot (V_F^2/\lambda_V^2)} = \lambda_L^2 \cdot \lambda_V^2 \quad (2.9)$$

$$T_M = \frac{T_F}{\lambda_L^2 \cdot \lambda_V^2} \quad (2.10)$$

Although this methodology would reduce the gap between the Reynolds numbers at full- and model-scale, it implies very high wind speeds, which would signify a sharp increase in the drag loads over the rotor. This is translated as a large overturning moment on the floating platform (Froude-scaled), which has not been designed for these forces, i.e. it is likely to flip over.

### 2.1.5 Aerodynamic Scaling

This alternative methodology, developed by the TUM, aims to improve aerodynamic performance of scaled-down FOWT by incorporating the platform restoring and dynamic properties. The motivation behind this proposal is that for Froude-scaled conditions, the rotors need to be subjected to substantial changes with regard to geometry in order to get closer in non-dimensional aerodynamic performance, i.e. thrust and power coefficients ( $C_T$  and  $C_P$ , respectively) to the one expected for full-scale. In this sense, the chord needs to increase for the local Reynolds numbers to grow, which consequently increases the rotor mass. However, these modifications do not improve the  $C_P$ s.

To cope with this, the time variable is assigned with a scaling factor twice of the length ( $\lambda_T = 2\lambda_L$ ). According to the authors of this approach, the chord distribution can remain unchanged, therefore allowing a proper aero-elastic scaling [16]. This scaling factor, would decrease the

Reynolds mismatch, but affect negatively the Froude-scaling of the platform, which means that even though the rotor would be suitable for both wind tunnel and wave tank tests, the platform would be too light for the environmental testing conditions, as shown in Table 2.2.

Table 2.2 Scaling factors for Froude-scaling and Aerodynamic-scaling [16]

Quantity	Froude	Aerodynamic
Reynolds	$\lambda_L^{\frac{3}{2}}$	$\frac{1}{2}\lambda_L$
Froude	1	$\frac{1}{4}\lambda_L^{-1}$
Mach	$\lambda_L^{\frac{1}{2}}$	$\frac{1}{2}$

### 2.1.6 Final Remark

In light of these methodologies, the most appropriate approach for the floating setting is to apply the Froude-scaling since it scales properly the gravity-based forces coming from waves. Consequently, the achieved wind speed is lower, which renders in the so-called scaling-effect degrading the aerodynamic performance. However, in order to compensate for the mismatch in the Reynolds regime, the blade geometry is to be modified such that the non-dimensional aerodynamic performance matches as close as possible to the one found a full-scale. For this purpose, various approaches to the design have been introduced and described in the following chapter.

## 2.2 Aerodynamics of Wind Turbine Rotor Design

In order to introduce the reader to the concepts that are further used for the aerodynamic design of (horizontal axis) wind turbine - HAWT rotor blades, in this section a brief description of the Blade Element Momentum Theory is presented with the most characteristic equations. For this purpose, the chapters concerning Aerodynamics from the Wind Energy Handbook [17] and Wind Energy Explained [18] textbooks are employed as main sources. Furthermore, since the blade design resulting from this work will be implemented in a floating setting for testing purposes, the impact of the floating dynamics on the aerodynamic design is studied.

### 2.2.1 Blade Element Momentum Theory

The Blade Element Momentum Theory (BEMT, BEM or Strip Theory referred to indistinctively in literature and further in this document) is the combination of Momentum (or Rankine-Froude) Theory and Blade Element Theory. The first is based on a one-dimensional wind flow against an actuator disc that represents the rotor plane; the purpose of this model is to obtain the thrust and therefore the power by analysing the difference in velocities upwind, at the rotor position and down wind. With the second approach, the normal and tangential forces are calculated for a discretised element of the rotor blade, which is further extrapolated to overall thrust and torque.

#### *Momentum Theory*

The principle behind this theory is the conservation of linear momentum of a particular control volume. In order to make this analysis, a number of assumptions are made: the incoming flow is homogeneous, incompressible and in steady state; there is no frictional drag; the number of blades is infinite; the thrust is uniform over the disc and the static pressures far upstream and downstream (positions 1 and 4 respectively from Figure 2.1) are equal to non-disturbed ambient static pressure.

The thrust is defined as the opposite of the net force of the wind acting on the disc, which is the difference in the change over time of the momentum between positions (1) and (4). Furthermore, with the implementation of Bernoulli's equation to find the difference  $\Delta p$  from equation (2.8), it is found that the thrust is defined as displayed by equation (2.11).

$$T = \frac{1}{2} \rho A (U_1^2 - U_4^2) \quad (2.11)$$

Now, the velocity at the rotor ( $U_2$ ) is the average of the far upstream and downstream velocities, the axial induction factor  $a$  is introduced as the fraction of the decrease in wind velocity at the rotor disc with respect to the free stream velocity ( $U$  or  $U_1$ ), as seen in equation (2.12)

$$a = \frac{U_1 - U_2}{U_1} \quad (2.12)$$

In this sense, the thrust equation is transformed into:

$$T = \frac{1}{2} \rho U^2 A 4a(1 - a), \quad (2.13)$$

which for performance assessment purposes, it is relevant to determine the non-dimensional thrust coefficient  $C_T$ , defined as:

$$C_T = \frac{T}{\frac{1}{2} \rho U^2 A} = 4a(1 - a) \quad (2.14)$$

Similarly, the aerodynamic power can be found as the product of the thrust and the velocity at the rotor disc position ( $U(1 - a)$ ). This is described by equation (2.15):

$$P = \frac{1}{2} \rho U^3 A 4a(1 - a)^2, \quad (2.15)$$

therefore, the non-dimensional parameter, power coefficient  $C_P$  is:

$$C_P = \frac{P}{\frac{1}{2} \rho U^3 A} = 4a(1 - a)^2 \quad (2.16)$$

Since the goal of full-scale turbines is to extract the maximum amount of power from the wind, then the power coefficient should be maximum. This is then achieved at an axial induction factor of  $1/3$ , giving a  $C_{P,max} = 16/27 = 0.5926$ , referred to as Betz limit in honour to its discoverer. However, in practice, factors such as the presence of aerodynamic drag, a finite number of blades, with their respective tip losses and the rotation of the wake behind the rotor lead to a decrease in the maximum aerodynamic power achievable.

Wake rotation, opposite in direction to the rotor, takes rotational kinetic energy from the rotor, which results in a lower power extraction. In this case, the angular velocity of air with respect to the one pertaining the rotor increases in the angular velocity of the wake, i.e. from  $\Omega$  to  $\Omega + \omega$ . Hence, in order to establish the amount of power lost due to the wake rotation, it is relevant to introduce the tangential induction  $a'$  factor as the half of the ratio between the wake and the rotor angular velocities, as seen in equation (2.17) below.

$$a' = \frac{\omega}{2\Omega} \quad (2.17)$$

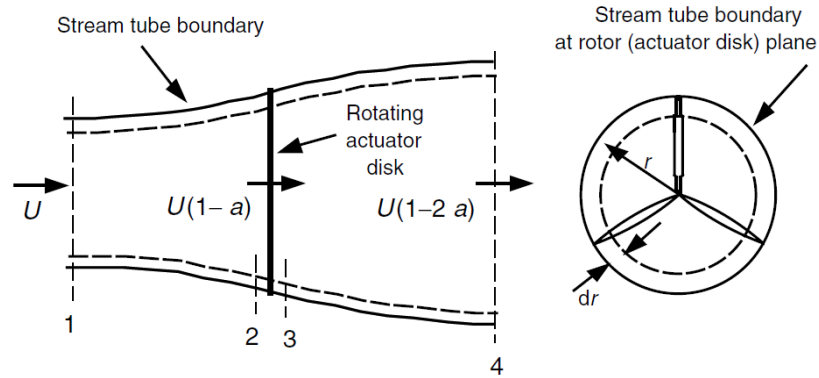


Figure 2.1 Scheme of rotor analysis as an actuator disc [18]

### Aerofoil concepts

Blade Element Theory is based on a discretisation and subsequent force analysis of a wind turbine rotor blade, whose cross section has the shape of an aerofoil, a profile intended to generate aerodynamic forces due to its motion in a surrounding fluid or vice versa. Therefore, they are essential for wind turbines to generate power. For these reasons, it is relevant to introduce general terminology and concepts of aerodynamic performance of an aerofoil, which will serve as base to understand the development within this work.

First, it is useful to introduce the terminology used to describe a particular aerofoil: terms that are self-explanatory from Figure 2.2 except the mean camber line. This latter relates to the locus of points in the middle between the pressure and the suction sides (lower and upper respectively). Camber is the distance between the mean camber and the chord lines. Hence, the higher the camber an aerofoil has the more curvature. In addition, the thickness is the distance between top and bottom surfaces. Both the camber and the thickness are measured perpendicular to the chord line [18].

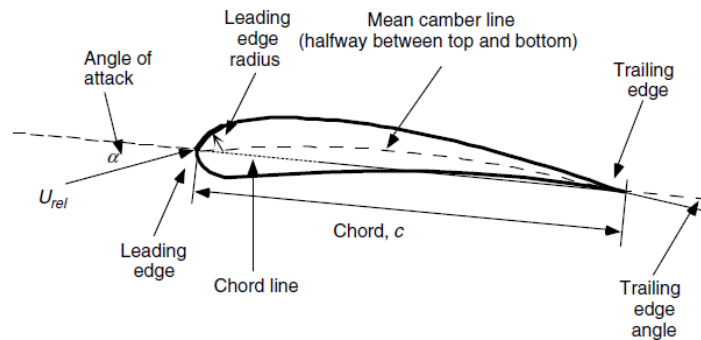


Figure 2.2 Scheme Aerofoil nomenclature [18]

As mentioned before, the main goal of aerofoils is to generate aerodynamic forces, divided into two types: lift ( $L$ ) and drag ( $D$ ), perpendicular to each other. Lift is generated by the difference in pressure of the surrounding fluid, which leads to an increase in flow velocity on the suction side; its vector is normal to the relative wind velocity. On the other hand, drag comprises two sub-types: pressure and viscous friction drag. The first, relates to the compression of air particles at the surface, and the last is caused by the surface roughness that slows down the flow. Figure 2.3 illustrates the forces generated by the aerofoil. The pitching moment displayed is not considered in this study, therefore not further explained.

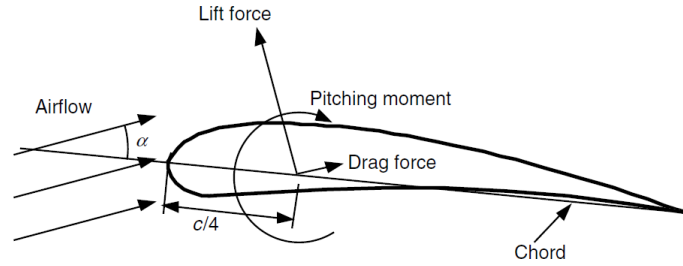


Figure 2.3 Representation of forces on an aerofoil [18]

Now, from these forces, non-dimensional parameters can be obtained for analysis purposes. These parameters are described by equations (2.18) and (2.19).

$$C_l = \frac{L/l}{\frac{1}{2}\rho U^2 c} \quad (2.18)$$

$$C_d = \frac{D/l}{\frac{1}{2}\rho U^2 c}, \quad (2.19)$$

where  $l$  is the span (length) of the aerofoil section. Further, in section 2.2.2 stall, rotational effects and post-stall aerofoil performance are introduced.

### Blade Element Theory

With these basic aerofoil concepts in mind, the aerodynamic forces generated by the aerofoil are responsible for the change in pressure observed in the actuator disc model from the Momentum Theory. In this sense, aerofoil characteristics are used to describe power extraction and thrust. Moreover, these are useful for rotor blade design purposes.

For the purpose of this study, the blade is divided in  $N$  independent elements of length span  $dr$  as displayed in Figure 2.4, with no interaction between each other. This means that there is no flow going from one to another (radial flow, further introduced in section 2.2.2). Wind makes contact with the blade section at a velocity  $U(1 - a)$  and due to the wake rotation, the blade section has an overall tangential velocity  $\Omega r(1 + a')$ . The vector sum of both gives a relative velocity, from which the Reynolds number and corresponding lift and drag are derived, depending on the aerofoil shape.

Furthermore, it is relevant to introduce the concept of local tip speed ratio ( $TSR_r$ ), which aids in understanding the aerodynamics at a particular blade section. This is presented in equation (2.20).

$$TSR_r = \frac{\Omega r}{U} = \frac{TSR \cdot r}{R} \quad (2.20)$$

Figure 2.5 illustrates the vector representation of normal and tangential induced velocities and resultant forces, and defines the quantities involved; this serves for explaining the derivation of the theory itself.

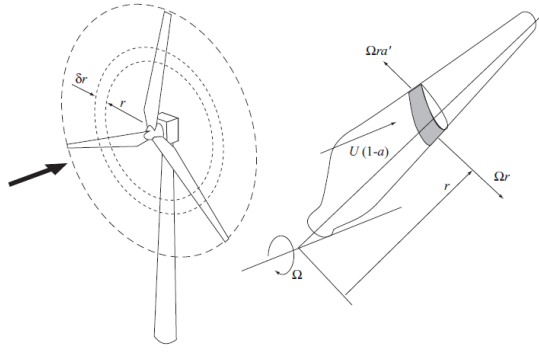


Figure 2.4 Blade discretisation for HAWT blade element analysis [17]

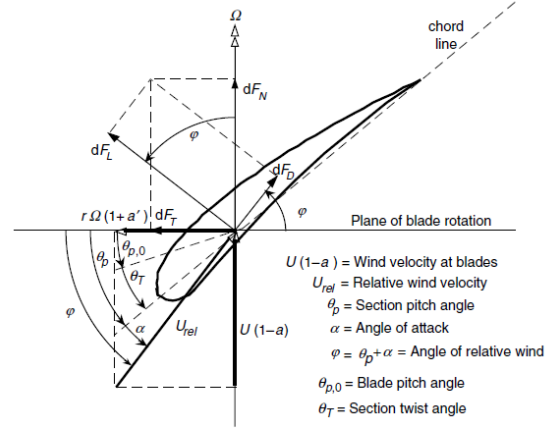


Figure 2.5 Vector diagram for HAWT blade element analysis [18]

First, the following expressions can be derived from the figures:

$$\tan \varphi = \frac{U(1-a)}{\Omega r(1+a')} = \frac{1-a}{(1+a') \cdot TSR_r} \quad (2.21)$$

$$U_{rel} = \frac{U(1-a)}{\sin \varphi} \quad (2.22)$$

$$dF_L = \frac{1}{2} \rho C_l U_{rel}^2 c dr \quad (2.23)$$

$$dF_D = \frac{1}{2} \rho C_d U_{rel}^2 c dr \quad (2.24)$$

Consequently, to find the off- and in- plane forces the lift and drag are to be translated to normal and tangential planes.

$$dF_N = dF_L \cos \varphi + dF_D \sin \varphi = \frac{1}{2} \rho U_{rel}^2 c dr (C_l \cos \varphi + C_d \sin \varphi) \quad (2.25)$$

$$dF_T = dF_L \sin \varphi - dF_D \cos \varphi = \frac{1}{2} \rho U_{rel}^2 c dr (C_l \sin \varphi - C_d \cos \varphi) \quad (2.26)$$

It can be noted that the drag affects negatively the tangential force associated with power extraction, whereas the lift is beneficial. That is why the most desired aerofoil characteristic is a high  $C_l/C_d$  at lower A.o.A. In addition, these forces can be transformed into overall thrust and torque of the rotor by multiplying with the corresponding number of blades and lever arm as displayed by equations (2.27) and (2.28).

$$dT = B \cdot dF_N \quad (2.27)$$

$$dQ = Br \cdot dF_T \quad (2.28)$$

### BEM Theory

From the Momentum Theory, it can be derived expressions for the contributions to the thrust and torque of a section of the blade, as shown by equations (2.29) and (2.30).

$$dT = \frac{1}{2} \rho U^2 4a(1-a) 2\pi r dr \quad (2.29)$$

$$dQ = 4a'(1-a) \frac{1}{2} \rho U \Omega r^2 2\pi r dr \quad (2.30)$$

After equating both models, and taking into account the rotation of the wake, expressions for the inflow angle and the chord are obtained:

$$\varphi = \frac{2}{3} \tan^{-1} \left( \frac{1}{TSR_r} \right) \quad (2.31)$$

$$c = \frac{8\pi r}{BC_l} (1 - \cos \varphi) \quad (2.32)$$

The concepts described in this section are further employed for the blade design process [18].

### 2.2.2 Rotational Effects and Stall Delay

As seen from the previous section, drag forces are due to the combination of pressure distribution and viscous friction between the airflow and the aerofoil. The flow over the aerofoil can be immediately adjacent to the surface, i.e. boundary layer or farther where frictional effects can be considered negligible. In the first case, the flow is characterised as laminar or turbulent, which depends on the Reynolds number regime at that specific point and time. Usually, a transition is made along the surface from laminar at the leading edge to turbulent downstream. In addition, the pressure gradient has a significant effect on the flow since it can accelerate, decelerate or even reverse its direction with the aid of the surface friction. This combined effect results in a flow separation from the surface, known as stall, mostly when the flow is still laminar at the boundary layer.

Furthermore, there is the effect of angle of attack (A.o.A.), which also determines the behaviour of the aerofoil. As seen from the example displayed in Figure 2.6, there is a point at which the lift does not increase further but drops, thus consequently increasing the drag; that inflexion point is called stall angle. In the past, wind turbines blades had a fixed pitch and the control was done taking advantage of the stall in order to limit the power at high wind speeds. Nowadays, this is done via variable pitch control.

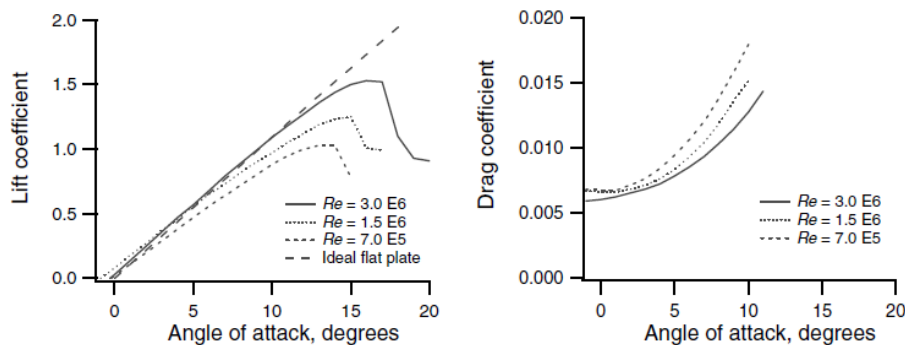


Figure 2.6 Lift and drag coefficients for aerofoil NACA 0012 [18]

### 3-Dimensional Flow

In addition to the effect of the A.o.A. on the aerofoil's aerodynamic behaviour, it was first evidenced that due to the rotation of the blade there was a so-called aerodynamic

augmentation, when studying helicopter rotor aerodynamics. That is, an increase in the lift and a subsequent delay in the stall. This could be explained as a result of centrifugal and Coriolis accelerations, which have a significant effect on the flow separation. However, this was not always the case since it was confirmed experimentally to occur strongly towards inboard sections of the blade [19], whilst at lower A.o.A. the behaviour outboards resembles the one of a stationary blade but still evidencing major differences at larger A.o.A.

Stall delay can be described by three events: First, wakes are generated due vortices from the mid-span sections towards the root. Second, a suction pressure along the chord is re-distributed followed by a constant airflow circulation. In addition, flow circulation occurs spanwise, thus decreasing the lift and increasing the separation bubble size. This results in a separation of the flow beyond a radial position inverse to the TSR, and consequently to leading-edge stall. According to Dimitrescu et al. [20], this phenomenon starts at TSR = 3. The events of stall delay are depicted in Figure 2.7, and the so-called 3-D (or radial) flow from a CFD simulation in Figure 2.8.

Laminar separation bubbles occur when the flow is unable to make the transition to turbulent at the boundary layer. Therefore, the flow separates from the surface before the transition and the turbulent flow re-attaches to the surface, thus creating the aforementioned bubbles. This phenomenon is generally accompanied by an increase in the drag and as consequence a drop in the lift, hence degrading the aerofoil's aerodynamic performance [21].

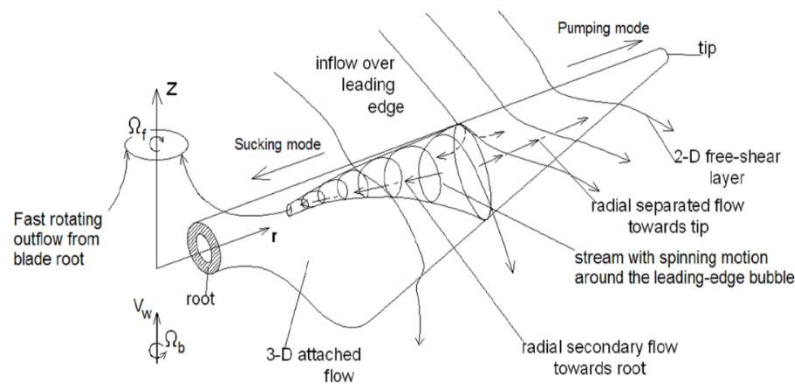


Figure 2.7 Events of stall delay [20]

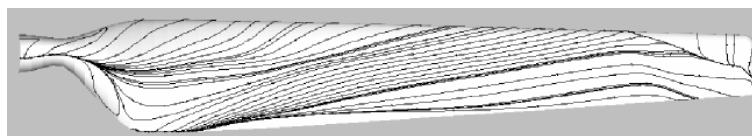


Figure 2.8 3-Dimensional flow over an experimental wind turbine blade [19]

Moreover, when the inflow angle exceeds dynamically the static stall angle, a significant increase in lift is observed due to unsteady boundary layer separation that creates increasing vortices. This is known as dynamic stall [19].

Aforementioned phenomena, especially the stall delay due to rotational effect on aerofoils' aerodynamic performance is to be taken into account for wind turbine blade design purposes. In this sense, several correction models have been proposed over the years, which when applied to 2-D-based polars, the non-dimensional aerofoil characteristics are adjusted to incorporate the aforementioned effects. Chronologically ordered these are: Snel & van Bussel (1993), Du & Selig (1998), Chaviaropoulos & Hansen (2000), Lindenburg (2004), and more recently Bak & Johansen (2006). All models, except for the last one follow a linear

approximation form for both lift and drag coefficients as described by equations (2.33) and (2.34), by varying the slope  $f$  [22]:

$$C_{l,3D} = C_{l,2D} + f \left( \frac{c}{r}, \dots \right) \cdot \Delta C_l \quad (2.33)$$

$$C_{d,3D} = C_{d,2D} + f \left( \frac{c}{r}, \dots \right) \cdot \Delta C_d, \quad (2.34)$$

where  $c/r$  is defined as the aerofoil local solidity since it is computed at its location  $r$  along the blade. This is important to establish whether it should be treated as in-, mid- or outboard. The models are described in the following table:

Table 2.3 3-D Correction models for aerofoil characteristics [22]

Authors	Slope Lift	Slope Drag	Definitions
Snel & van Bussel	$f_{cl} = 3 \left( \frac{c}{r} \right)^2$	-	-
Du & Selig	$f_{cl} = \frac{1}{2\pi} \left[ \frac{16 \left( \frac{c}{r} \right) a a - \left( \frac{c}{r} \right)^{\frac{dR}{AR}}}{0.1267 \frac{dR}{AR} - 1} - 1 \right]$	$f_{cd} = -\frac{1}{2\pi} \left[ \frac{16 \left( \frac{c}{r} \right) a a - \left( \frac{c}{r} \right)^{\frac{dR}{AR}}}{0.1267 \frac{dR}{AR} - 1} - 1 \right]$	$\Lambda = \frac{\omega R}{\sqrt{V_\infty^2 + (\omega r)^2}}$ $a = b = d = 1$
Chaviaropoulos & Hansen	$f_{cl,cd} = a \left( \frac{c}{r} \right)^h \cos^n \theta$		$a = 2.2$ $h = 1$ $n = 4$
Lindenburg	$f_{cl} = 3.1 \left( \frac{\omega r}{V_{rel}} \right)^2 \left( \frac{c}{r} \right)^2$	-	-
Bak & Johansen	$C_{l,3D} = C_{n,3D} \cos(\alpha) + C_{t,3D} \sin(\alpha)$	$C_{d,3D} = C_{n,3D} \sin(\alpha) - C_{t,3D} \cos(\alpha)$	$C_n$ & $C_t$ are normal and tangential coefficients

### Post-stalled aerodynamic behaviour

Beyond stall region, and in general outside of the attached flow and stall regimes, aerofoils' behaviour is not easily predicted by computational tools. Therefore different approaches have been introduced in order to determine the polars. These are the data set of the curves presented in Figure 2.6, but in the full range from -180 to 180. For instance, the aerofoil can be modelled as a flat plate beyond 45°, which means that the lift and drag coefficients can be approximated by equations (2.35) and (2.36) [23].

$$C_l = 2 \cdot \sin \alpha \cdot \cos \alpha \quad (2.35)$$

$$C_d = C_{d,max} \cdot \sin^2 \alpha, \quad (2.36)$$

with  $\alpha$  being the angle of attack. In addition, Viterna and Corrigan proposed a more complete method, which is being amply used in wind turbine design practices. It is driven by basic equations (2.37) and (2.38) [24] [25].

$$C_l = A_1 \sin 2\alpha + A_2 \frac{\cos^2 \alpha}{\sin \alpha} \quad (2.37)$$

$$C_d = B_1 \cdot \sin^2 \alpha + B_2 \cos \alpha, \quad (2.38)$$

where  $A_1, A_2, B_1$  and  $B_2$  are coefficients specific to every aerofoil polar.

## 2.3 Impact of Floating Dynamics on Aerodynamic Design

Floating support structures, unlike bottom-fixed ones, have the freedom to move from one point to another and to oscillate around certain axis. These translational and gyroscopic motions are therefore transferred to the entire turbine (Rotor-Nacelle Assembly – RNA –, and tower), becoming of particular significance for its effects on the rotor and its aerodynamic performance. In this section, a description of the effects of floating dynamics on the rotor aerodynamics is introduced and further validated.

### 2.3.1 Floating platform motions

First, the motions of the floating platform are characterised by six degrees of freedom (D.o.F.), three of displacement and three of rotation: surge refers to horizontal side-to-side, sway to horizontal fore-to-aft, and heave to vertical. On the other hand, roll refers to side-to-side rotation, pitch refers to fore-to-aft, and yaw to the rotation about the vertical axis. These D.o.F. are depicted in Figure 2.9.

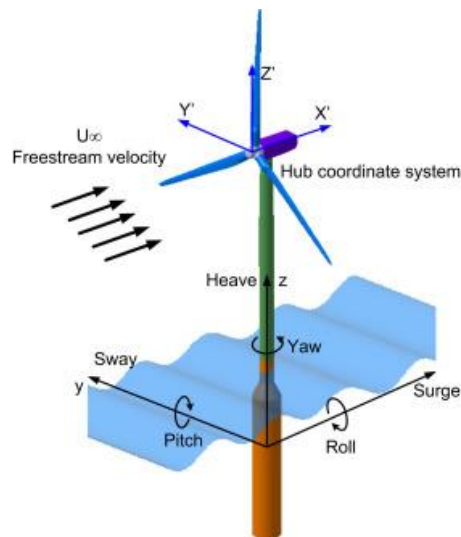


Figure 2.9 Degrees of Freedom of a rigid FOWT [26]

### 2.3.2 Aerodynamic Effects of Floating Dynamics

As a consequence of the aforementioned motions, especially when pitching fore and aft, the rotor blades could experience changes in the inflow, which induce variations in the instantaneous angles of attack due to additional tilting of the main shaft. Therefore, the aerodynamic performance is affected by the so-called dynamic stall hysteresis. This event invalidates the main assumption of the BEMT, based on the axial air flow acting upon the rotor [6]. However, correction models have been developed in order to make feasible the use of BEM codes for wind turbine performance prediction, e.g. the Beddoes-Leishman model [18].

#### *Additional Rotor Tilt Angle*

The added rotor tilt angle oscillates between 5 - 10° for spar and semi-submersible type of floating platforms, which are the ones that have more pitch freedom. This variation causes annual energy production (AEP) losses up to 4.5%. In order to compensate for those motions, a dynamic ballasting is being implemented in modern FOWTs [27].

Another effect is observed when the thrust changes rapidly due to the motion of the floating platform, and the rotor is unable to achieve a new equilibrium. This is known as dynamic inflow

(or time-varying rotor induction) since there is a sudden variation in the angle of attack. In this sense, BEMT is not well-equipped to overcome these changes, hence generating delays in the response.

### Reduced Frequency Analysis

In addition to the aforementioned, more complex effects are derived from the interaction of the rotor with its own wake, seen as flow unsteadiness. For instance, this condition can be identified through the assessment of the reduced frequency  $k_i$ , a dimensionless parameter described by equation (2.39). This allows to establish the unsteadiness of a flow over a blade section chord length  $c_i$  due to variation of the inflow velocity (denominator) as a result of a platform frequency  $\omega_{ptfm}$ . This parameter is zero for steady, between zero and 0.05 for quasi-steady, between 0.05 and 0.2 for unsteady and larger for highly unsteady conditions, according to Theodorsen's theory [28].

$$k_i = \frac{\omega_{ptfm} c_i}{2\sqrt{U_\infty^2 + (r_i \Omega)^2}} \quad (2.39)$$

### Vortex Ring State

One of the most relevant effects is the vortex ring state (VRS) that occurs occasionally and is induced when the platform pitches in the same direction as the inflow (generally leeward). With the VRS, air recirculates in a toroidal shape near the blade tip as seen in the third frame (left to right) from Figure 2.10. This leads to unsteady loads, which makes the rotor to behave as a propeller in the sense that provides energy to the surrounding air instead of extracting it. Thrust and torque are driven by VRS's energy dissipation. Evidently, due to the drop in the effective wind speed, the assumptions for the application of BEMT are broken down. In addition, at lower wind speeds it is more likely that outboard sections are subjected to unsteadiness [28].

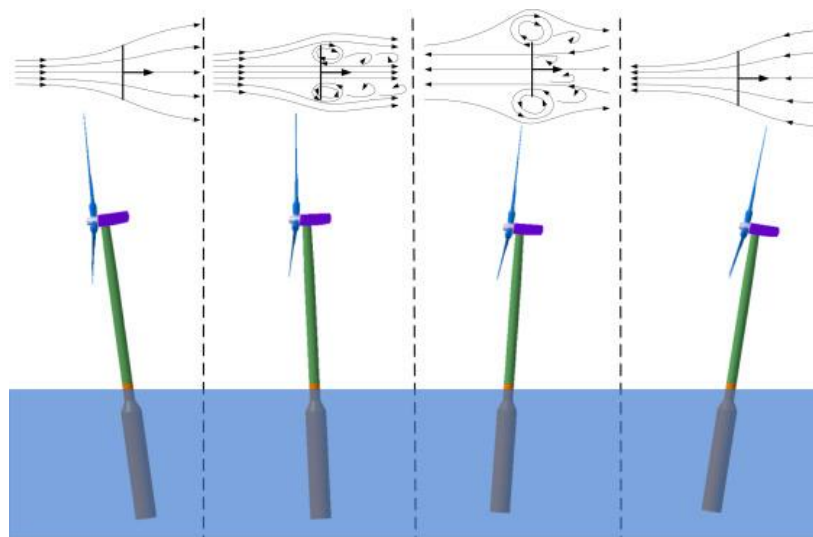


Figure 2.10 Transition from windmill to propeller state during rotor wake interaction [26]

### Validation of the Effects

In order to quantify the overall impact of the floating platform dynamics on the aerodynamic design of the FOWT rotor, a validation exercise was done by Matha et al. In this study, changes in inflow velocities and angles of attack throughout the span were identified when comparing floating against onshore configuration.

For this purpose, the NREL 5MW Offshore Baseline Wind Turbine, further detailed in chapter 3 was simulated in FAST (see section 4.3.3) with the Hywind spar support structure, using the corresponding controller developed within the Offshore Code Comparison Collaboration (OC3) programme. The setting included 11.3 m/s as testing wind speed and a 2.29° blade pitch. Furthermore, corrections for axial and tangential induction as well as tip and hub losses (Prandtl and skewed-wake approximations) were incorporated for aerodynamic load prediction in AeroDyn sub-routine, further introduced in this work. Additionally, for aerofoil analysis XFOIL (introduced in section 4.3.1) was put to use with the aid of Viterna's extrapolation method and Snel & van Bussel 3-D correction. Finally, for the hydrodynamic loads, the use of HydroDyn was of great importance [29].

As seen from Table 2.4, the variations in the most relevant parameters subjected to analysis are considerably low, which indicates that for design purposes the effects of floating dynamics can be neglected.

Table 2.4 Variations in simulated aerodynamic parameters from floating with respect to onshore setting [29]

Radial Position [m]	$\Delta U_{rel}$ [%]	$\Delta A. o. A.$ [%]
14.2	-1.55	0.39
16.7	-1.45	0.12
21.9	-1.36	-0.11
30.0	-1.31	-0.26
38.2	-1.28	-0.04
53.9	-1.26	0.22

This can be confirmed by Figure 2.11, in which additional simulations for the same reference turbine were performed in both floating (Hywind spar OC3 platform) and onshore settings. In this case, the only difference was the test wind speed, which was 8 m/s (blade pitch 0°). Nonetheless, it is evident that on average the values for thrust and power are very close, hence the assumption of neglecting the floating effects is proved.

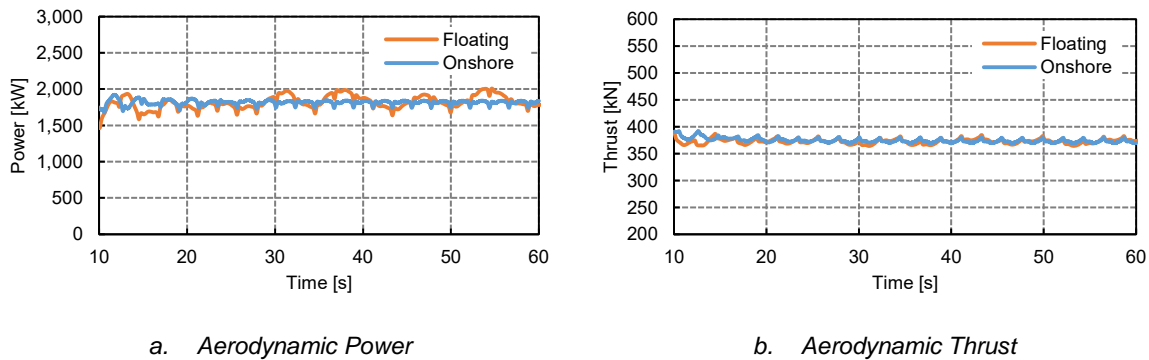


Figure 2.11 Comparison of aerodynamic performance for floating vs. onshore setting for the NREL 5MW

# 3 Benchmark study on Model-scale Blade Design

In agreement with the scaling procedures and aerodynamics presented in chapter 2, several approaches to the design of a wind turbine rotor blade to be built and tested in a wind/wave tank have been introduced by distinct research groups. The procedure designers followed, their outcomes and their aerodynamic performance is presented in section 3.1. Consequently, the associated testing methods are discussed in section 3.2.

## 3.1 Rotor designs

In order to pursue the mutual motivation of developing at large-scale the offshore floating industry, there have been several exercises done in the past for testing the NREL 5MW Offshore Baseline Wind Turbine (NREL 5MW hereinafter) and the DTU 10MW Reference Wind Turbine (DTU 10MW hereinafter). The first, developed by the National Renewable Energy Laboratory (NREL) in 2009 [30] and the latter developed first in 2012 in the framework of the Light Rotor Project [31] as an upscale from the NREL 5MW and further refined in 2013 within the INNWIND.EU programme [32]. The key parameters of both turbines are shown in Table 3.1. For instance, the University of Maine (UMaine), followed by MARIN (Maritime Research Institute Netherlands), Politecnico di Milano (PoliMi), and more recently the wind energy department of the Denmark Technical University (DTU Wind) developed rotors for model-scale testing of the above-mentioned, which are presented in this section.

Table 3.1 Key parameters of the DTU 10 MW and the NREL 5MW Reference Wind Turbines [30, 32]

Parameter	DTU 10MW	NREL 5MW
Wind Regime	IEC Class 1A	IEC Class 1B
Rotor Orientation	Clockwise - Upwind	Clockwise - Upwind
Control	Variable Speed – Collective Pitch	Variable Speed – Collective Pitch
Rated Power	10 MW	5 MW
Number of Blades	3	3
Rotor Diameter	178.3 m	126 m
Cut-In, Rated & Cut-Out Wind Speeds	4, 11.4 & 25 m/s	3, 11.4 & 25 m/s
Rotational Speed Range	6 – 9.6 rpm	6.9 – 12.1 rpm
Maximum Tip Speed	90 m/s	80 m/s
Hub Diameter	5.6 m	3 m
Hub Height	119 m	90 m
Rotor Mass	228,962 kg	110,000 kg
Nacelle Mass	446,036 kg	240,000 kg
Tower Mass	628,442 kg	347,460 kg

### 3.1.1 University of Maine

The Advanced Structures and Composites Centre from the University of Maine has come up with three different designs of wind turbine models, based on the NREL 5MW, for testing floating platforms with the purpose of replicating accurately the thrust forces.

#### *First Blade Design*

The first rotor was developed in 2011 as part of the M.Sc. Thesis from the Civil Engineering department, which purpose was to develop an entire model wind turbine for testing in a wind/wave basin. With its development, a subsequent design methodology for scaled-down

wind turbines for testing purposes was introduced, called 'Performance Scaling'. The premise of this methodology is to design a blade such that it matches closely the non-dimensional full-scale performance, i.e. match the power and thrust coefficients at low Reynolds numbers.

The outcome of this exercise was a 1/50<sup>th</sup> scale ( $\lambda = 50$ ), i.e. 1.23m-long rigid carbon-fibre hollow blade design, geometrically similar (geo-sim) to the original design of the NREL 5MW. The motivation for this design was to keep unaltered the geometry of the industry standard by that time. However, in order to improve the manufacturability the thickness of both the aerofoils and the trailing edges, the centrelines were adjusted and the non-dimensional chord ( $c/r$ ) distribution was smoothened.

However, after constructing and testing this rotor's performance in a floating setting with three different floating platforms: spar buoy, (TLP) and semi-submersible at MARIN's offshore basin [33], it was evidenced that the aerodynamic coefficients were significantly lower than expected at full-scale. This is due to the fact that aerofoils from the full-scale rotor blade are not suitable for low Reynolds numbers present when Froude-scaling, as explained before in section 2.1.3. This mismatch induces laminar flow separation, whose effect is to increase the drag and therefore decrease the lift coefficient, making the thrust coefficient low contrary to what is desired. For this reason, the blade sections were tripped by increasing their roughness on the leading edge side, which makes the flow more turbulent and less prone to detach (an effect described in section 2.2.1). This resulted in a performance improvement, but not enough to meet the full-scale expectations.

### Second Blade Design

Therefore, a new rotor was designed by switching all the aerofoils (including the cylinder from the blade root) by the Drela AG04 [34] (AG04 hereinafter), which is a thin profile less susceptible to laminar flow separation than the ones composing the NREL 5MW blade [12, 35]. In addition, the chord, relative thickness and twist angle distributions were re-defined, as shown comparatively in Figure 3.3.

This redesign, analysed numerically, brought a match in the thrust coefficient between the model- and the full-scale as presented in Figure 3.1. Furthermore, the power coefficient was also analysed, and even though it came closer, it is still lower for the model-scale. This is due to the increase in the drag at low Reynolds numbers, which decreases the torque and consequently power. Nevertheless, this is completely acceptable since the ultimate goal is to mimic the thrust force that is translated as overturning moment on the floating platform.

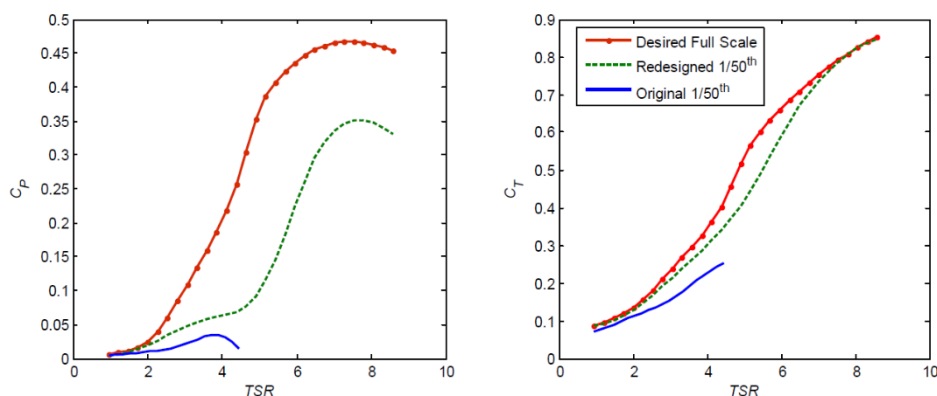


Figure 3.1 Comparison of Power and Thrust coefficients vs. TSR for target, first & second blade design from UMaine [12]

### Third Blade Design

Later on, a third blade design was realised with the Drela AG24 [34], from the same family of the previous approach but with slightly larger thickness. This selection obeyed to its positive performance under low-Reynolds numbers. The scale factor was 130, which was in line with the turbine testing setting available at UMaine at that moment. Nonetheless, the wind conditions comply with 1/50<sup>th</sup> Froude-scaling. The chord distribution was greatly increased, in order to increase the Reynolds regime, as shown in Figure 3.3. This is a result of an optimization process, in which the chord and twist angle distributions vary to the end of closely matching  $C_T$  and  $C_P$ , bounded by upper and lower limits. [36]

The blade design was then analysed using the BEMT code embedded in NREL's WT\_Perf, which unfortunately is out of circulation and replaced by the AeroDyn subroutine [37] from FAST (Fatigue, Aerodynamics, Structure and Turbulence wind turbine simulator) [38], explained in section 4.3.3. Furthermore, the blades were 3-D-printed and further tested in a wind tunnel setting under controlled conditions. The comparative results for the  $C_T$  and  $C_P$ , corresponding to the target (continuous red line), first (dotted red line) and third (blue lines) blade designs are depicted in Figure 3.2. It is evident that this exercise exceeded the target values. Therefore the approach taken for the third blade design is not entirely reliable.

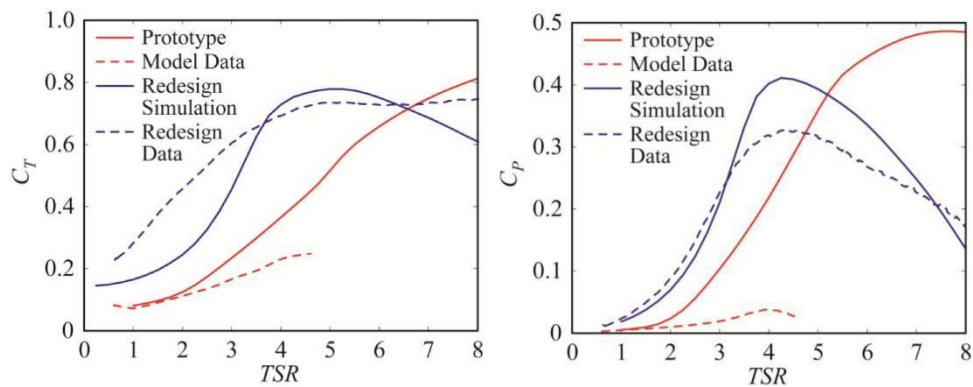
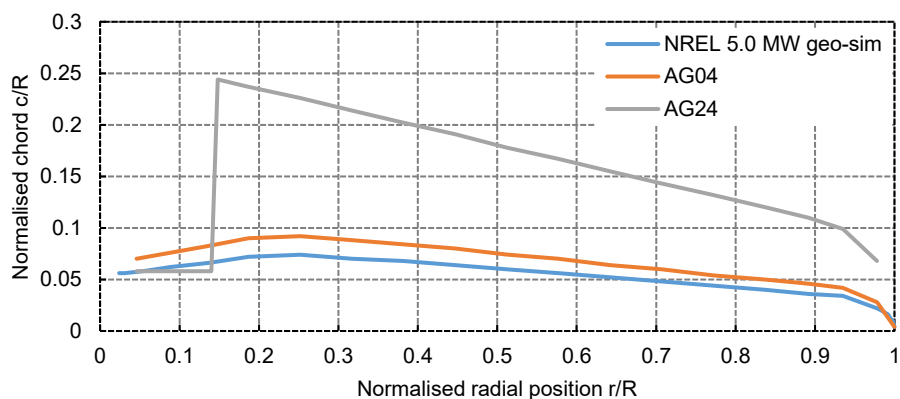
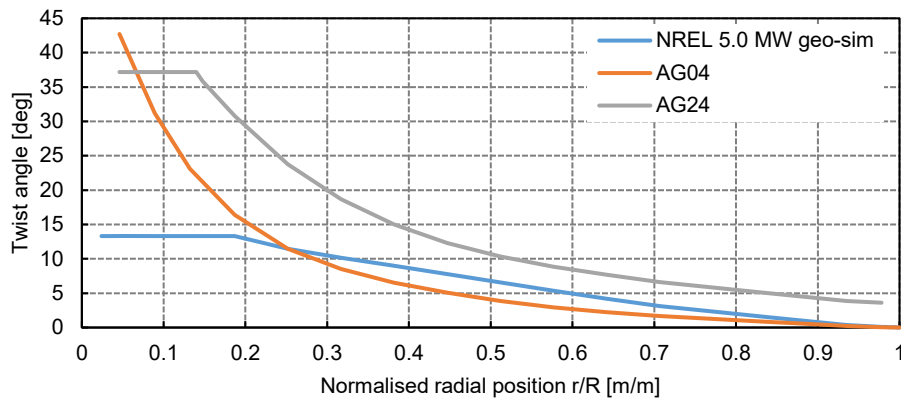


Figure 3.2 Comparison of Thrust and Power coefficients vs. TSR for target, first and third blade design from UMaine [36]

### Non-dimensional geometries of the blade designs

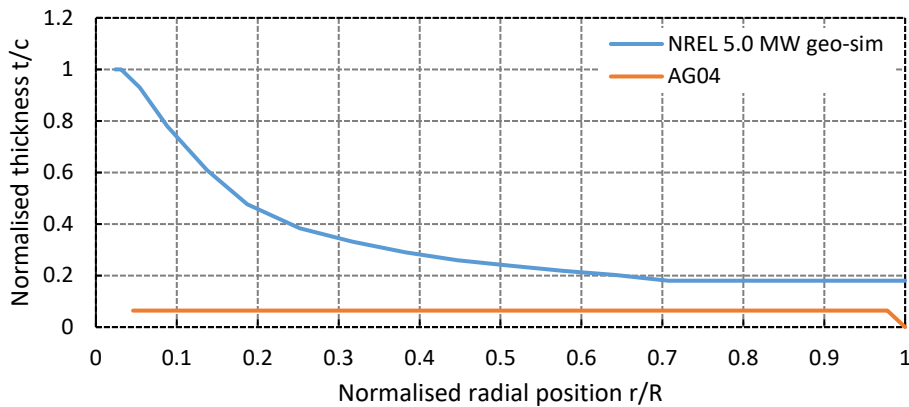


a. Normalised chord distribution



b. Twist angle distribution

For the thickness there was no information reported for the third design [36], therefore it is not shown in the comparative figure below.



c. Normalised relative thickness distribution

Figure 3.3 Representative distributions for geo-sim blade from NREL 5MW & re-design UMaine

### 3.1.2 MARIN Stock Wind Turbine

After this first approach made by UMaine, MARIN took the most trusted design (second method), improved, analysed, constructed and tested it in their wind / wave basin, further detailed in section 3.2.1. For this purpose, the same methodology of the “performance scaling” was followed, which yielded in the MARIN Stock Wind Turbine (MSWT) rotor blade design ( $\lambda = 50$ ). According to the results from the testing campaign, the non-dimensional aerodynamic performance is in line with the full-scale behaviour and with the results from in-house Computational Fluid Dynamics (CFD) computations [39].

In order to meet manufacturing constraints, the original AG04 aerofoil used in the UMaine design suffered an increase in its thickness to twice its value at every chord position as displayed by Figure 3.4. This modification was carefully applied since the purpose is to avoid laminar flow separation and keep the  $C_L/C_D$  ratio as high (as explained in chapter 2) and as close as possible to the original AG04 profile. This was verified with the aid of XFOIL [40], a powerful tool for aerofoil analysis, further introduced in the chapter 4.

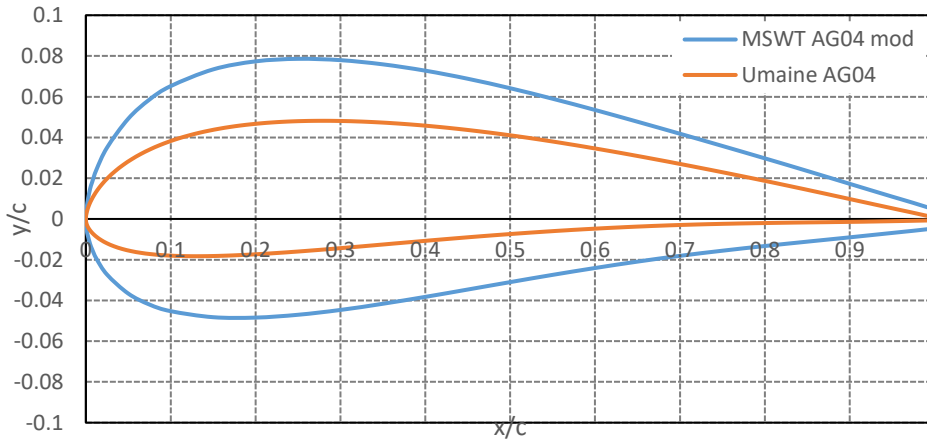
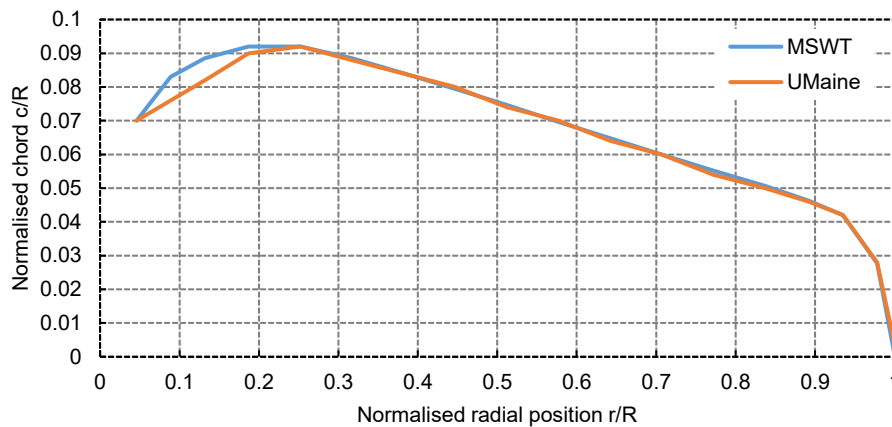
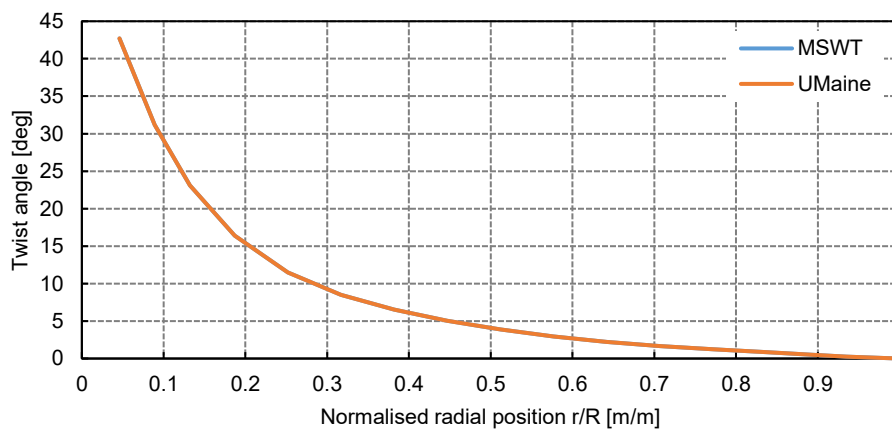


Figure 3.4 Geometries of the AG04 aerofoil used in the MSWT and UMaine blade designs

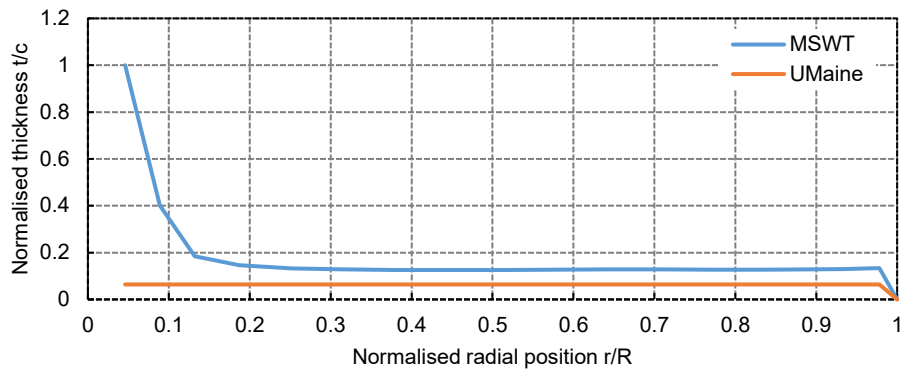
Now, spanwise the chord and twist angle distributions remained virtually unaltered. However, as explained before the thickness was increased to twice its original value but the transition from the cylinder present at the blade root and the first section was smoothed. The comparison of distribution between the MSWT and UMain (No.2) are shown in the figure below:



a. Normalised chord distribution



b. Twist angle distribution



c. Normalised relative thickness distribution

Figure 3.5 Representative distributions for MSWT & UMaine blade designs

With the geometry of the blade defined, an analytical study of the aerodynamic performance was carried out in order to determine the closeness of the thrust and power coefficients with the full-scale NREL 5MW. This was done with the aid of PropID, a code for analysis and design of HAWT developed by the University of Illinois Urbana-Champaign, used for computing the power and loads by means of BEMT [41].

Then, the blades were constructed using carbon-fibre epoxy composite material in order to achieve the stiffness that would comply with the rigid and lightweight assumptions used for modelling purposes. Furthermore, once the blades were characterised, the test campaign was carried out at MARIN's Offshore Basin under controlled environmental conditions using the GustoMSC Tri-Floater as floating platform, for which the nacelle was equipped with gauges to measure accelerations and torque, and further instrumented for data acquiring.

Moreover, the performance was verified using an in-house CFD code called ReFRESHCO [42], detailed in section 4.4.3, which makes possible to incorporate a three-dimensional flow. So far the flow has been considered to move in a bidimensional plane (axial with respect to the main shaft). This is very important because it is a consequence of the so-called rotational effect, which brings a decrease in the lift coefficient and a subsequent increase in the drag. The following figures show comparatively the outcomes from PropID, ReFRESHCO and testing, with respect to the NREL 5MW full-scale thrust and power coefficients respectively.

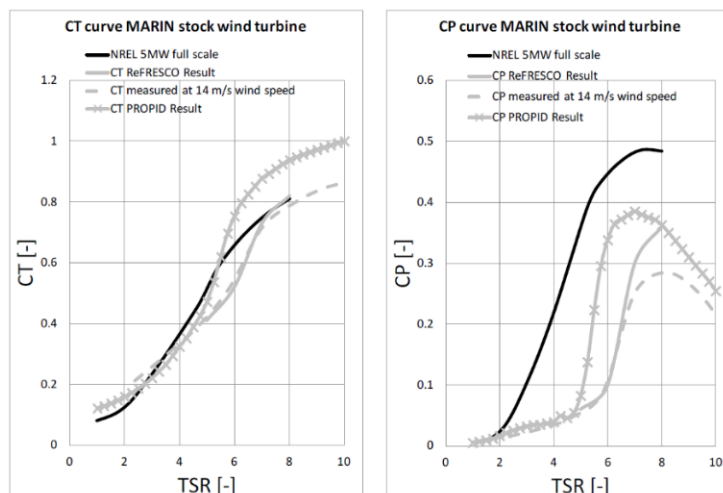


Figure 3.6 Comparison of Thrust and Power coefficients vs. TSR for MSWT and NREL 5MW obtained with BEMT, CFD and testing [39]

As evidenced from these, the NREL 5MW expected values for the thrust coefficient are closely matched by the measurements and computations, whilst the power coefficient was underpredicted. However, it is interesting to note that the BEMT code PropID gives too optimistic predictions with respect to the actual measurements. This was due to the fact that the turbulence of the inflow was not properly modelled, with respect to the testing conditions.

In addition, the turbine was also tested by UMaine at scale 130 with the purpose of verify the performance of this thrust-matched approach. The results, as reported in [43], show an agreement with the tests performed at MARIN for both  $C_T$  and  $C_p$ , which gives a good indication regarding reproducibility.

### 3.1.3 Politecnico di Milano

The department of Science and Aerospace Technology from the Politecnico di Milano has been widely involved in the development of wind turbine rotors for the INNWIND.EU programme [44], specifically the LIFES50+ project that intends to develop a 10MW FOWT. The first design presented in this section was based on the NREL 5MW and the subsequent on the DTU 10MW.

#### *Froude-scaled Blade Design*

Within the framework of the INNWIND.EU programme, specifically within the project “Verification and Validation of Design Methods for Floating Structures”, a set of numerical codes for floating support structures were validated against wave tank tests [45]. For this purpose, a model-scale rotor was designed that would reproduce, at Froude-scaled environmental conditions, the thrust coefficient from the full-scale NREL 5MW. This yielded in a 1/60<sup>th</sup> scaled-down high-chord-solidity blade of approximately 1.4 m-long. The corresponding chord and twist angle distributions are presented in Figure 3.7, which according to a conversation with Dr Filippo Campagnolo (one of the designers) were obtained from applying equations (3.1) and (3.2) respectively from the Wind Energy Handbook [17].

$$c(\mu) = \frac{16\pi R}{9C_l B(TSR)^2 \mu} \quad (3.1)$$

$$\beta = \frac{2}{3 \cdot TSR_r} - \alpha \quad (3.2)$$

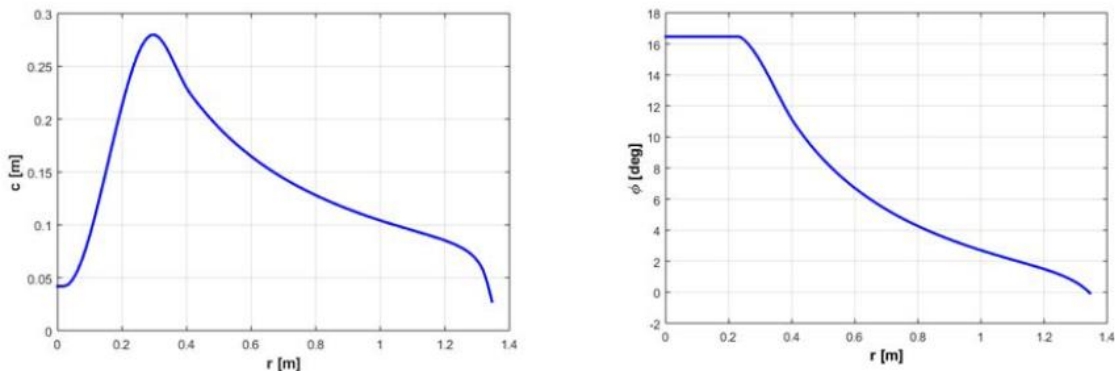


Figure 3.7 Chord and Twist Angle Distributions for “Froude-scaled” rotor [45]

The aerofoil selected for this application was the low-cambered RG14 [46], suitable for low-Reynolds numbers (approximately  $6 \times 10^4$  at mid-chord and rated wind speed), given its considerably good  $C_L/C_D$  at low angles of attack (close to 40, obtained with the aid of XFOIL

at  $Re = 60,000$  and  $N_{crit} = 9$ ). After construction and testing of the rigid carbon-fibre composite blade, the non-dimensional aerodynamic characterisation resulted in the following figure, which shows the comparison between the thrust and the power coefficients for both full- and model-scale.

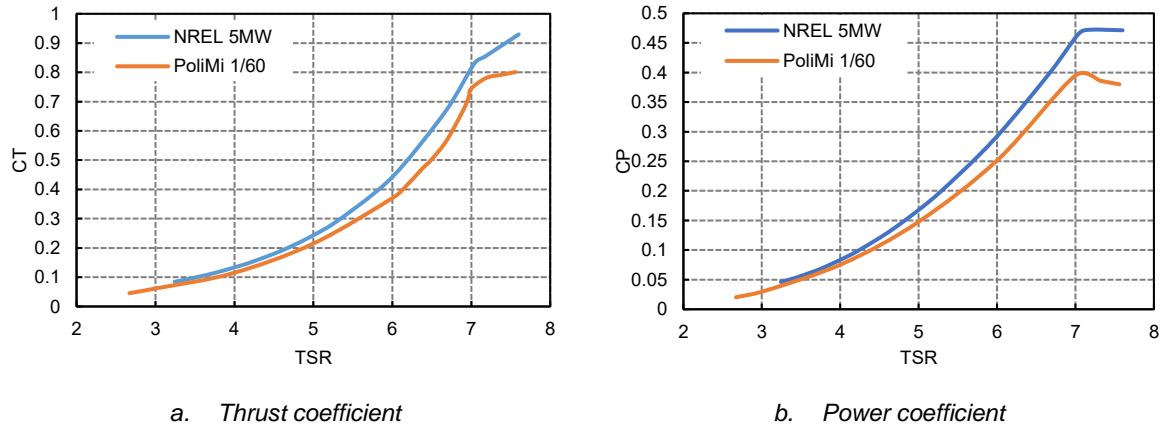


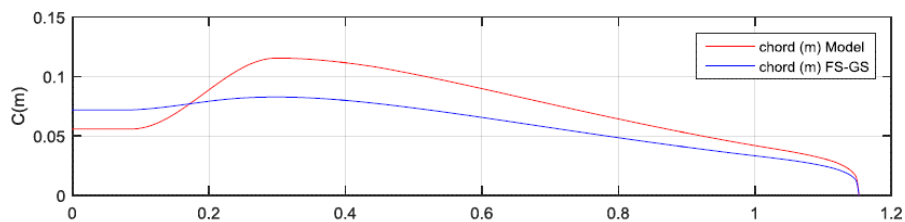
Figure 3.8 Comparison Aerodynamic coefficients vs. TSR for Full- and Model-scale [45]

In this sense, the plots show a subtle discrepancy when above TSR of 4. This means that in the full-load region, which is the most relevant one, the thrust and the power at model scale are not as high as expected. This is, of course, assuming that the TSR was kept constant during the scaling process, in order to achieve kinematic similarity, as seen before in section 2.1.3.

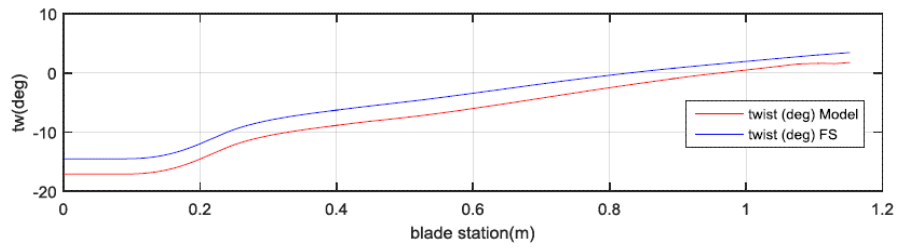
### PoliMi Combined-scaled Blade Design

The goal of this exercise was to introduce a blade design, whose aerodynamic performance would agree with the expected values for the DTU 10MW simulated using the AeroDyn subroutine of FAST. Now, according to the scaling methodology introduced in section 2.1.4, the length and wind speed are scaled differently, which results in a combined scaling factor for the forces, e.g. thrust. In this case  $\lambda_L = 75$  (chosen based on the wind tunnel dimensions) and, two wind speed scaling factors  $\lambda_V = 2$  and  $\lambda_V = 3$  for verification purposes. This means that the diameter of the model scale rotor was 2.38 m, turning at 37.68 rad/s for  $\lambda_V = 2$ . The chord, twist and relative thickness distributions were realised in order match the thrust coefficient, i.e. maximising the lift force according to equation (3.3), the first flapwise scaled natural frequency and the scaled weight [47]. In addition, the inflow angle was kept constant for both full- and model-scale. The chord, twist and relative thickness distributions are shown comparatively with the full-scale (geo-sim) distributions in Figure 3.9.

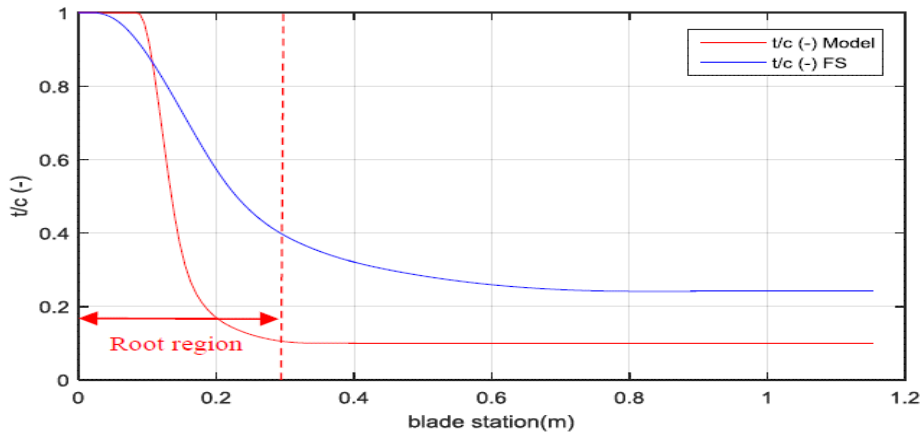
$$L_M = \frac{L_F}{\lambda_V^2 \cdot \lambda_L^2} \quad (3.3)$$



a. Chord distribution



b. Twist angle distribution (inverse)



c. Thickness distribution

Figure 3.9 Representative Distributions for DTU 10MW (geo-sim) and PoliMi Model-scale [15]

In order to cope with the scaling effects, the SD7032 aerofoil suitable for low-Reynolds number regime was chosen from the Selig's low-Reynolds database [46]. The Reynolds number orders of magnitude are displayed in Figure 3.10.

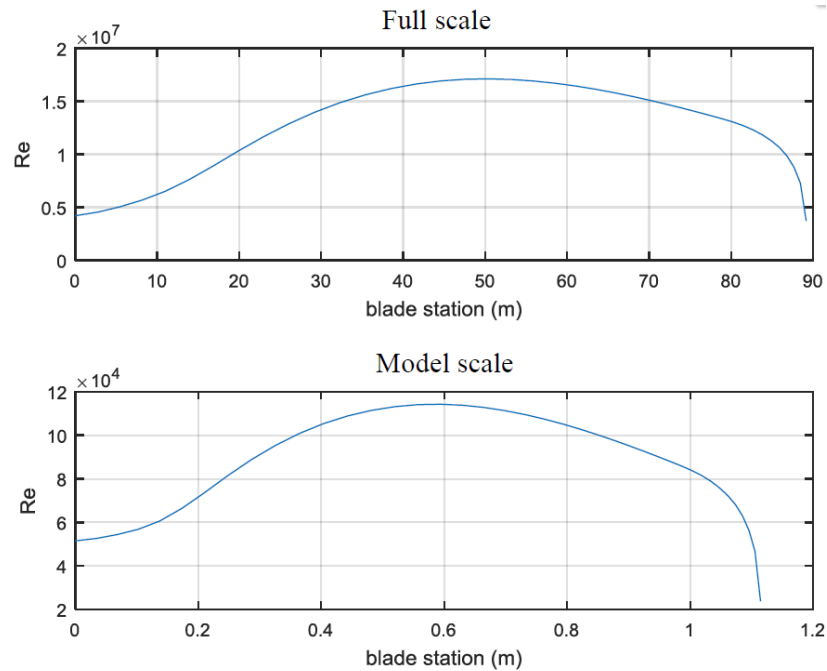


Figure 3.10 Reynolds numbers at every blade station for Full- and Model-scale [15]

The shape of these previous curves obeys to the fact that the local Reynolds numbers are calculated with the relative wind speed ( $V_{rel}$ ), introduced in the BEMT section 2.2.1, as opposed to the inflow wind speed; and the local chord for the characteristic length.

With the geometry defined, the blades were constructed and tested in a wind tunnel setting in order to characterise the rotor's aerodynamic performance. In this sense, the thrust coefficients were obtained for both  $\lambda_V = 2$  and  $\lambda_V = 3$  scaling factors. These were plotted and shown comparatively along with the values obtained for full-scale in Figure 3.11.

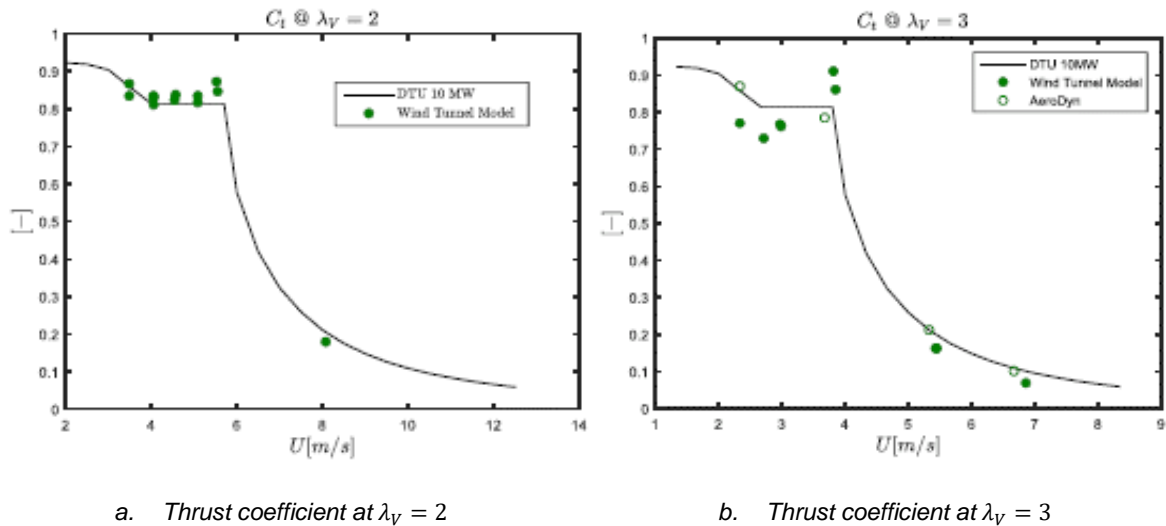


Figure 3.11 Comparison of Thrust coefficients vs. Wind Speed for Full- and Model-scale at different wind speed scaling factors [15]

As expected, the decrease in the testing wind speed (increase in the scaling factor) jeopardizes the match since the lower the Reynolds number, the earlier the laminar flow detaches from the aerofoil. This has repercussions on the lift coefficient and therefore on the thrust. Nevertheless, this matching exercise to the author's opinion is not realistic since the testing setting does not reproduce fully the environmental conditions to which the entire turbine is subjected, as it will be detailed in section 3.2.2.

### 3.1.4 DTU Wind

Within the same test campaign from the INNWIND.EU project of the Froude-scaled rotor developed by PoliMi introduced in previous section, researchers at DTU Wind designed their own blade for testing a TLP in the Danish Hydraulic Institute (DHI). This exercise was also a 1/60<sup>th</sup> Froude-based, which considered instead the DTU 10MW as baseline for a single wind speed of 10 m/s (at full-scale) and a design TSR of 7.5. The purpose was to mimic the thrust coefficient and to match the power coefficient as close as possible to the full-scale reference values. To achieve this goal, and in order to compare the aerodynamic performance, the FLEX5 aero-servo-elastic in-house code was employed, to which the DTU 10MW was adapted. In these computations, no gravity or wind shear were taken into consideration.

As seen before, one of the most important tasks when designing a Froude-based blade, i.e. to operate under low-Reynolds numbers conditions (approximately 60,000 as seen in Figure 3.12), is to select properly the aerofoil (or set of them) in order to meet the expected aerodynamic performance. In this case, the SD70xx series, developed by Selig & Donovan suitable for their implementation in the design of small wind turbines [46, 48], was chosen for further analysis. This set comprised, from tip inboards the SD7003 (t/c: 8.5%), SD7032 (t/c: 9.95%) and the SD7062 (t/c: 13.98%) aerofoils, illustrated in Figure 3.13, for which the corresponding lift and drag coefficients curves were studied.

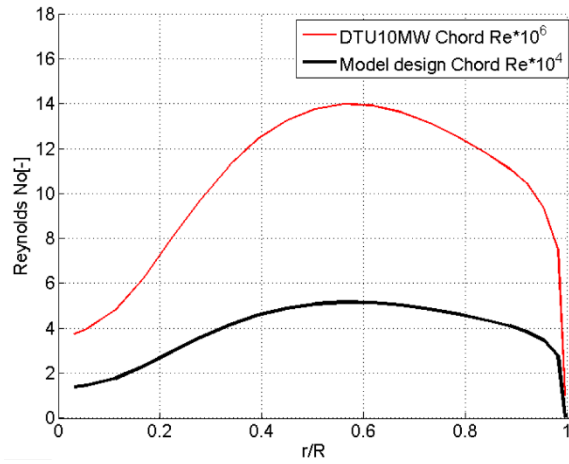


Figure 3.12 Reynolds number regime for full- and model-scale DTU 10MW 1/60

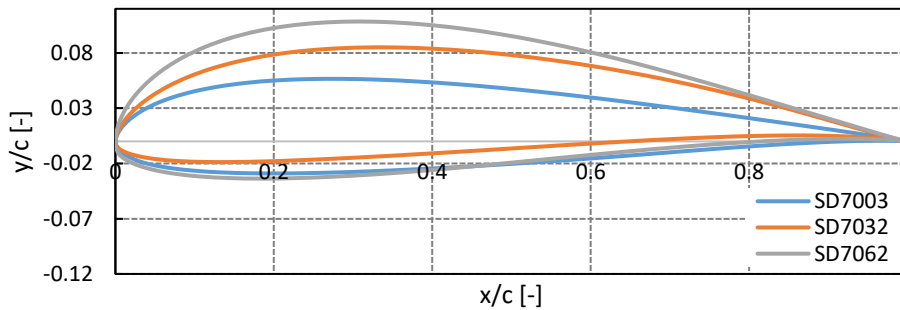
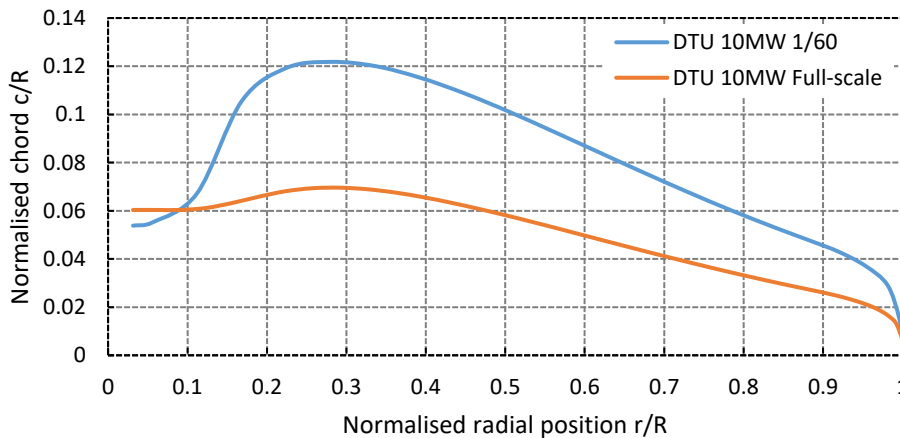
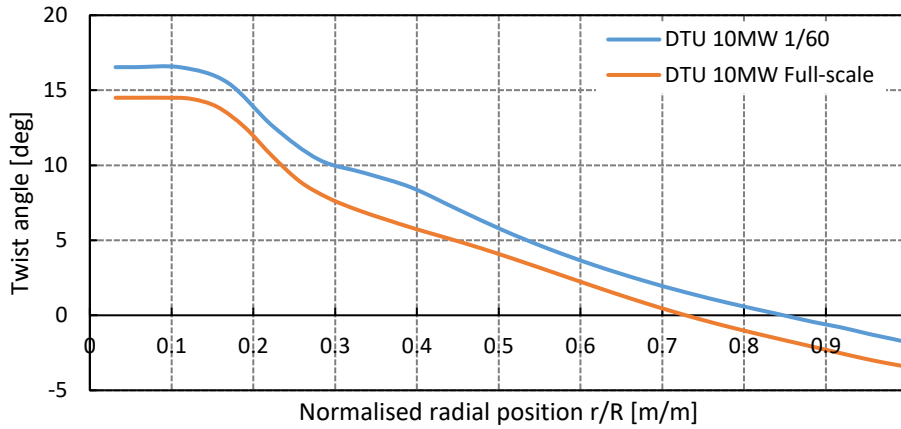


Figure 3.13 Aerofoils employed in DTU 1/60 model blade design (constructed with data from [34])

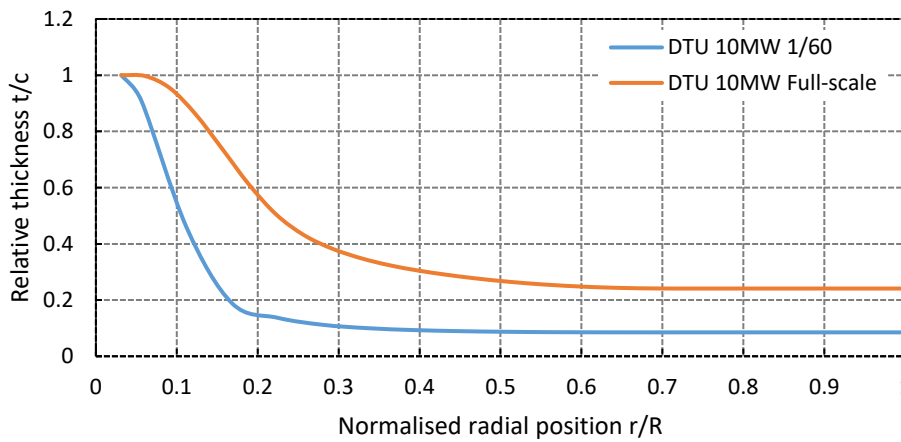
Then, a design lift coefficient of around 0.6 for the SD7003 aerofoil (in-house wind-tunnel-tested) led to a 75% chord increase with respect to the original non-dimensional chord distribution. Furthermore, the twist was slightly shifted upwards in order to incorporate the increase in raw A.o.A. of the new aerofoils. Finally, the thickness was decreased due to the implementation of thinner aerofoils, and keeping the transition to the cylinder from the blade root. Figure 3.14 displays the resultant chord, twist and relative thickness distributions.



a. Normalised chord distribution



b. Twist angle distribution



c. Relative thickness distribution

Figure 3.14 Representative distributions for the DTU 10MW at 1/60th and full-scale blade designs (adapted from [49])

This aerodynamic blade design yielded in the performance depicted in Figure 3.15 that shows an agreement at the same pitch angle set at full-scale.

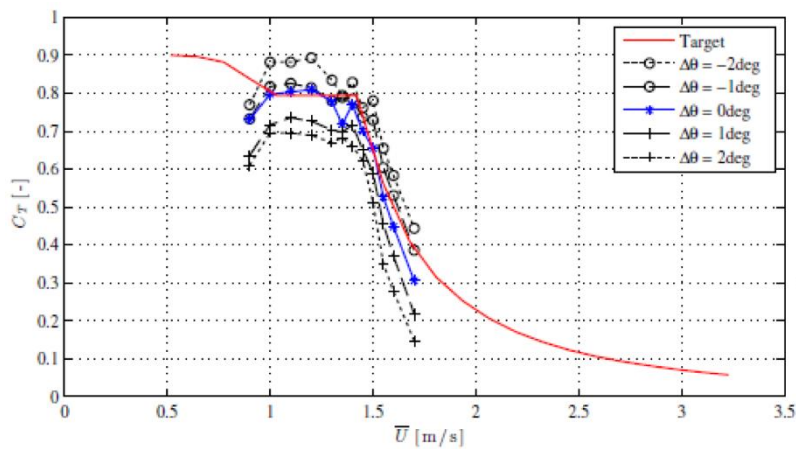


Figure 3.15 Thrust coefficient of the 1/60th model of the DTU 10MW blade for various pitch settings [50]

It can be noted that this approach did not incorporate advanced computational tools to predict such behaviour, but clearly displayed extensive experience in the subject, since based on the aerofoil aerodynamic coefficients they were able to establish the shape of the blade. Nevertheless, the use of an aerofoil distribution with decreasing relative thickness gives a convenient recommendation for the present work.

## 3.2 Testing methods

To the end of assuring that the floating support structure is correctly loaded during model testing, it is crucial to achieve the correct thrust force on the rotor as mentioned in previous sections. This is because the overturning moment generated by such force is representative with respect to the overall loading profile acting upon the platform, which also comprises the hydrodynamic loads from the waves and sea currents. In this sense, different approaches have been proposed with regard to the testing setting, which are introduced in the following sections.

### 3.2.1 Wind / Wave Basin

The most common technique used for testing FOWT is the wind/wave tank (also called offshore basin or wave tank), which purpose is to emulate as close as possible the downscaled environmental conditions that a full-scale FOWT would experiment when placed offshore. That is, to generate Froude-scaled high-quality wind, waves and sea currents acting upon the model-scale FOWT. This consists in an indoor setting, to prevent outside conditions to affect the testing. Wind is generated using a set of fans with a honeycomb, a device placed in front in order to avoid swirls and to straighten the flow as seen further in Figure 3.20, making it uniform and steady. Waves on the other hand, are produced by controlled moving paddles and further absorbed at the opposite side(s) to prevent them to return and therefore interfering with the subsequent ones, as depicted in the side view from Figure 3.16. Underwater flows related to current profiles are generated by pumps, and the recirculation is done as presented by Figure 3.19.

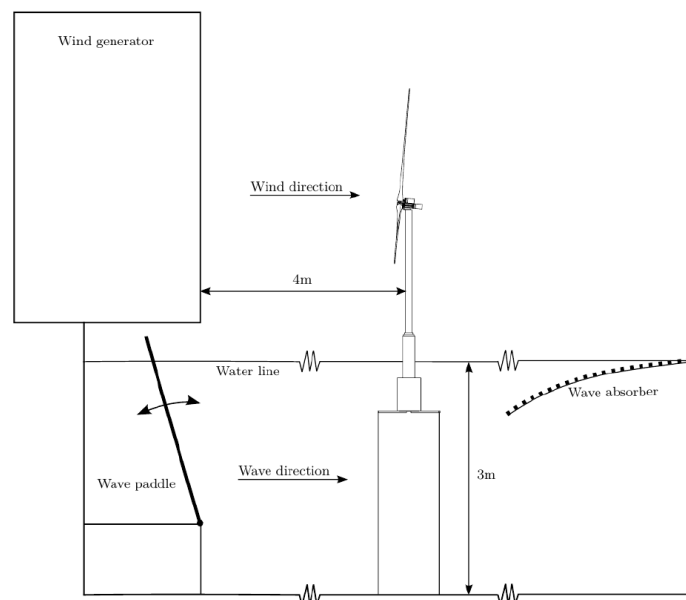
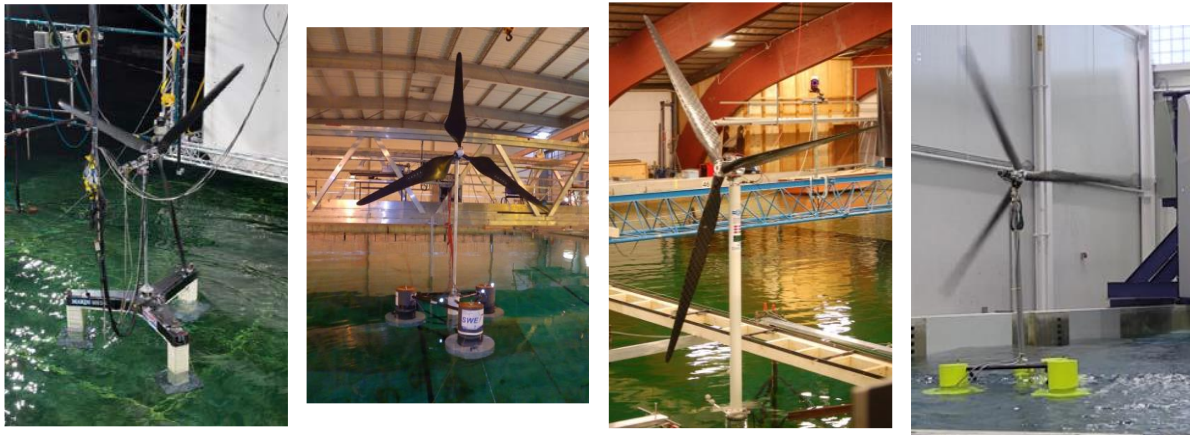


Figure 3.16 Side view of wind/wave basin for FOWT testing [45]

This concept has been implemented by MARIN, which hosted among others UMaine's first design and the MSWT's tests. Furthermore, the LHEEA - Research Laboratory in Hydrodynamics, Energetics and Atmospheric Environment of the Ecole Centrale de Nantes in France witnessed the test of the 1/60<sup>th</sup> FOWT developed by PoliMi. Moreover, the turbine

developed by DTU Wind was tested in the Danish Hydraulic Institute, and more recently UMaine invested in its Alford W2 Ocean Engineering Lab. These are shown in Figure 3.17.



a. MARIN Semi-submersible FOWT Testing in the Offshore Basin [39]

b. Ecole Centrale de Nantes Semi-submersible FOWT Testing in the Wave Tank [45]

c. Danish Hydraulic Institute TLP FOWT Testing in the Wave Basin [50]

d. UMaine Semi-submersible FOWT Testing in the W<sup>2</sup> Wind/Wave Basin [51]

Figure 3.17 Wind / Wave FOWT testing setups

The setting of interest here is MARIN's Offshore Basin since it will be the host for testing the current and future turbines that result from the implementation of the methodology yielded from this study. This particular facility has the capability of testing deep-water fields of up to 3,000m (deep pit of 30 m at model scale). In addition, the 45 m x 36 m basin has a movable floor that allows water depth to be adjusted according to the on-site conditions being emulated, up to 1,000 m at real-scale and 10.5 m at model scale. This is shown in Figure 3.18. Furthermore, every point within the testing area displayed in Figure 3.19 can be reached thanks to the three degree-of-freedom (D.o.F.) carriage, plus a six D.o.F. multiple body motion tracking system which is useful for setting and conducting tests [33].

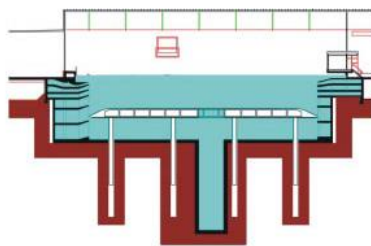


Figure 3.18 Side view of MARIN's Offshore Basin [33]

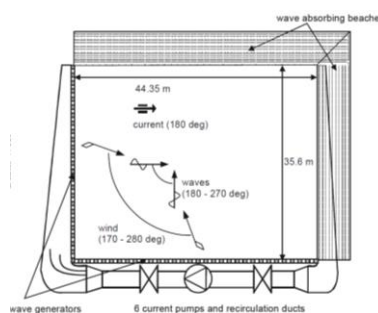


Figure 3.19 Top view of MARIN's Offshore Basin [52]

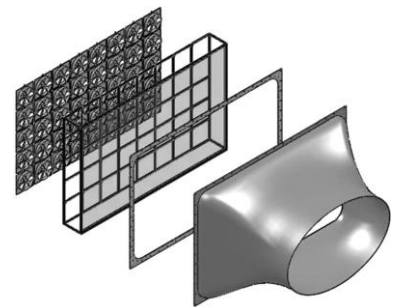


Figure 3.20 Exploded view of the wind generator for FOWT Testing in the Wave Basin [35]

The capabilities of this testing facility are numerous, which for the developed wind generation are: 35 fans rotating simultaneously in alternate directions in order to generate constant wind speeds of up to 6 m/s. These can also be controlled so that stochastic wind is generated. In addition, the flow is straightened with two honeycomb screens and further forced through an elliptical nozzle, resulting in a homogeneous low-turbulent wind field [39]. That is, approximately 4% turbulence intensity within the rotor plane as depicted in Figure 3.21 done at scale of 50 for the MSWT.

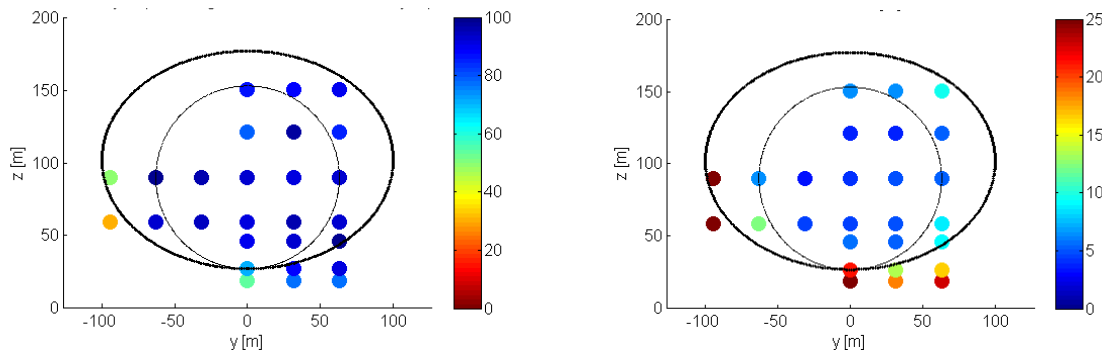


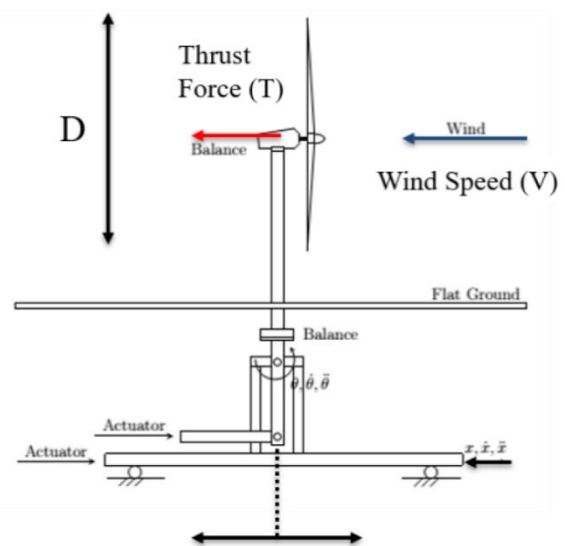
Figure 3.21 Wind velocity as percentage of maximum and Turbulence intensity in plane at MARIN's Offshore Basin [39]

### 3.2.2 Politecnico di Milano – Wind Tunnel

Contrary to the wind/wave setting expected for testing FOWTs, PoliMi uses a wind tunnel: the GVPM (Galleria del Vento del Politecnico di Milano) which incorporates a turn table that emulates two of the six D.o.F. of the floating platform, i.e. surge and pitch. As has already been discussed in chapter 2, pitch is the motion that has more significance when studying the impact of the floating dynamics on the aerodynamic performance of the turbine. Therefore, in order to reproduce this D.o.F., two hydraulic actuators were implemented that respectively move the model of the FOWT through a rail and enforce an oscillatory motion with a slider-crankshaft mechanism. Furthermore, the setting is fully instrumented with gauges that help measure the forces and moments at the tower base and at the rotor (thrust). Figure 3.23 displays the wind tunnel test setting with the 1/75<sup>th</sup> rotor in-house designed and introduced in the second part of section 3.1.3.



a. Wind tunnel test setting



b. Experimental scheme for pitch and surge motions

Figure 3.22 PoliMi Wind Tunnel [15]

Generally, wind tunnels operate on a larger wind speed regime than the ones encountered at a wind/wave basin, and this case is not an exception. The GVPM can develop at the two testing sections available, boundary layer and low-turbulence, 16 and 55 m/s respectively [15]. This turbine model was tested in the first section, for which the Reynolds numbers achieved were only 150 times lower than at full-scale. However, the testing wind speeds are considerably high, which oscillate between 2.33 and 8 m/s (or ~20 – ~69 m/s at full-scale in a floating

environment). This means, that in spite the success of this rotor on the wind tunnel it would not be feasible for testing floating platforms on a wind/wave basin since at these high wind speeds the drag force on the rotor would generate enough overturning moment to flip the platform over.

### 3.2.3 Technical University of Munich – Upward Moorings

Coupled to the Aerodynamic Scaling approach introduced in section 2.1.5, the TUM developed a consistent testing method to cope with the drawbacks of this methodology, which entails improving the restoring properties that affect directly the floating platform motions explained in section 2.3. In this sense, it was proposed that the mass per unit length of the downward moorings pertaining to the model subjected to analysis (NREL 5MW mounted onto the OC4 DeepCWind semi-submersible floating platform) was adjusted in order to effectively improve the surge behaviour (one of the 6 D.o.F. of platform motion described in section 2.3). Furthermore, it was introduced the idea of implementing upward moorings connected to the ceiling of the wave tank (see Figure 3.23) in order to increase heave ( $Z_p$ ), pitch ( $\theta_p$ ) and surge ( $X_p$ ) restoring properties as evidenced in the results from the simulations displayed in Figure 3.24 [16].

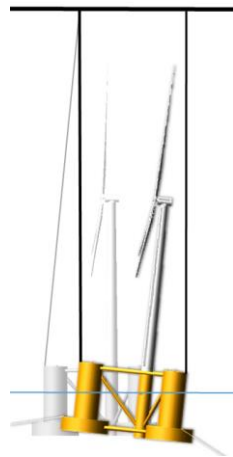


Figure 3.23 Testing model with upward ceiling moorings [16]

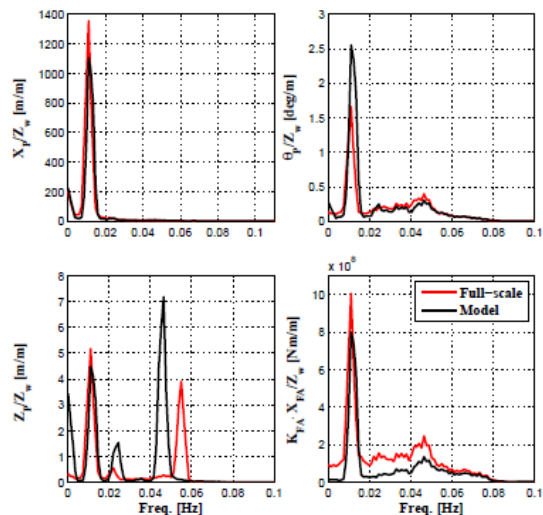


Figure 3.24 Dynamic response full- vs. aerodynamic-scaled model [16]

Although this proposed setting seems to have a positive impact on the floating motions, its implementation appears to be rather complex since there is always the likelihood that when the platform pitches abruptly the rotor may collide with the upward moorings. Unfortunately, the aerodynamic behaviour of the rotor when the aerodynamic scaling is applied is overlooked and not further investigated, which leaves the question of its benefits.

### 3.2.4 Ideol - Drag Disc

In order to reproduce the thrust forces that the rotor experiences, and that consequently are transferred to the floating platform in the form of surge and pitch motions, Ideol a French innovator on floating offshore systems, introduced the use of a drag disc instead. The solid disc will move backwards upon the effect of wind, inducing pitching of the platform as evidenced in Figure 3.25. In fact, it is possible to replicate closely the thrust for the range of full load wind speeds as presented in Figure 3.26. However, the implementation of such disc has some aerodynamic drawbacks. Since it cannot replicate the performance of the rotor when the blades are pitched for power control purposes, it is not possible to construct a power curve

from its characterization. Moreover, since the disc does not rotate it is not feasible to obtain the corresponding set of TSRs.

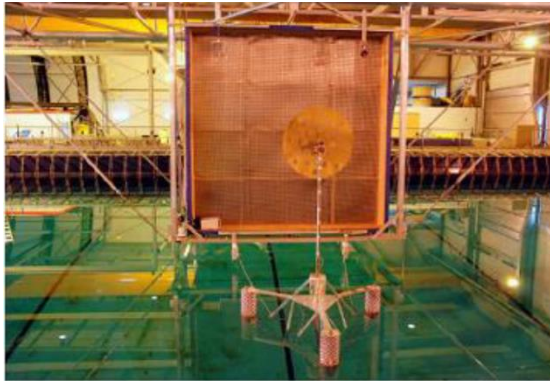


Figure 3.25 FOWT test setting with drag disc [53]

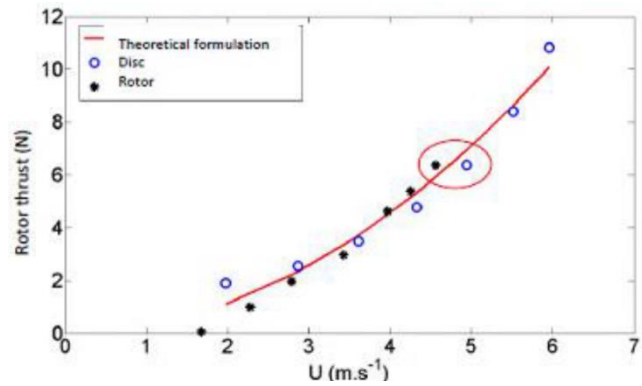


Figure 3.26 Thrust force behaviour for a rotor- vs. a disc-based FOWT test [53]

In addition, with respect to the hydrodynamics, it poses a disagreement on the surge and pitch platform motions in comparison with the traditional rotor-based test setting, when in low-frequency waves, as displayed in Figure 3.27. This overestimation is mainly due to the difference in aerodynamic damping.

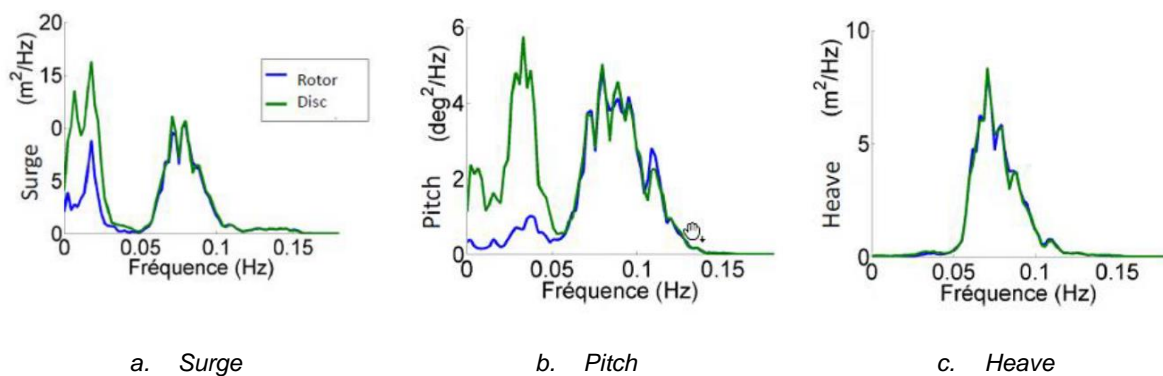


Figure 3.27 Platform motions vs. Wave frequency upon wind/wave effect [53]

### 3.2.5 CENER - Ducted fan

Sharing the goal of reproducing the thrust forces as accurate as possible, CENER (Spain's National Renewable Energy Centre) has implemented the ducted fan mechanism for FOWT tests, as shown in Figure 3.28. This system comprises a high-thrust fan-brushless-motor assembly, controlled in such way that the thrust generated by the turning fan induces a downwind motion on the floating platform. In order to establish the exact rotational speed of the fan, a software-in-the-loop (SIL) control has been designed. This takes into account the full-scale wind conditions and the performance of the rotor to be emulated to the end of, by means of scaling-down, translating into aerodynamic thrust, as seen in Figure 3.29. This allows wave tank testing without the need of wind generation.



Figure 3.28 Ducted-fan-based FOWT test [45]

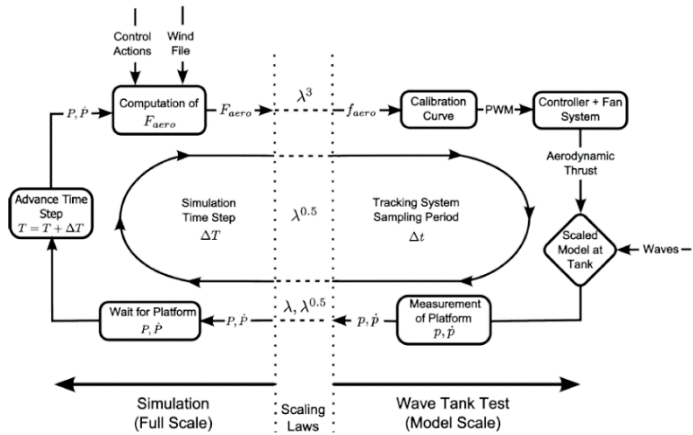
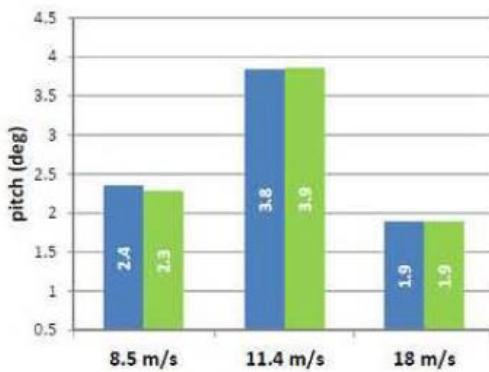
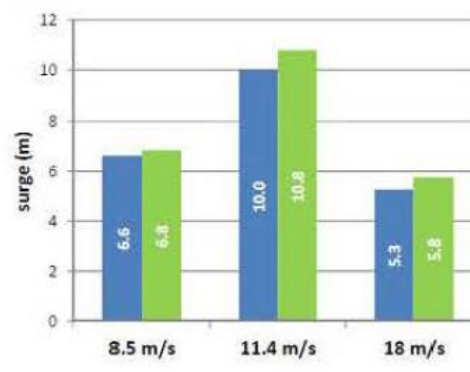


Figure 3.29 Software-in-the-Loop for fan control [45] [54]

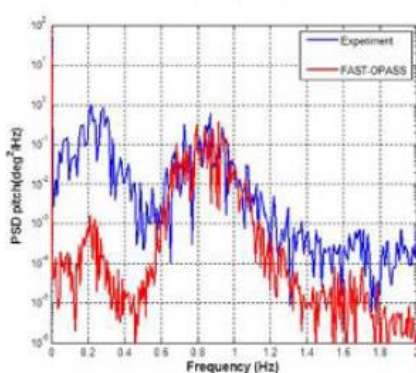
In addition, Figure 3.30 shows the comparison between the simulated pitch and surge motions for a semi-submersible 5MW FOWT model test. It is there shown that the difference is comparatively low. However, when irregular waves are incorporated, there is a clear mismatch at low frequencies (<1 Hz) between the experiments and FAST simulations, mainly due to second-order hydrodynamic effects. Nonetheless, this is a low-cost quick-installation method suitable for FOWT testing. The main drawback for the scope of this present work is that given that most of these tests are performed on a commercial basis, the fan is not as attractive as a wind turbine-alike rotor and its calibration may present some challenges.



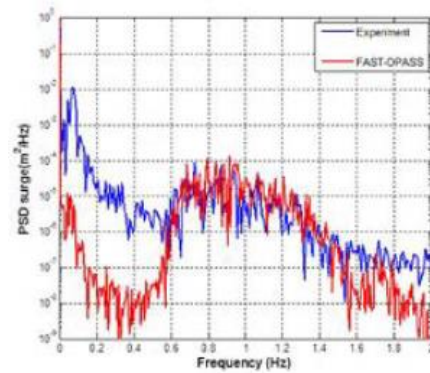
a. Pitch at constant wind and regular waves



b. Surge at constant wind and regular waves



c. Pitch at constant wind and irregular waves



d. Surge at constant wind and irregular waves

Figure 3.30 Ducted-fan-based representative floating platform motions [55]

### 3.2.6 IHC – Multi-fan

Similar to the ducted fan concept introduced before, researchers at IHCantabria (Environmental Hydraulic Institute of the University of Cantabria in Spain) have come up with an innovative way for modelling wind loads and platform motions simultaneously. This is achieved by means of six independent electrically-driven-fans, displayed in Figure 3.32. These are able to face every direction (360° range) in- and out-of-plane, in order to emulate the thrust, pitch and surge altogether. The multi-fan concept has been implemented in the testing of the TELWIND Project, which is an innovative support structure concept, especially developed by ESTEYCO that comprises a spar-type floating platform consisting of a floater and a ballast attached by tendons, and a self-erecting telescopic tower [56] as evidenced in Figure 3.31.



Figure 3.31 TELWIND FOWT support structure concept [56]

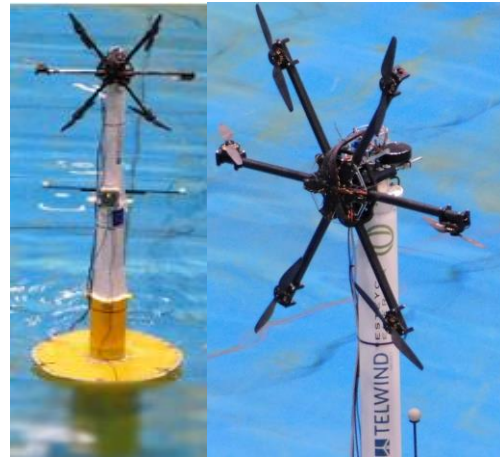


Figure 3.32 IHCantabria Multi-fan FOWT testing concept [56]

The advantages of this testing method are numerous: first, thrust and torque can be adequately modelled for any wind turbine including the control system since negative aerodynamic damping can be reproduced. Furthermore, it is suitable for wave tank testing without the need for implementation of wind generation (constant or turbulent). In addition, gyroscopic loads can be emulated thanks to the vertical fans. Moreover, it is considered to be flexible with regard to scaling factors, in addition to being lightweight. Nonetheless, this testing exercise has proven that its implementation is rather complex with respect to the sensible mechanic and electronic system, its calibration, communication and power supply. This latter is because the amount of cable used is too large and can generate extra undesired weight [56]. Unfortunately, there is not yet conclusive data on its performance related to thrust, pitch and surge; thereby it is still uncertain its behaviour for further implementation.

### 3.2.7 MARIN - Winch-controlled

To the end of reproducing all six D.o.F. of the floating platform, MARIN proposes that six wires are attached to a plate that resembles the wind turbine rotor plane as shown in Figure 3.33. These wires are pulled with a particular tension back and forth depending on the load required to be exerted, based on SIL calculations from FAST (or equivalent) [57], as evidenced in Figure 3.34. With this, the thrust, aerodynamic damping, drag on the tower and the gyroscopic effects are accounted for, unlike the static cable system implemented in 2010 – 2014 by IHC where wires were held static by suspended weights in a pulley mechanism. This meant that there was a lack of control or accountability for wind variability and the platform response was not taken into consideration, aside from inertial issues.

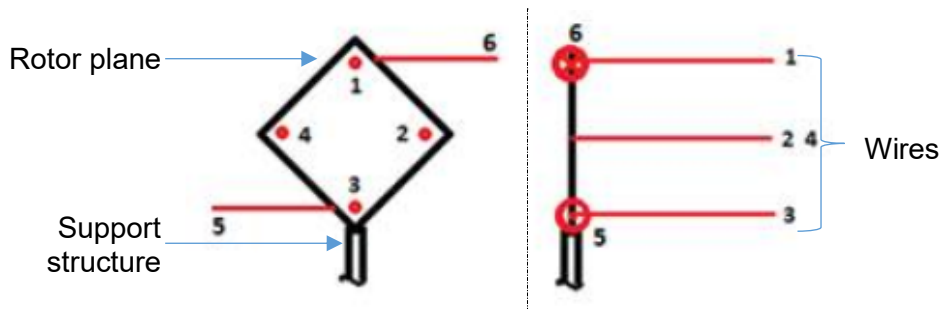


Figure 3.33 Representation of a 6-wire winch-driven load control system [57]

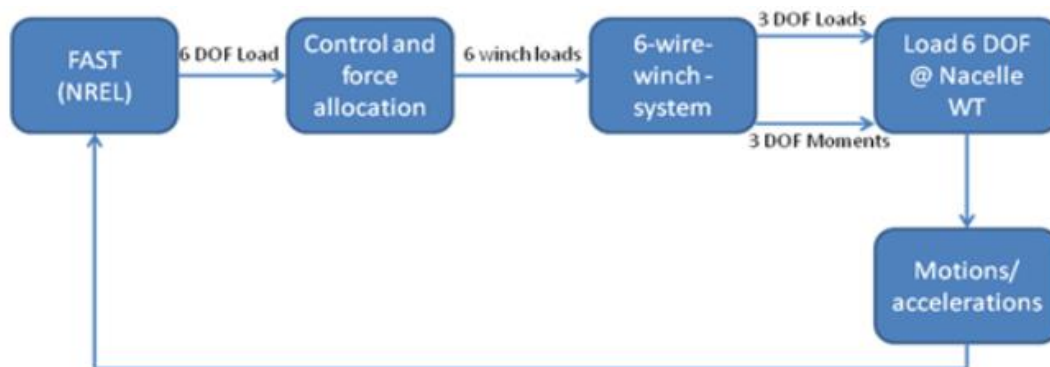


Figure 3.34 SIL for 6-wire winch-driven load-control system [57]

The success of this concept relies on the accuracy of the loads being computed and further transferred to the wire by means of the tools and scaling factors, and of the control system that manages the tension of the wire, which can be a challenging combination.

### 3.2.8 Final Remark

Though very innovative testing methods have been implemented, they have not been perfected yet to the extent of recreating all the conditions present at full-scale. For instance, although in a wind tunnel setting the wind speeds are suitable for representing the aerodynamics, they are far too high for a floating setting emulation. On the other hand, the drag disc does not allow to be controlled, i.e. there is no possibility to pitch the blades as in the real case scenario and hence, no power curve can be derived. Furthermore, the ducted-, multi-fan, and the winch-controlled settings pose challenges when it comes to calibration. For the aforementioned reasons, it is valid for the purpose of this study to respect the wind/wave basin-based testing since is the environment that provides more accuracy.

# 4 Methodology for Rotor Blade Design

The theoretical and design concepts introduced so far serve as the foundation for establishing the blade design procedure, which is one of the main objectives of this work. For this purpose, in section 4.1 the problem is defined along with its corresponding variables. Furthermore, the design steps and subsequent flowchart is proposed in section 4.2. Moreover, in succeeding section 4.3 specific design tools to be implemented are described along with their corresponding validation. Finally, this is also done in section 4.4 for the tools selected for further check of the results.

## 4.1 Problem Definition and Optimisation Model

As seen from previous exercises, the main goal for developing a wind turbine rotor blade to be employed in the testing of FOWTs (in a wind/wave basin) is to reproduce at model-scale the non-dimensional axial aerodynamic forces, i.e. thrust and its corresponding coefficient ( $C_T$ ) acting upon the rotor at full-scale. Nevertheless, in order to properly match this parameter, this must be done for every TSR; taking into account that the rotational speed increases and the velocity decreases when Froude-scaled. This is relevant since thrust is then transferred in the form of overturning moment on the floating platform, hence affecting its behaviour and therefore, its final design. Considering that, for a testing model the power generated has little or no effect over the platform behaviour, the non-dimensional power, i.e. power coefficient ( $C_P$ ) is taken as a secondary objective, hence trying to get as close as possible.

To the end of achieving such parameters through the design of the rotor blade, its geometry needs to be defined in terms of spanwise chord, twist and thickness distributions. Generally and for this purpose, multi-objective optimisation models are implemented. In this case the goal is to minimise the sum of all individual differences between the current blade aerodynamic performance parameters and the reference values ( $C_{T,ref}$  &  $C_{P,ref}$ ), obtained from full-scale characterisation, at every TSR [36, 58].

Nonetheless, in this case, the TSR values from full-scale are intrinsically guaranteed at all time since the pitch, and rotational speed strategy is imposed for every wind speed (with the range between cut-in and cut-out), which basically is the function of the active-pitch controller (assumed to be Collective Pitch Control – CPC). Therefore, the optimisation model is transformed as a function of wind speeds ( $U_i$ ) instead of TSRs as displayed in (4.1). The motivation behind this setting is mainly because usually floating platform test campaigns are carried out with the customer's specifications, which may include a proprietary controller. This way, there is freedom to input such strategy. In addition, it can be noted from the model presented below that the chord ( $c$ ) and the twist ( $\theta$ ) are bound by lower and upper limits and vary for every radial position ( $r$ ) from the hub radius ( $r_{hub}$ ) until blade length ( $R$ ).

$$\left\{ \begin{array}{l} \min \sum_i C_T(U_i) - C_{T,ref}(U_i), \forall U_{cut-in} \leq U_i \leq U_{cut-out} \\ \min \sum_i C_P(U_i) - C_{P,ref}(U_i), \forall U_{cut-in} \leq U_i \leq U_{cut-out} \end{array} \right. \quad (4.1)$$

*subject to:*

$$\left\{ \begin{array}{l} c_{min}(r) \leq c(r) \leq c_{max}(r), \forall r_{hub} \leq r \leq R \\ \theta_{min}(r) \leq \theta(r) \leq \theta_{max}(r), \forall r_{hub} \leq r \leq R \end{array} \right.$$

## 4.2 Design Procedure

Bearing in mind the main goal described in previous section, the design procedure is built around it, which is described in this section. The steps are detailed as follows:

### *Aerofoil Disaggregation*

First, since the BEMT is to be applied in order to determine the aerodynamic performance of the turbine with the implementation of the rotor blade designed, a disaggregation of the blade into individual aerofoils is necessary. This is done for a certain number of geometries that is statistically significant, each one discretised in 12 nodes, which as will be further seen, requires low computational effort and does not degrade the quality of the results. As seen from previous experiences, the aerofoils resulting from this break-down should be thin compared to the ones employed at full-scale, and with large Lift-to-Drag ratio at low Reynolds numbers.

### *Aerofoil Analysis*

Then, with the individual aerofoils at hand, the corresponding analysis is performed. That is, to find the lift and drag coefficients for the complete range of angles of attack (polars), which depend on the Reynolds number, in this case low at model-scale. This is done incorporating the rotational effects.

### *Preparation of Inputs for BEMT*

Furthermore, once the polars are complete, a set of files is prepared in order to be read and further processed by the code that incorporates the BEMT. For this purpose, a set of instructions is provided: among others, the time of the simulation, the flexibility of the components, the overall setting (onshore as opposed to floating as seen in section 2.3.2), the corresponding wind speed, blade pitch, rotational speed and of course the aerofoil discretisation.

It is important to notice here that the simulations are run at full-scale, which means that even though the current blade design will be realised at model-scale, it needs to be scaled back at full-scale, while the polars remain consistent with low-Reynolds numbers.

### *Simulations with BEMT*

With this information, it is possible to apply the BEMT and establish the aerodynamic performance of the rotor, i.e. the thrust and power, and consequently their respective non-dimensional coefficients. This is done several times for the same turbine under different wind speeds, associated to blade pitch and rotational speed combination, in order for the resulting blade to be able to perform in all operating conditions.

### *Check of Preliminary Results*

Now, once the thrust and power coefficients are obtained, they are further compared against the reference values, which for this case are the simulated  $C_T$  &  $C_P$  curves vs. wind speed for the DTU 10MW. From this comparison the sum of all differences is the value of interest, which when a minimum is reached, it can indicate a match and therefore, the design is ready to be verified on its performance.

### *Verification of Performance*

If a match is achieved, then it is relevant to verify the reproducibility of such the aerodynamic performance by carrying out computation with an alternate method such as CFD 3-D. This

allows to determine if the results from BEMT are reasonable, assuming that CFD gives, in general, better accuracy.

### Optimisation

On the other hand, if no match is achieved for any of the geometries, then they are ranked and the best features are combined in order to create a new set of improved chord and twist distributions. For this purpose, a genetic algorithm is employed.

### Geometry Generation

With the aforementioned distributions, a group of geometries is generated, which are the new input for the design loop as depicted in Figure 4.1.

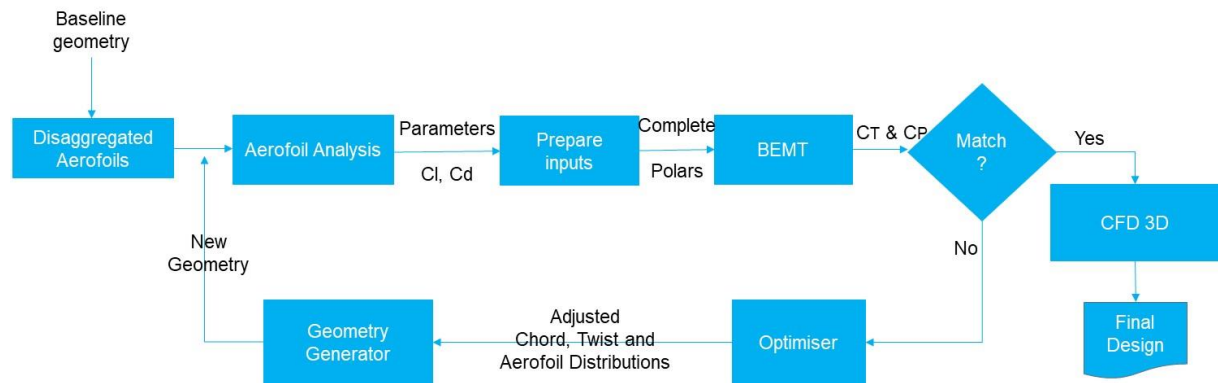


Figure 4.1 Flowchart implemented for wind turbine rotor blade design for testing of FOWTs

## 4.3 Design Tools

In order to enable the previously established design flowchart, appropriate computer-aided engineering (CAE) tools are needed, which are listed in Table 4.1.

Table 4.1 Implemented Tools in the Design Loop

Stage	Tool	Use	Version	Developer
Design	RFOIL	Aerofoil analysis and design	1.1	ECN, TU Delft & NLR
		Aerofoil analysis and design (XFOIL)	6.99	Mark Drela
	AirfoilPrep	Polars extrapolation	2.02.03	NREL
	FAST	Aero-servo-elastic code for WT	8.12	NREL
		Aerodynamics through BEMT (AeroDyn)	14.04	
	PropArt	Optimisation, geometry generation and blade disaggregation	1.0	MARIN
Validation	ReFRESKO	CFD 3-D calculations	2.3.0	MARIN
Pre-processing	Rhinceros	Import PropArt geometry (plugins)	1.5.6	MARIN
		RNA, surface and domain definitions	5.0	Robert McNeel & Associates
		Automate the process (Grasshopper)	0.9.76.0	NING
	HEXPRESS	Meshing	6.2	NUMECA International
Post-processing	Tecplot	Visualisation of results	360 - 2013	Tecplot
	Paraview	Visualisation of results	5.3.0	Kitware

### 4.3.1 RFOIL

#### Selection criteria

RFOIL is an extension of the well-known XFOIL code originally developed by Mark Drela from MIT in 1986, whose purpose is to aid in the design and analysis of individual aerofoils working in a subsonic regimes [40]. Among its numerous capabilities, the most commonly used is its ability to predict lift, drag and pitching moment coefficients, and establish the points in the pressure and suction sides of the aerofoil at which laminar separation occurs, by varying the A.o.A. In addition, these polars can be written to a proper file. The main consideration used by XFOIL is the 2-Dimensional flow, which limits its application for rotating blades. This is why for wind turbine blade design there is the need for 3-D flow corrections, as illustrated in section 2.2.2. Since its development, many other codes have been implemented with the same goal, such as ProFoil, XFLR5 and JavaFoil.

RFOIL, on the other hand, was adjusted by the Energy research Centre of the Netherlands (ECN), Delft University of Technology (TU Delft) and the Netherlands Aerospace Centre (NLR) in 1997 with the aim of incorporating the 3-D effects for rotating aerofoil. For this purpose, the Snel & van Bussel's correction was implemented, which allows the calculation of aerodynamic coefficients near stall by taking into account the rotational (Coriolis) effects [59]. This is done by means of including the local solidity  $c/r$  of the section (introduced in section 2.3.2) and the dimensionless free-stream velocity  $f_0$ , defined as:

$$f_0 = \frac{V_{rel}}{\Omega \cdot r} \quad (4.2)$$

In addition, according to experimental data RFOIL's computations give better agreement when taking 2/3 of the local solidity [59]. In order to visualise the difference in performance between XFOIL and RFOIL, Figure 4.2 shows comparatively the pressure coefficient distribution for the NACA 4415 aerofoil, yielded from the analysis without and with rotational effects (outboard radial position). From this, it can be carefully observed that around mid-chord, separation bubbles appear as a result of the 3-D effects.

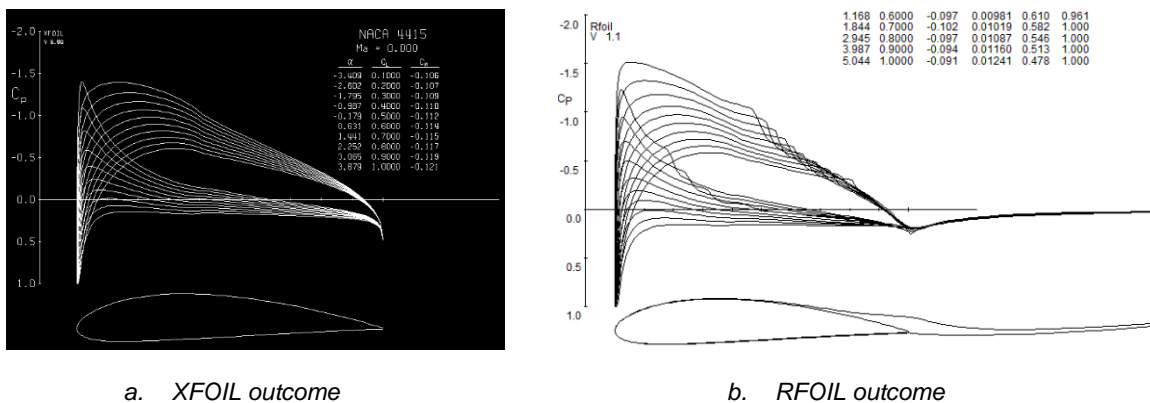
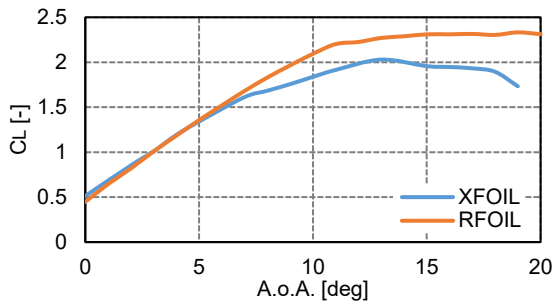
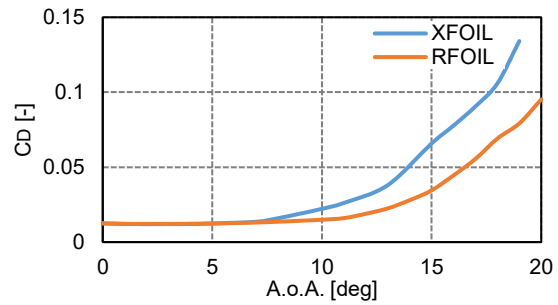


Figure 4.2 Layouts of XFOIL and RFOIL analyses of the NACA 4415 aerofoil

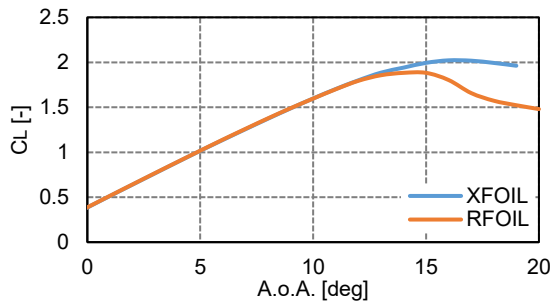
This fact can be corroborated via Figure 4.3, which displays the lift and drag coefficients for inboard and outboard aerofoils, FFA-W3-480 at 23% and FFA-W3-241 at 96% respectively used in the definition of the DTU 10MW blade. It is evident that at inboard positions the stall is delayed, which is seen as an increase in the lift coefficient in RFOIL with respect to XFOIL. On the other hand, when looking at the outboard aerofoil, the stall occurs earlier (anticipation) as predicted by the theory presented earlier. These computations were performed at rated wind speed (11.4 m/s) using the data consigned in Table 4.2.



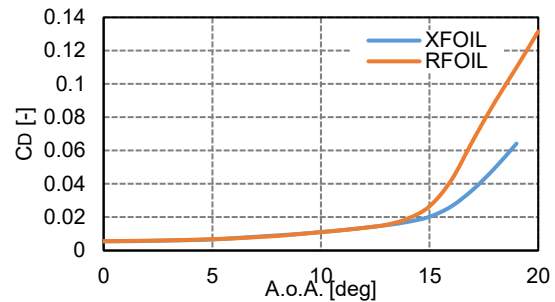
a. Lift coefficient FFA-W3-480 inboard aerofoil



b. Drag coefficient FFA-W3-480 inboard aerofoil



c. Lift coefficient FFA-W3-241 outboard aerofoil



d. Drag coefficient FFA-W3-480 outboard aerofoil

Figure 4.3 Comparison aerodynamic coefficients for inboard and outboard aerofoils using RFOIL vs. XFOIL

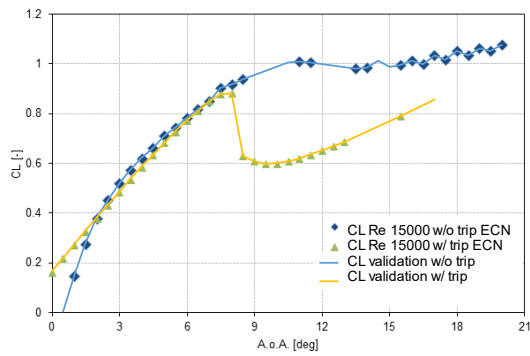
Table 4.2 Inboard and outboard aerofoils simulation conditions

Aerofoil	Radial position [m]	Reynolds Number [-]	$f_0$ [-]	$\frac{2}{3} \cdot \frac{c}{r}$ [-]
FFA-W3-480	20.8	$12.3 \times 10^6$	1.31	0.195
FFA-W3-241	85.6	$13.7 \times 10^6$	1.24	0.014

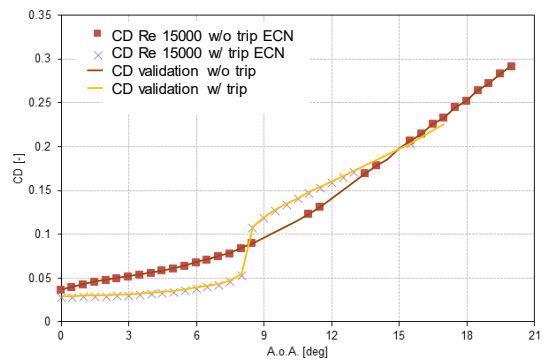
From the above-mentioned evidence, RFOIL is chosen over XFOIL as it is more suitable for wind turbine blade design.

#### Validation of RFOIL

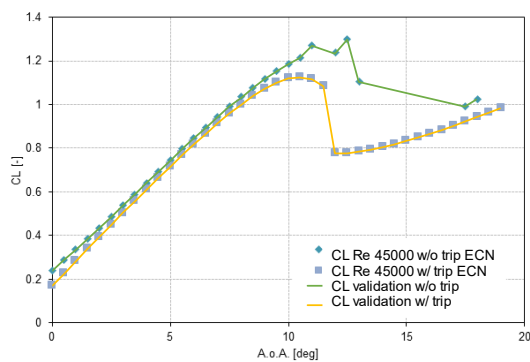
Once selected the tool suitable for aerofoil analysis, it is important to establish if it is capable of replicating a set of data obtained from a previous experience. This is to gain confidence in the tool prior its integration into the design loop. For this purpose, a validation exercise was performed against a previous aerofoil analysis done by ECN of the modified version of the Drela AG04 implemented in the MSWT, as discussed in section 3.1.2. In this case, the polars were obtained for two Reynolds numbers 15,000 and 45,000 under two assumptions: with and without tripping strips (at 5% from the leading edge on the top and bottom sides), which are used to create turbulence at an early stage in order to re-energise the boundary layer. This is relevant because the flow gains sufficient momentum to overcome the pressure gradient and thereby will remain attached to the aerofoil's surface. Figure 4.4 shows all four cases depicted as markers and their corresponding validations with continuous lines.



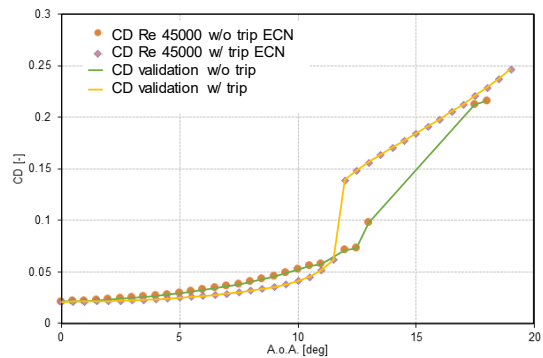
a. Lift coefficient Re 15,000 with and without tripping



b. Drag coefficient Re 15,000 with and without tripping



c. Lift coefficient Re 45,000 with and without tripping



d. Drag coefficient Re 45,000 with and without tripping

Figure 4.4 Validation of RFOIL for modified Drela's AG04 aerofoil

From this validation exercise, it can be noted that a perfect match was achieved with respect to ECN's results, which means that they are highly reproducible. In addition, it can be evidenced that this particular tripping scenario is not always the best alternative for attaining better aerodynamic performance since the lift drops earlier than it should and consequently the drag rises. Another location for tripping might be considered; however, in order to avoid the implementation of such strips a clean blade is hereinafter considered in this work.

In order to automate the process, the RFOIL batch version provided by TU Delft is used, which will allow to run simultaneous aerofoils, thus making the optimization process more efficient.

### 4.3.2 AirfoilPrep

Currently, there is no aerofoil analysis tool available capable of providing the full range of polars ( $-180^\circ$ ,  $180^\circ$ ), therefore, there is the need to extrapolate the coefficients obtained in order to fulfil the BEM code requirements. For this purpose, NREL developed a tool on both Microsoft® Excel and Python platforms with several features that include: 1) interpolation function for creating uniform lists of  $C_l$  and  $C_d$  obtained discontinuous range of angles; 2) blending aerofoils for creating intermediate blade sections; 3) application of Selig & Du 3-D corrections; 4) extrapolation of polars to a full range; 5) computing dynamic stall parameters required by the BEM code; and 6) it displays the respective BEM input file in a text format. In this case, the last three are considered useful.

For the extrapolation procedure, the worksheet allows to choose between the Viterna and the flat plate approaches. As seen before in section 2.2.2, the Viterna method is the most commonly used in the wind turbine design field. Therefore this is the most consistent choice. Moreover, the maximum drag coefficient is varied according to the blade element aspect ratio (AR), described by equation (4.3), as the ratio between the span  $S$  and the chord  $c$ . However since the range beyond stall is out of the pitch range, the default values are kept to 1.29 as a result from an AR of 10.

$$AR = \frac{S}{c} \quad (4.3)$$

Regarding the dynamic stall calculations, mainly the normal and tangential coefficients ( $C_n$  &  $C_t$ ) rely on a linear approximation based on two points in the attached flow regime and the stall angle. The latter is taken as the corresponding positive value in the independent axis at which the first maximum lift coefficient occurs. From these assumptions, the Zero  $C_n$  angle of attack, the  $C_n$  slope at zero lift, the  $C_n$  extrapolated to value at positive stall angle of attack, the angle of attack at minimum  $C_d$  and the minimum  $C_d$  value can be obtained. Furthermore, the last worksheet takes the previous outputs and integrates them into a readable text.

#### Validation of AirfoilPrep

As done previously for RFOIL, results obtained through AirfoilPrep need to be validated against known results. Therefore, the polars obtained by DTU for the FFA-W3-241 aerofoil implemented in the blade of the DTU 10MW is employed for comparison purposes. These were acquired using EllipSys 2-D, an in-house CFD code for angles of attack in the range  $(-32, 32)$  and further applying Bak & Johansen's (also in-house) 3-D correction method [60]. The extrapolation method used was the flat plate and then smoothed manually. For this purpose, the set of results for the FFA-W3-241 (outermost) aerofoil serve as a benchmark for comparing the extrapolation done with AirfoilPrep.

For that purpose, these values are entered and the maximum  $C_d$  is adjusted to 1.5 in AirfoilPrep. Figure 4.5 shows the comparison of extrapolated lift and drag coefficients. Even though there is a mismatch in the lift extrapolation, the drag matches almost perfectly. This is due to the difference in nature of the extrapolation methods, which cannot be investigated because of the lack of information on the smoothing procedure done by DTU. Nonetheless, provided that the purpose here is to establish the reliability of the tool, it is without a doubt that AirfoilPrep's extrapolation feature is able to perform its task for any range of polars.

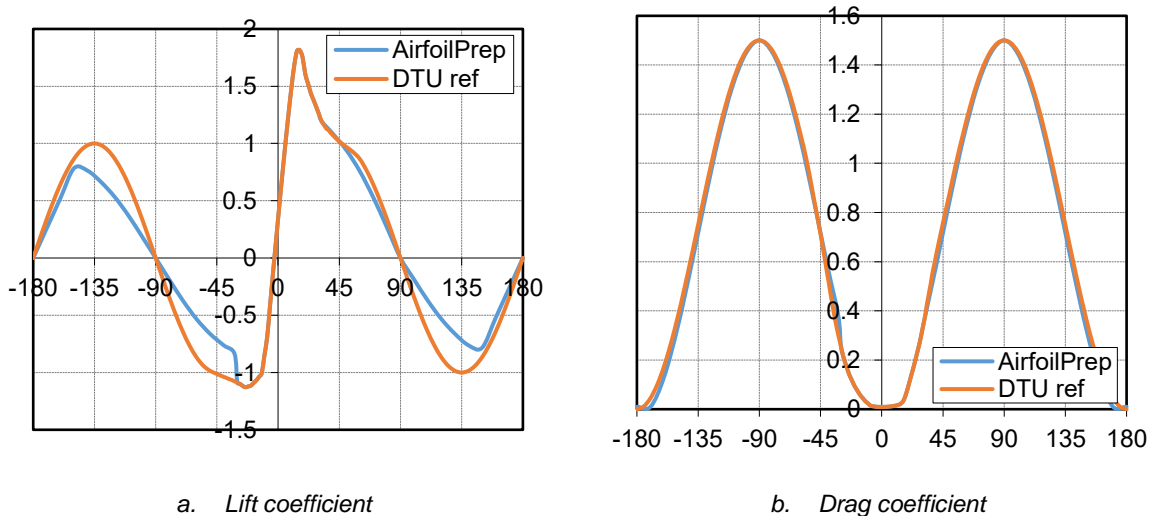


Figure 4.5 Validation of AirfoilPrep extrapolation feature for FFA-W3-241 aerofoil

### 4.3.3 FAST

FAST (Fatigue, Aerodynamics, Structure and Turbulence) is an aero-servo-hydro-elastic open-source HAWT simulator developed by NREL. Its purpose is to determine the dynamic response of the turbine in the time domain through the integration of several sub-routines. For instance, AeroDyn takes care of the aerodynamics; InflowWind of the wind characterisation; ElastoDyn and BeamDyn of the structures (blades and tower); HydroDyn and SubDyn of the hydrodynamics of the offshore support structure; ServoDyn of the control and electrical system; MoorDyn of the FOWT platform; IceDyn of the ice loading on the support structure, and so on [61]. This coupling enables a broad range of configurations, e.g. two- or three-bladed configuration; pitch or stall control; upwind or downwind; uniform and steady or wind shear; tubular or lattice tower; floating or bottom-fixed support structure.

One of the most relevant sub-routines, suitable to be employed in this work is AeroDyn, which is in charge of applying the BEMT on the rotor, based on a blade discretisation. AeroDyn incorporates rotor-wake effects, dynamic stall, tip and hub losses, which makes it accurate enough for its broad implementation. In complement, ElastoDyn plays a significant role since it helps manipulate the initial conditions for blade. This is: the turbine configuration; the active D.o.F.; the blade and tower distributed properties such as various types of stiffness, inertias and local density; and the outputs of interest. Furthermore, InflowWind aids in defining the wind speed or the wind profile, including turbulence to be used throughout the simulation.

There have been many developments of wind turbine simulators over the years, but only a few of them are open-source codes and further less are proven to be reliable. That is why in 2005 FAST (with AeroDyn) was conceded an evaluation certificate issued by the well-known wind turbine certification entity Germanische Lloyd (GL). These aforementioned reasons are the ground for selecting FAST over other codes, such as, e.g. Bladed (from DNV-GL, originally from GL Garrad-Hassan), HAWC2 (Horizontal Axis Wind turbine simulation Code 2nd generation - from DTU Wind), SIMO/RIFLEX (from MARINTEK) [62], PropID (by the UIUC) [41] or even QBlade (from TU Berlin).

#### *Validation of FAST*

With the purpose of establishing whether FAST is capable of reproducing the results obtained in a particular simulation campaign or if possible in a test campaign, a validation exercise is required. To this end, a comparison is made on the aerodynamic performance of the DTU 10MW. To achieve this, the reference values were obtained from the DTU 10MW project repository, which contains all sort of information such as 2-D and 3-D CFD models; aeroelastic models (FAST and HAWC2); aerofoils coordinates; CAD designs, and structural models. In addition, it incorporates a full description of the turbine with valuable information, e.g. general properties, steady state operational data (pitching vs. rotational speed strategy for every wind speed); complete aerofoil polars; blade's structural properties; and chord, twist, pitch axis and relative thickness distributions [60].

DTU used EllipSys 2-D for the polars of the aerofoils at fixed Reynolds numbers:  $6 \times 10^6$  for the FFA-W3-600,  $10 \times 10^6$  for the aerofoils from FFA-W3-480 to FFA-W3-301 and  $12 \times 10^6$  for the tipmost, even though as it will be seen in section 5.2.3, it can achieve higher values. Furthermore, Bak & Johansen's 3-D correction method was applied, and the flat-plate approach extrapolation model introduced in section 2.2.2 was used. Finally, HAWC2 (HAWCStab2 sub-routine) was employed as the in-house BEMT code, optimising the design at a TSR of 7.5.

Within the current work, a coarser blade discretisation was used, which comprises 12 nodes as opposed to the original finer version. This was a result from a variable optimisation, further described in section 5.2.1 and illustrated in Figure 4.9. On the other hand, RFOIL was used

instead of EllipSys2-D to obtain the polars incorporating the corresponding local solidity criterion ( $2/3$  of the  $c/r$ ) and the corresponding dimensionless free-stream velocity  $f_0$ . In addition, AirfoilPrep was employed for extrapolating the aforementioned polars into the full range using Viterna's approach. With the help of AirfoilPrep's final feature described in previous section, the aerofoils' input files are created in order to be read and processed by AeroDyn sub-routine. The main parameters for the validation simulations are listed in Table 4.3 below.

Table 4.3 FAST validation simulation parameters

Parameter	DTU Simulations	Present Work
Wind speed range	4: 1: 25 m/s	4: 2: 24 & 11.4 m/s
Wind state	Uniform and steady	
Blade condition	Rigid non-pre-bent non-coned no-rotor-shaft-tilt	
Controller	Active pitch	Imposed pitch and RPM
Polars	(-32, 32)	(-10, 35) to achieve convergence
Gurney Flaps	Yes	No
Tower interaction	No	No

In consequence, as a result of the BEMT (RFOIL-FAST) computations, Figure 4.6 illustrates the steady-state response for the aerodynamic power and thrust, and subsequently, the associated non-dimensional coefficients for the discrete wind speeds indicated in the table above. For validation purpose, a comparison is made with respect to the DTU's BEMT and CFD calculations performed with HAWC2 and EllipSys3-D respectively.

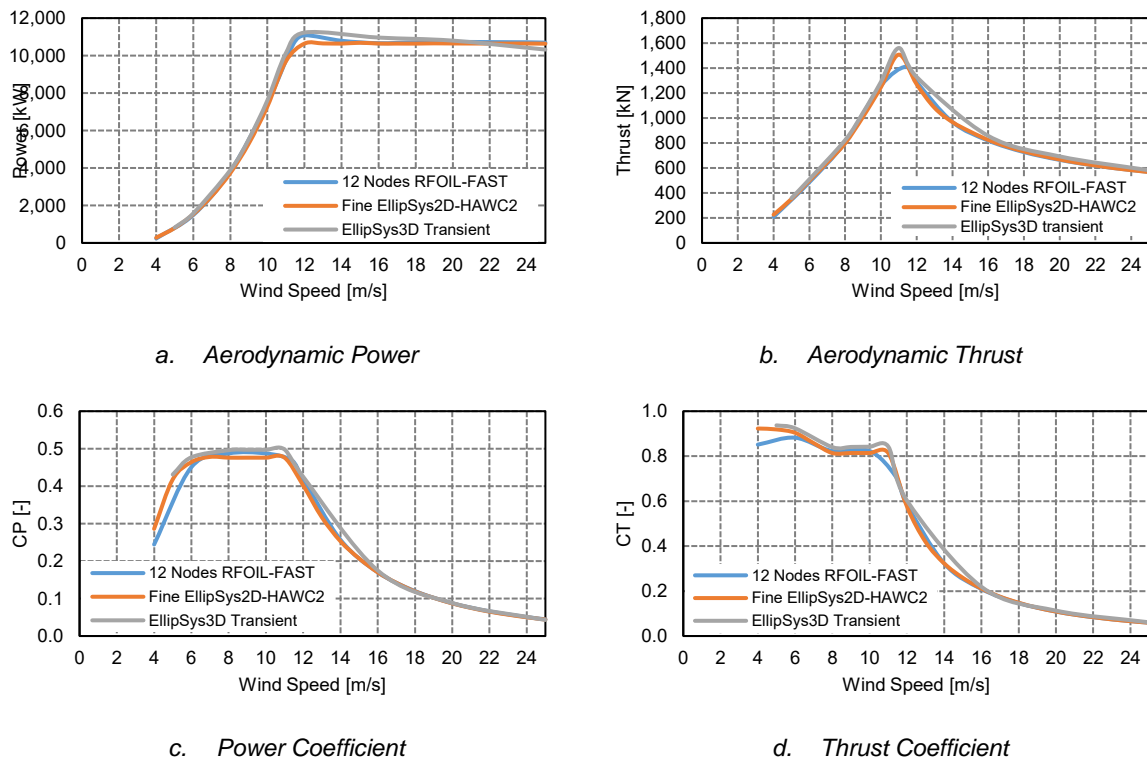


Figure 4.6 Validation of FAST aerodynamics for the DTU 10MW

The results from the first two sub-figures show good agreement for most of the wind speeds analysed; the main difference can be seen in the power and thrust at rated wind speed. This is mainly because the wind speeds subjected to analysis do not coincide in all three approaches. In addition, as for the non-dimensional coefficients, the differences at below-rated wind speeds, particularly at 4 and 6 m/s, obey to a subtle underestimation of the power and

thrust by FAST, which can be caused by many factors in the pre- and processing itself. Although not significantly, EllipSys3-D overestimates the performance in every case. Nonetheless, due to its apparent ability to perform accurate predictions of aerodynamic performance, FAST is considered to be validated for its further implementation in the design loop.

#### 4.3.4 PropArt

Moving on into the subsequent steps of the design loop from Figure 4.1, MARIN has developed a tool called PropArt capable of generating and optimising a blade geometry based on a predefined objective function. It is a Matlab-based code that uses splines to parametrise a geometry and incorporates a multi-objective Non-dominated Sorting Genetic Algorithm (NSGA-II) for the optimisation. Its main application is the propeller design. However, it has been adapted especially for this project with the aim of describing the geometry of a wind turbine rotor blade.

##### *Principles of operation*

Spline is a set of second-order polynomial functions used to explain the curve contained between 2 points [63]. In this case, the chord, twist, thickness, skew, rake and camber discrete distributions are converted into splines for plotting purposes. Furthermore, for the sake of the optimisation, the chord ( $c/R$ ), twist and relative thickness ( $t/c$ ) distributions are described via Bézier curves, specifically the linear type. The principle behind it is to define control points, which when moved change the beginning, end and curvature of a specific section [63]. Figure 4.7 illustrates this with an example of the parametrisation done for the DTU 10MW. The more points, the better accuracy is achieved but higher computational effort is required. Therefore, a low amount of points to describe every curve is chosen.

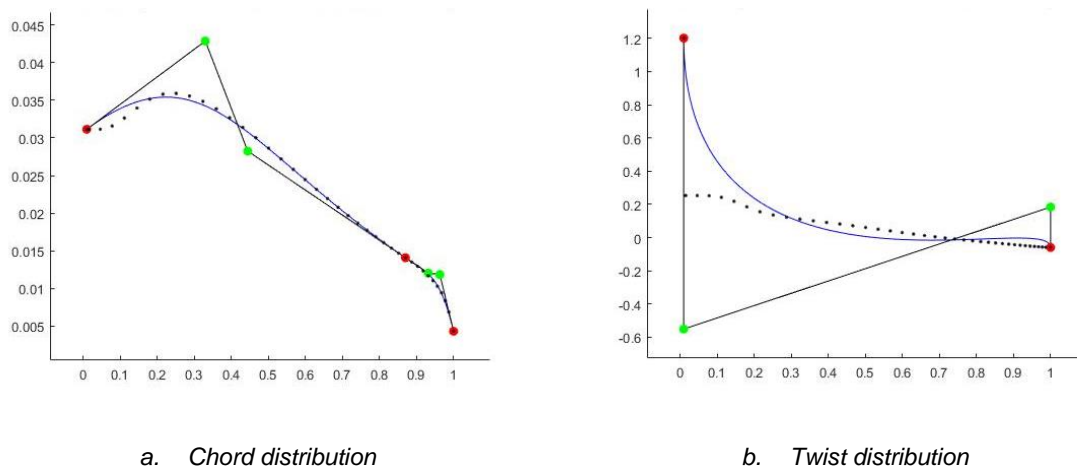


Figure 4.7 Bézier parametrisation of representative variables for DTU 10MW

Now, the NSGA-II has various functions: 1) to move these control points accordingly within predefined boundaries; 2) to sort the individuals based on their performance on their objective functions (most suitable solutions: elitism); and 3) to mate them (combine their properties: genetics). The non-dominating feature of this algorithm refers to the fact that there is no solution that optimises all objective functions, therefore one or more of them is degraded when improving another one. These solutions are placed in the so-called Pareto optimal solution front. The advantage of this method is that the Pareto-optimal front becomes more populated than other multi-objective genetic algorithms [64]. Therefore, there are more solutions to choose from as seen in Figure 4.8.

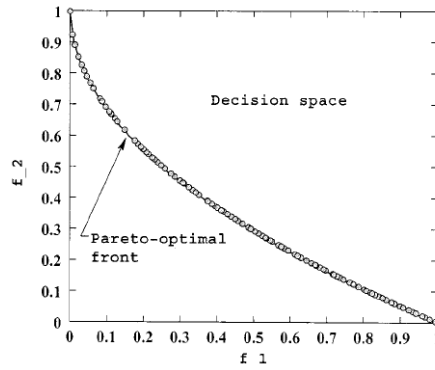
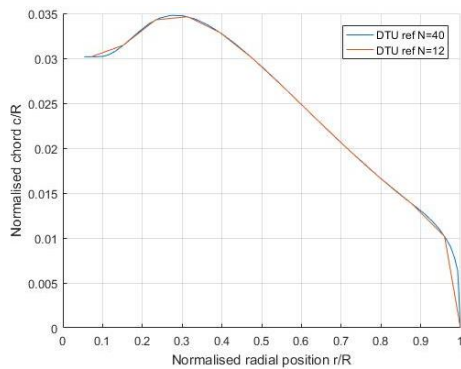


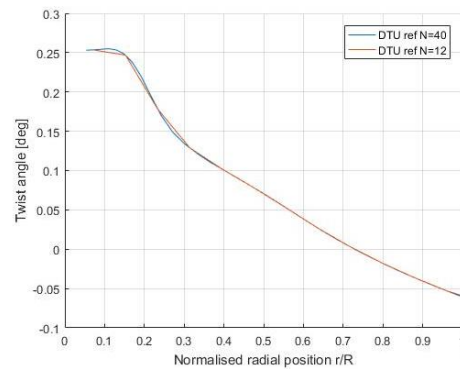
Figure 4.8 Pareto-optimal front [64]

### Validation of PropArt

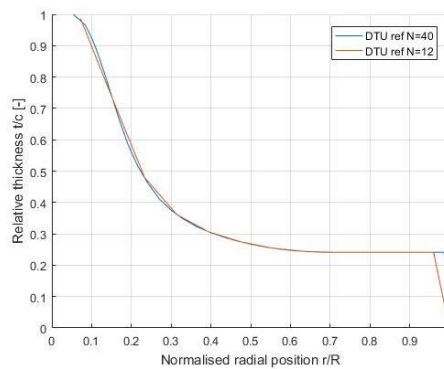
With the aim of getting acquainted with PropArt's capabilities of generating geometries accurately, the parametrisation of DTU 10MW blade was done by adapting its description to the terminology used in the propeller's field. For this purpose, the information consigned in DTU's repository was employed, which as mentioned comprises extensive data including the chord, twist, pitch axis and relative thickness distributions for coarse (N=40) and fine (N=200) discretisations [60]. Figure 4.9 shows such distributions for two different refinements, the original (of 40 nodes) and the reduced one (of 12 nodes equally distanced). The latter is hereinafter employed in order to reduce computational effort due to the large number of simulations to be run.



a. Chord distribution vs. Normalised radial position



b. Twist angle distribution vs. Normalised radial position



c. Relative thickness distribution vs. Normalised radial position

Figure 4.9 Representative distributions of the DTU 10MW in PropArt

The DTU 10 MW was designed with the premise of making it lightweight yet strong, and for that, aerofoils with increased relative thickness were selected, which effectively raise the moment of inertia and therefore the stiffness. These aerofoils belong to the FFA-W3 series, with relative thickness ranging from 21.1% to 36%. For this case, three were selected 24.1% from the tip to 57.54 m, 30.1% until 43.44 m and 36% until 30.19 m. Then, from there on, two further extrapolations were made in order to fit with the cylinder at the blade root, creating aerofoils with relative thickness of 48% until 21.35 m and 60% until 15.55 m radial position. In addition to the base aerofoils, Gurney flaps were added on the inboard side of the blade, from 0.05 to 0.4 in relative radial position [32].

However, with the optimisation of the computational requirements in mind, the Gurney flaps were not considered in the baseline design created in PropArt, given that the analyses with RFOIL alone did not converge and the polar output resulted empty. The comparison between the original shape of the aerofoils and the ones derived in PropArt is shown in Figure 4.10 and Figure 4.11.

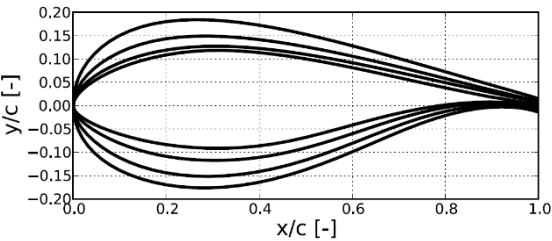


Figure 4.10 FFA-W3 aerofoils with Gurney flaps [32]

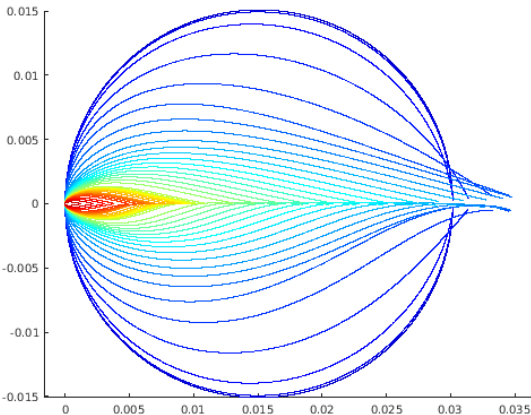


Figure 4.11 Implemented FFA-W3 aerofoils in PropArt

Furthermore, the blade design developed by DTU has a slim shape as seen in Figure 4.12, which was inherited from the NREL 5MW. This is because the first approach to the design was an up-scaling exercise [31], while the second included a thorough study on the aerodynamics [32].

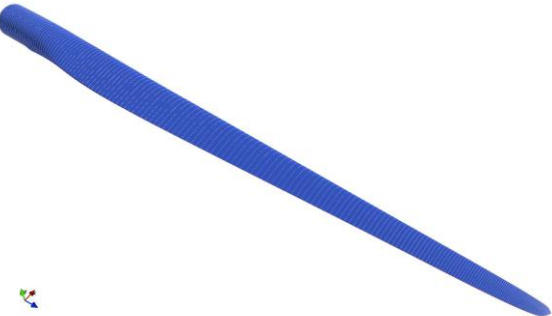


Figure 4.12 DTU 10MW 3-D blade design [32]

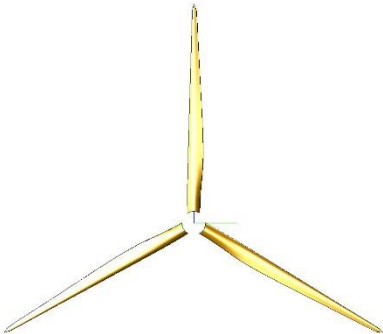


Figure 4.13 DTU 10MW rotor blades representation using PropArt

With this implementation and based on a visual estimation, it can be stated that PropArt is capable of reproducing the blade geometry based on splines, thereby is suitable for integration with the afore-described tools.

### 4.3.5 Integrated Design Tool

With the aim of generating sufficient number of geometries that are further evaluated in their performance, it is essential to integrate the aforementioned tools in order to run them in batch mode. For this purpose, an integrated tool has been developed, which follows the steps from the design loop from Figure 4.1.

First, the baseline (DTU 10MW at full-scale) geometry is loaded in order to be disaggregated into the aerofoils corresponding to the radial positions selected from the initial discretisation. Second, an 'actions' file is created with the corresponding inputs for RFOIL to process each of these aerofoils. Furthermore, the output file from RFOIL is read, and the polars are extracted in order to be entered into the extrapolation and dynamic stall features of AirfoilPrep. With this information, the corresponding aerofoil files are created as an input for FAST, particularly for AeroDyn, which then with the aid of InflowWind and ElastoDyn subroutines calculates the aerodynamic power and thrust for a particular wind speed. Moreover, the output file is read, and the steady state values for the current wind speed are extracted. These tasks are performed for all wind speeds subjected to analysis, which are a few within the range of operation of the turbine.

Consequently, the power and thrust coefficients are derived from the outputs from AeroDyn by the integrated tool in a Matlab function, and further compared against the RFOIL-FAST reference values from Figure 4.6 (for the same wind speeds analysed). Finally, with the computed objective functions of the optimization model in memory, the NSGA-II creates new improved distributions of the constrained variables, i.e. chord, twist and relative thickness. These are further transformed into splines that make a new geometry. This loop is then run for the number of generations set for the simulation.

#### *Validation of the Integrated Design Tool*

As indicated before, it is important to gain trust in the developed tool, and for this reason, a validation exercise is necessary. In this sense, the DTU 10MW, i.e. its coarse representation in PropArt is entered as baseline with the goal of establishing the best geometry that matches the reference aerodynamic performance. For validation purposes, the following tool-specific inputs listed in Table 4.4 are considered. As evidenced here, the Reynolds number is calculated for each radial position, averaged over the wind speeds of analysis. This renders in the spanwise distribution depicted in Figure 4.14, only shown for cut-in, rated and cut-out wind speeds as an example. As indicated in the section 'Validation of FAST', the Reynolds numbers achieved are higher when compared with the figures used by DTU for design purposes.

Furthermore, it is important to set the boundaries to the variables, as described by the optimisation model in section 4.1. Therefore, the upper and lower limits for the parametrisation of the chord and twist distributions are listed in Table 4.5. For this case, no iteration over the thickness was done since the goal is to keep the aerofoil distribution constant.

*Table 4.4 Design integrated tool validation parameters*

<b>Tool</b>	<b>Parameter</b>	<b>Assumption</b>
PropArt	Discretisation	12 nodes
Coupled	Individuals x Generations	33 x 100 (further detailed in section 5.2.3)
	Scale	1:1
	Constrained Variables	Chord and Twist
RFOIL	Range of A.o.A.	-10; 2; 20 (see section 5.2.3)
	Rotational effects	Active
	Reynolds Number	Averaged Calculation
FAST	Controller	Active pitch
	Wind Speeds	6, 10, 11.4, 12, 16, 20, 24

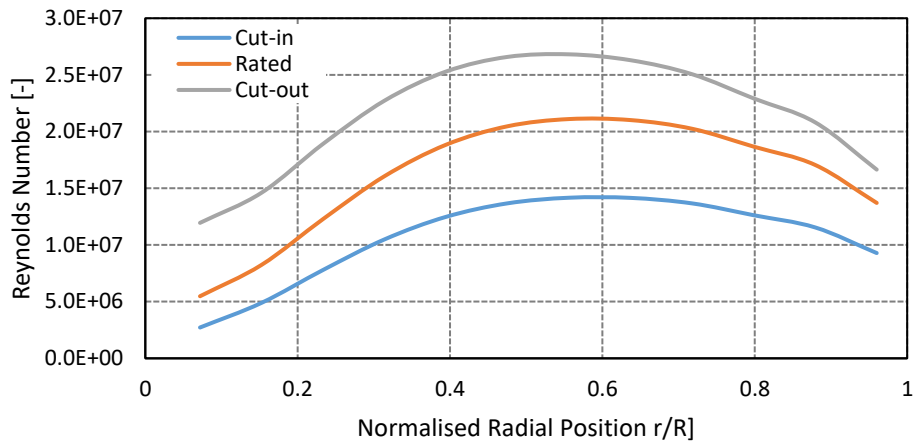


Figure 4.14 DTU Full-scale Reynolds regime

Table 4.5 Chord and twist parametrisation ranges

Variable	Parameter	Range (min, max)		Unit
Chord	Chord at the root	0.06	0.70	c/R [m/m]
	Chord at Mid-span	0.03	0.05	c/R [m/m]
	Angle of descent section	3.00	4.00	[deg]
Twist	Twist at the root	13.18	16.04	[deg]
	x-coordinate mid-span	0.20	0.90	x/R [m/m]
	y-coordinate mid-span	-2.29	14.32	[deg]
	Twist at the tip	-4.01	-2.86	[deg]

Once the simulations were run, a rotor blade geometry was obtained, which is further plotted against the baseline in terms of shape and aerodynamic performance, i.e. power and thrust. First, Figure 4.15 displays the optimisation progression, i.e. the solutions and their position on the Pareto-optimal solution front for both minimisation of the difference in power and thrust coefficients. From these solutions, the one circled is chosen provided that it shows a reasonable agreement on the thrust and secondly on the power.

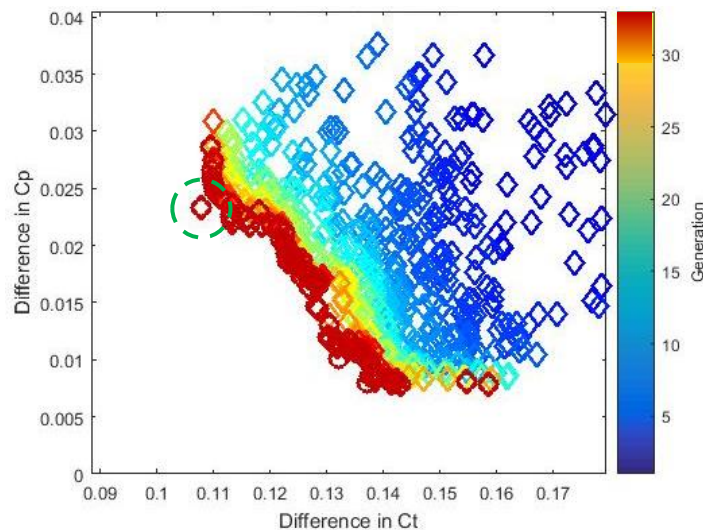
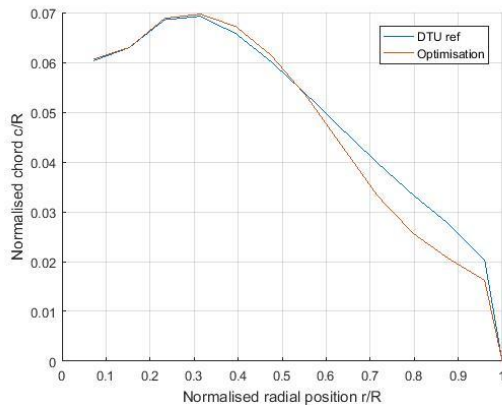


Figure 4.15 Optimisation progression of the DTU 10MW at full-scale

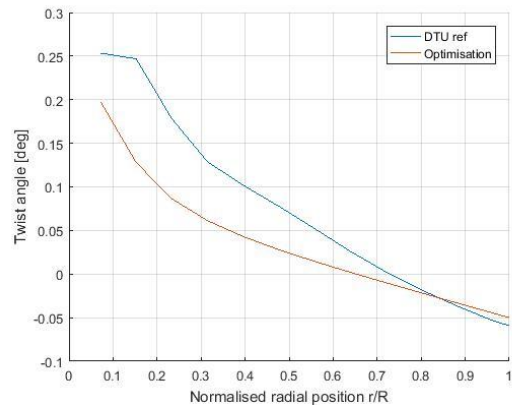
With the selected design, the chord, twist and relative thickness distributions are plotted, in addition to a 3-D representation of the rotor blades, as illustrated in Figure 4.16. From these, it can be evidenced the resemblance in shape of the distributions. For instance, the normalized

chord is virtually the same until mid-span with respect to the baseline, from there, the slope diverges significantly due to the freedom given in the angle of the descent section. It is important to note that the chord must close in a null value, which the optimised geometry does.

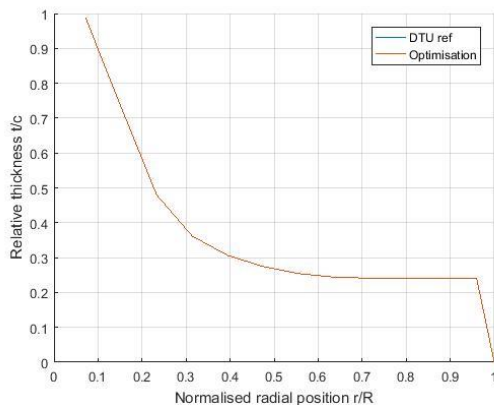
On the other side, the twist distribution shows that at the inboard side there is a lower offset. However, the curve finds its way to similar values like the baseline does at the outer sections of the blade. Moreover, the relative thickness for the baseline and the optimized geometry is the same since no iteration over this variable was performed.



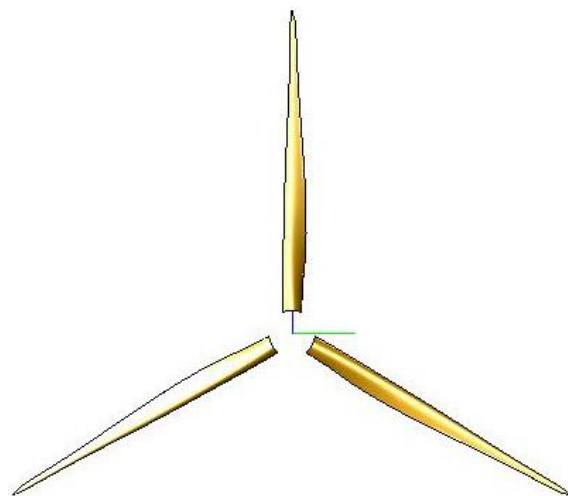
a. Chord



b. Twist



c. Relative Thickness

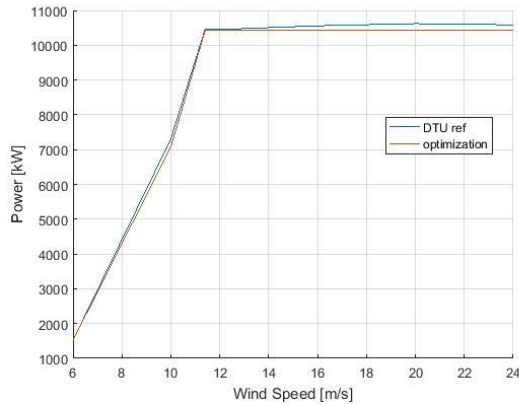


d. 3-D Rotor Blades

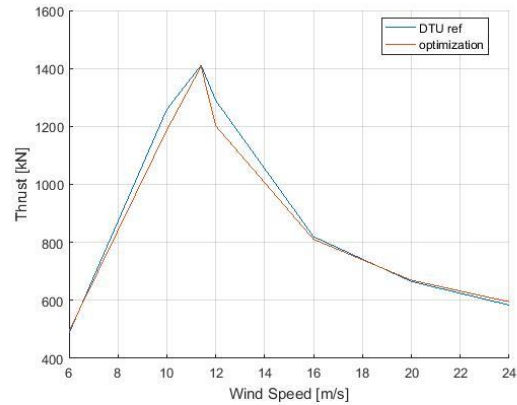
Figure 4.16 Optimised Blade Geometry based on the DTU 10MW using the Integrated design tool

Furthermore, the aerodynamic performance is now compared in order to establish how good the selected solution is with respect to its goals. Figure 4.17 presents the power and thrust curves for both the baseline and the optimised geometry. Here it is evident a good agreement in the power and the thrust at the selected wind speeds. However, the achieved geometry is different in shape with respect to the baseline, which was expected. Therefore, this means that numerous options are available for the design of a wind turbine rotor blade that meet a particular aerodynamic performance.

In this sense, it can be stated that the integrated design tool is validated, since it accomplishes its goal related to achieve certain performance values. Now it can be employed in the design of the scaled-down rotor blade for testing of a floating platform in a wind/wave basin.



a. Aerodynamic Power vs. Wind Speed



b. Thrust vs. Wind Speed

Figure 4.17 DTU 10MW rotor blades representation using PropArt

## 4.4 Tools for Design Check

Now, regarding the right side of the design flowchart that corresponds to the validation step, a set of tools are necessary in order to establish how reproducible the results are for the selected design, i.e. the aerodynamic performance. This is of great importance because there has to be certain trust in the design before moving forward with the construction and further testing phases. For this purpose, in contrast to BEMT, CFD 3-D is to be employed, specifically ReFresco 3-D and complementary commercial software packages for pre- and post-processing of the geometry and the results respectively. In this section, these are briefly introduced.

### 4.4.1 Rhinoceros

Rhinoceros© (commonly known as Rhino) is a commercial 3-D modelling tool developed by Robert McNeel & Associates, capable of handling Non-Uniform Rational B-Splines (NURBS)-based curves, surfaces, point clouds and solids in order to create geometries of any complexity [65, 66]. To import, and pre-process the geometry that comes from Matlab, Rhino is complemented with two additional sets of plugins, MARIN's and Grasshopper©. The first comprises among others, a propeller functionality capable of importing the propeller (in this case the wind turbine rotor blade) in spline-format coming from the integrated design tool. Additionally, it is able to integrate the aforementioned geometry with Grasshopper in order to refine and smoothen for meshing purposes. Grasshopper, on the other hand [67], is a user-friendly interface that enables to automate every function on Rhinoceros, through block-interactive algorithms.

Considering this latter plugin, a structured set of instructions have been implemented in a workflow format, in order to define sequence of activities, described as follows: First, the geometry resulting from the optimisation is imported. Then, it is further disaggregated into curves and surfaces, such as leading and trailing edges, tip, and suction and pressure side. Moreover, the non-dimensional blade is scaled-up (with  $\lambda$ ), then the naked edges are smoothened and the trailing edge is adjusted to comply with the minimum thickness constraint of 1.0 mm to achieve manufacturability, as will be further discussed in section 5.1. Furthermore, the blade is rotated around its pitch axis to the selected pitch angle and is replicated every  $120^\circ$  to achieve a 3-bladed rotor, whose blades are then mounted onto the hub so a solid can be realised. In addition, the cylindrical domain, further detailed in section 5.3, through which the air will flow undisturbed is constructed. Finally, all surfaces are meshed with triangular shapes, in order to be exported as a '.stl' file for HEXPRESS to read.

#### 4.4.2 HEXPRESS

The second stage of the preprocessing (before actually simulating the rotor with the CFD code) is to generate the mesh, i.e. divide both the body and the domain into fine elements to the end of improving calculations. For this task, HEXPRESS™ is selected. HEXPRESS is a full-hexahedral unstructured mesh generator, developed by NUMECA International, which allows to process geometries of any level of complexity. Additionally, among many functionalities, comprises the capability of smoothing surfaces to obtain high-quality boundary layers [68]. Furthermore, it is compatible with Python-based scripts to automate its operation, one of which was developed by MARIN and was available for further implementation in this work.

Considering the meshing itself, the finer the elements are, the better the resolution of the results will be and the larger the computational requirements. For this purpose, a grid refinement study is usually performed in order to determine the relative error for a specific variable between two adjacent time-steps based on the number of cells. From this, it can be determined the appropriate cell size according to the admissible error, bearing in mind a minimisation of the simulation time.

#### 4.4.3 ReFRESHCO 3-D

Once the pre-processing is complete, the tool that takes over the CFD 3-D calculations is ReFRESHCO - an acronym for Reliable & Fast RANS Equations solver for Ships and Constructions Offshore -, a code developed by MARIN for maritime applications. It is capable of solving multi-phase unsteady incompressible viscous flow by means of the Reynolds-averaged Navier Stokes (RANS) equations. These are discretised by the finite-volume method, which uses cell-centred variables. In addition, it features the ability to handle moving, deformable and sliding grids, and adapt them for the computation purposes, i.e. refining or coarsening them [42, 69, 70]. Moreover, ReFRESHCO has been verified and validated with the NREL 5MW and the MSWT as presented in Figure 4.18 and Figure 4.19.

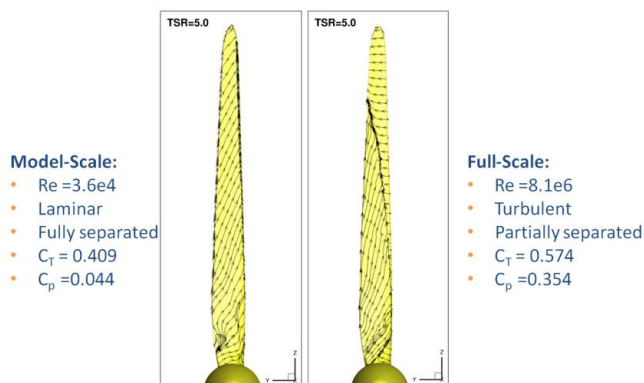


Figure 4.18 Visualisation of flow around MSWT and NREL 5MW rotor blades simulated with ReFRESHCO [42, 70]

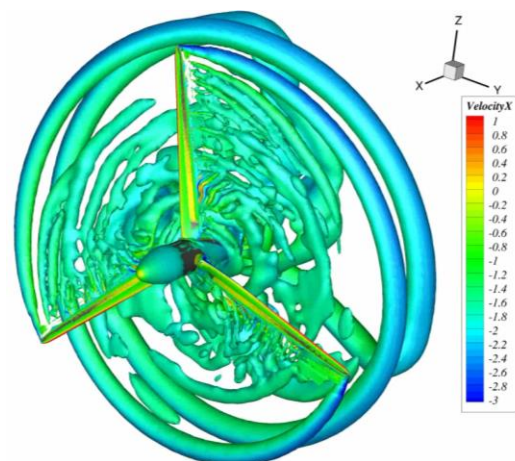


Figure 4.19 Visualisation of wake developed behind the NREL 5MW rotor simulated with ReFRESHCO [42, 70]

In detail, ReFRESHCO allows the user to vary the simulation parameters through a 'control' file. For this particular application, these parameters are: the number of time-steps; inflow conditions, i.e. wind speed; air properties; rotational speed; and the boundary layer conditions, i.e. the dimensionless wall distance criterion. This latter gives an indication of the grid refinement of the boundary layer element adjacent to the surface, and it is described by equation (4.4). Here  $u_*$  is the friction velocity near the wall,  $y$  is the distance to the closest wall, and  $\nu$  is the kinematic viscosity defined as the ratio of the dynamic viscosity  $\mu$  and the density

of the fluid  $\rho$  [71]. It is desired that  $y^+$  takes a value, at every point along the assembly surface, lower than 1 in order to achieve good resolution in the behaviour of the boundary layer.

$$y^+ = \frac{u_* \cdot y}{\nu} \quad (4.4)$$

The outcomes from ReFRESKO are the total forces acting upon the rotor and the total moment. The first (in the axial direction) can be interpreted directly as the thrust, while the latter when multiplied with the rotational speed yields in the power.

#### 4.4.4 Tecplot & Paraview

With respect to the post-processing of the results and provided that the outputs from ReFRESKO have a large data set format, it is useful to visualise the behaviour at which the simulation arrives upon convergence. Therefore, Tecplot and Paraview are employed for these purposes. Tecplot is a commercial software, while Paraview is an open-source platform developed by Kitware, for visualisation of results contained in extensive data sets, in order allow the user to analyse them qualitatively and quantitatively [72, 73]. The first will be employed for the full-scale case, while Paraview for the model-scale, given its availability at the promoter of this project and at the university respectively. The results only vary in terms of colours and resolutions.

#### 4.4.5 Validation of the Tools for Design Check

Analogue to the procedure followed for the design tools, it is important to make evident how accurate the results are yielded from the use of the afore-described tools, which are proven to be suitable for validating the BEMT-based design.

##### *Rhinoceros*

For this purpose, the DTU 10MW blade geometry created in PropArt was imported into Rhino with the aid of the plugin especially developed by MARIN, i.e. the propeller importer. Furthermore, it is refined, rotated, replicated and mounted onto the hub, with the Grasshopper-based propeller geometry add-on, also developed by MARIN. Figure 4.20 displays 3-D model of the full-scale RNA created in Rhino. Moreover, the cylindrical domain surface is created, and all the external surfaces are meshed.

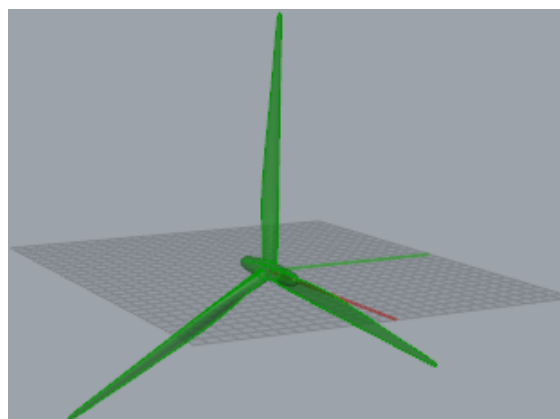


Figure 4.20 DTU 10MW RNA model on Rhinoceros

##### *Hexpress*

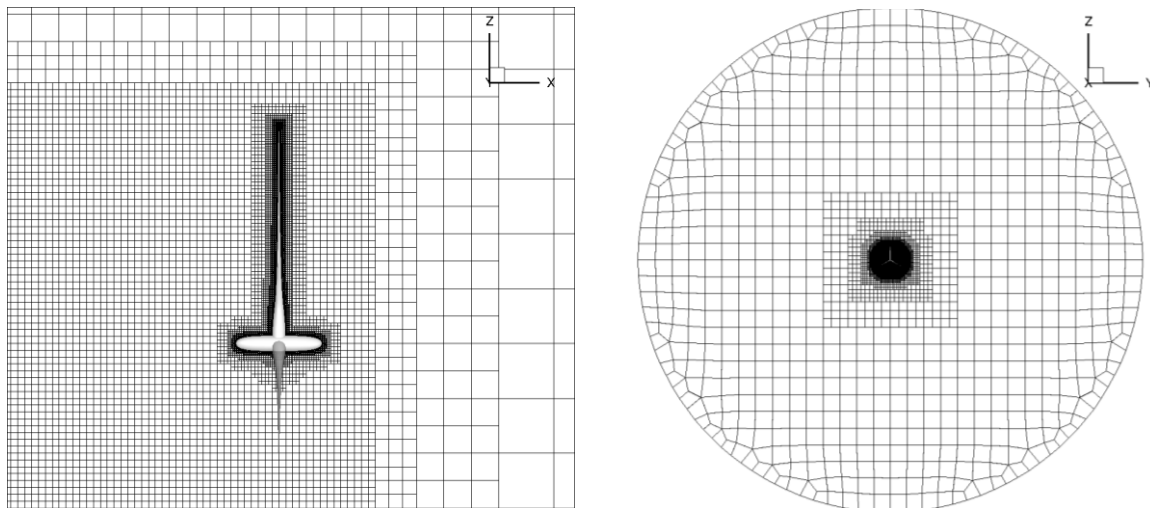
With the domain and the body meshed at their surfaces, the full volumetric mesh is done by HEXPRESS. For this purpose, the initial meshing was set to 10 cells in every direction, thus

giving 1,000. These were globally refined 20 times and at every location. Furthermore, a detailed refinement was set according to the parameters stated in Table 4.6.

Table 4.6 Meshing Refinement Parameters

Location		Levels of Refinement
Trailing Edge	Tip-most	14
	Middle	11
	Root	9
Leading Edge	Tip-most	11
	Root	9
Tip		13
Suction Side		8
Pressure Side		8
Hub		8

This gave approximately 20 million cells, which according to a previous study done by Make at MARIN, could render in a 2% in error [70], considered as acceptable. This deduction will be further illustrated in section 5.3.3. Figure 4.21 shows the viscous layer and the domain meshed with HEXPRESS. Nevertheless, detailed figures are shown in Appendix A.



a. Meshing of Viscous Layers

b. Meshing of Cylindrical Domain

Figure 4.21 DTU 10MW RNA and Cylindrical Domain meshed with HEXPRESS

### ReFRESKO

In contrast to the integrated design tool, there is no glue code that couples and allows to control all the validation tools. Therefore, in order to make the validation process faster, and considering that meshing and the CFD calculations for every geometry (or variation thereof) is to some extent time-consuming, only three cases are analysed. For this reason, the simulations are run varying the TSR and keeping a zero-pitch condition. In principle, when focusing on the TSR instead of the pitch, the vector triangle shown for the aerofoil analysis in the BEMT description keeps its proportion, maintaining the inflow angle derived from its tangent. However, this assumption leaves out the incorporation of the axial and tangential induction factors, reminded from equation (2.21) displayed below, which renders in a computed discrepancy of 5 – 10% in the effective inflow angle. Therefore, for simplification purposes this effect is neglected, although strictly speaking the CFD calculations should be done varying the

pitch as well, but it represents making a different 3-D model and corresponding mesh for every case.

$$\tan \varphi = \frac{U(1 - a)}{\Omega r(1 + a')} = \frac{1 - a}{(1 + a') \cdot TSR_r}$$

In this sense, the TSRs subjected to analysis at full scale are 8.0, 7.5 and 5.5, corresponding to wind speeds 7, 11.4 and 16 m/s. For every case, the rotational speed according to the pitch control strategy depicted in section 5.2.3 is respected. Table 4.7 displays the corresponding input parameters for every simulation.

Table 4.7 Inflow and RNA operational parameters for full-scale CFD calculations

Case No.	TSR [-]	Full-scale Wind Speed [m/s]	Full-Scale Rotational Speed [rad/s]	Reference Velocity at 0.7R [m/s]	Reference Length at 0.7R [m]
1	5.50	16.0	0.987	63.644	4.392
2	7.50	11.4	0.959	60.926	4.392
3	8.00	7.0	0.628	39.820	4.392

## Results

Finally, the outcomes from these simulations are post-processed, which means that both the power and the thrust coefficients are computed from the total axial force and moment acting upon the RNA. Nevertheless, before showing the comparative results, it is appropriate to examine the quality of the outcomes, and for that reason the dimensionless wall distance ( $y^+$ ) is plotted and presented in Figure 4.22, which shows steady state values lower than 1, as established before.

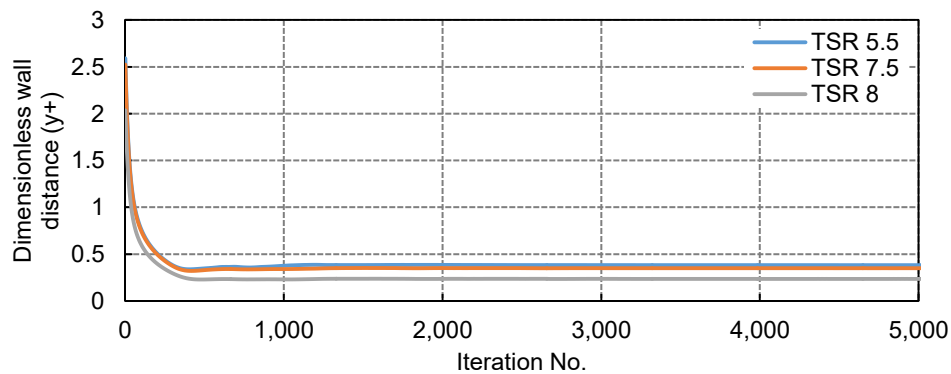


Figure 4.22 Dimensionless Wall Distance for Full-scale CFD Simulations

Furthermore, it is important to take a close look at the flow around the RNA, for which the visualisation for TSR = 7.5 is shown in Figure 4.23. Here, it is evident a drop in the wind speed after the rotor (yellow, orange and red areas), which is due to the kinetic energy being extracted by the rotating wake. In addition, for further detail Appendix A displays the visualisation of the airflow passing through the blade at every station, including the suction and pressure sides views. From those figures, it can be inferred that the flow is mostly attached to the surface spanwise, showing minor recirculation and vortices derived from 3-D flow effects. This can be explained by the fact that the high Reynolds regime delays the transition from laminar to turbulent, i.e. close to the trailing edge.

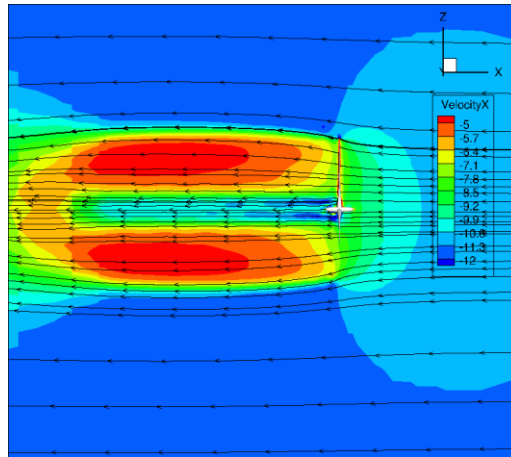


Figure 4.23 Visualisation of flow around DTU 10MW for TSR 7.5 with Tecplot

Now, in order to compare the results of the aerodynamic performance, a new set of BEMT calculations for the DTU 10MW was performed without considering a controller for the aforementioned reasons, but setting the pitch to zero and imposing the RPM. Therefore, varying strictly the TSR as done in the CFD calculations. Figure 4.24 below displays this comparison.

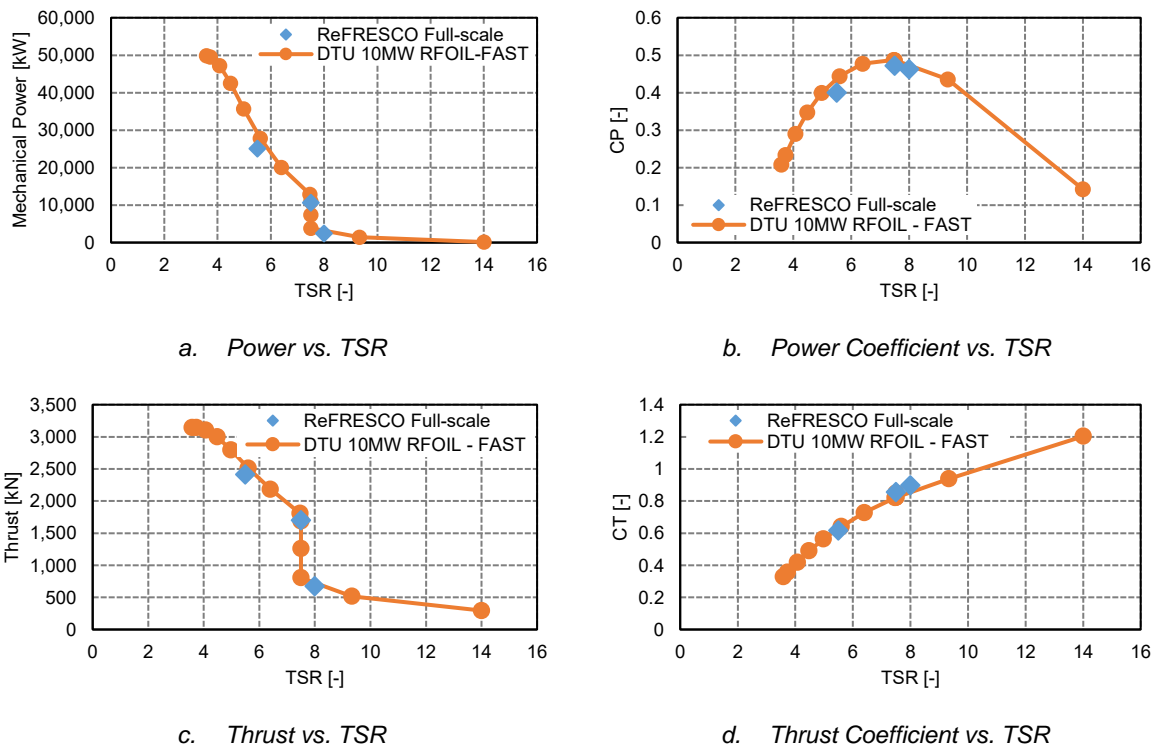


Figure 4.24 Validation of ReFRESKO vs. BEMT for the DTU 10MW

It can be noted from this figure that there is a good agreement between both approaches for the TSRs subjected to evaluation. This means that in spite the zero-pitch condition, ReFRESKO was able to predict the behaviour for the same operating conditions as in BEMT. For this reason, the set of tools for design check is trusted for its further implementation in the model-scale blade design.

# 5 Model-scale Rotor Blade Development

In this chapter, the inputs and considerations to be taken into account in the design process of the model-scale rotor blade are presented. The tools described and validated in the previous chapter are to be employed using carefully defined constraints and parameters. To this end, the design constraints are introduced in section 5.1, and the parameters are specified for each of the design tools in section 5.2. Finally, the parameters concerning the validation tools are detailed in section 5.3.

## 5.1 Design Constraints

Defining the boundaries is crucial in the design process since they help narrowing down the potential options to be assessed, thus speeding up the selection process when looking for the specimen that behaves best. In this section, the global design constraint, concentrated on dimensioning is introduced. This refers to the manufacturing constraint.

Similar to the full-scale blades, these are manufactured using two moulds, one for each half. These moulds are custom-milled for every blade design. Hence, there is no constraint regarding geometry unless an end plate is implemented [12, 47]. Following that, two layers of carbon fibre and the resin are put together in order to be cured with the application of vacuum at 0.9 mbar. Then, both halves are glued together, and the excess of material (flash) is removed. The only strict manufacturing constraint is that the trailing edge thickness (or the thinnest area throughout the entire blade span) must be larger than 1.0 mm so that there is no place for separation of composite surfaces during handling and testing. This is because the limiting factor is the thickness of the carbon fibre layer itself. Finally, the blade is carefully sanded in order to smoothen the surface.

In order to comply with this requirement, when presenting the final 3-D model to Rhino, the same procedure is followed as the pre-processing for CFD calculation. The geometry's edges are smoothed with the aid of the Grasshopper-based script, and a precise cut is made along the trailing edge to guarantee that none of its sections has thickness under 1.0 mm.

## 5.2 Design Inputs and Assumptions

In this section, the design inputs and their corresponding assumptions, i.e. the ones to be entered into the integrated design tool are presented in the following categories: geometry, environmental conditions, and simulation parameters. In the first, the blade discretisation, baseline aerofoils and boundaries of distributions are described. Secondly, the scaling factor and the wind profile are established. Finally, additional specific parameters for RFOIL, AirfoilPrep, FAST and PropArt are prepared.

### 5.2.1 Geometry

#### *Blade discretisation*

In order to properly select the blade discretisation that optimises the performance of the integrated design tool and in particular of FAST without degrading the solution, a sensitivity analysis was performed, whose results are presented in the table in Appendix B. From that table, where varying from 37 nodes (original blade discretisation of the DTU for FAST [60]), 17 and 12, it is evident that there is a significant decrease in simulation time for the coarser while the remaining simulation parameters were kept unaffected. In addition, the change in performance evaluated is negligible. Therefore, 12 nodes is the most appropriate discretisation

and as noticed in section 4.3.4, the chord, twist and relative thickness distributions are virtually the same as the finer case.

### Aerofoil distribution

Similar to previous exercises, the most suitable choice for low Reynolds numbers are the aerofoils with lower thickness. This is because they have less flow detachment than thicker aerofoils at the boundary layer, which effectively means an improved design lift when subjected to transition from laminar to turbulent flow. This is relevant because this is the range of operation where the laminar separation bubbles, introduced in section 2.2.2, occur. For this purpose, extensive research has been done with regard to the design of aerofoils that cope with such low-speed conditions.

In this sense, special aerofoils for all types of applications have been documented, and in particular, a reduced group suitable for small HAWT (low wind speeds with respect to large-scale) have been developed [21, 48]. This collection includes the overly used S822 and S823, prepared by NREL three decades ago [46, 74, 75]. More recently, Selig and Giguere developed a family of aerofoils (SG604x), illustrated by Figure 5.1, especially suitable for their implementation on small wind turbines of variable speed, due to its high lift-to-drag ratio at low Reynolds numbers [76]. The SG6040 is the thickest of them all with a relative thickness, designed for structural reasons to be part of the inboard side of the blade (30% radial position) due to its ability to handle large bending moments and to achieve significant blade-stiffness demands. On the other hand, SG6041, SG6042 and SG6043, designed to achieve high aerodynamic performance [48] have the same relative thickness with increasing camber and design lift coefficient as displayed in Table 5.1. As indicated by Manwell et al, a cambered aerofoil can often increase the lift and decrease the drag at low angles of attack [18].

Table 5.1 Properties of the SG604x aerofoils series for small wind turbines [76]

Aerofoil	t/c [%]	Camber [%]	Design Cl [-]	Design Re [-]
SG6040	16	2.5	1.1	200,000
SG6041	10	2	0.6	500,000
SG6042	10	3.8	0.9	333,333
SG6043	10	5.5	1.2	250,000

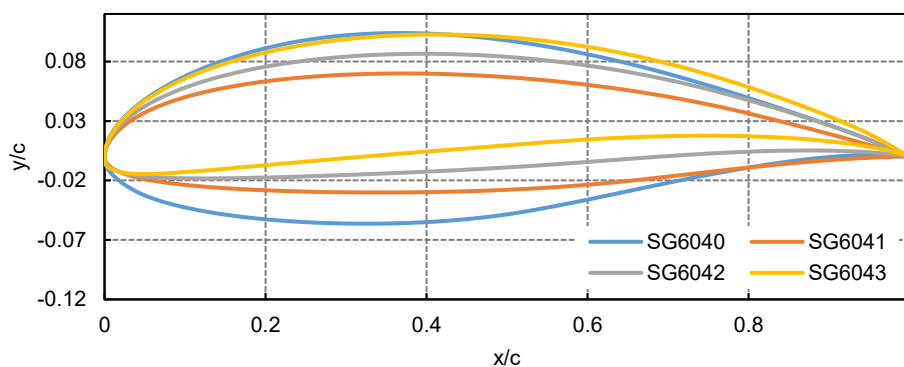
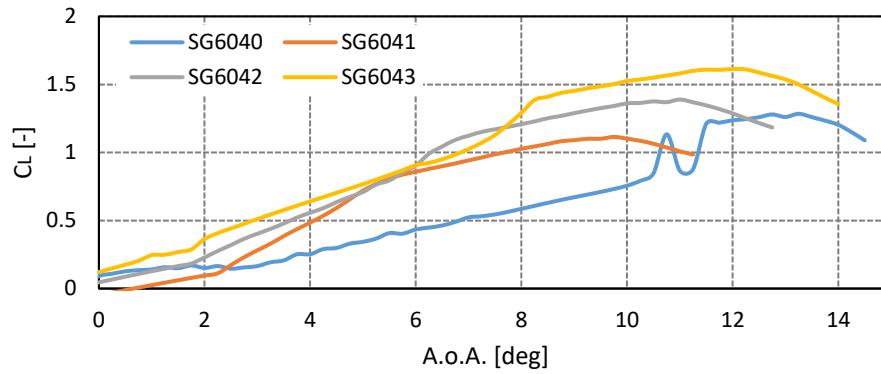
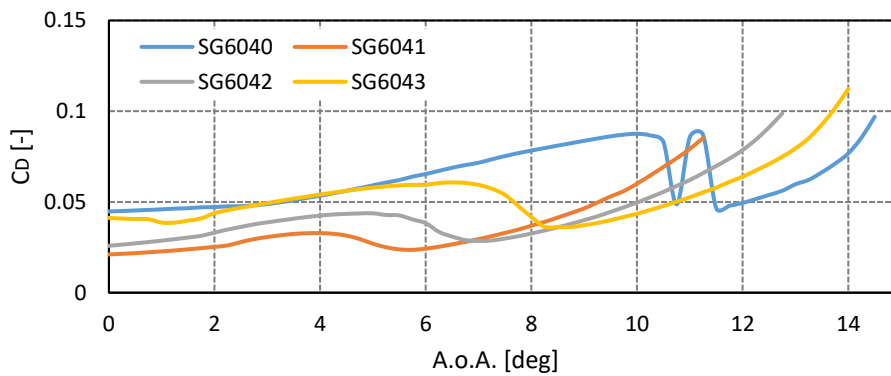


Figure 5.1 SG604x aerofoil series for HAWT application [77]

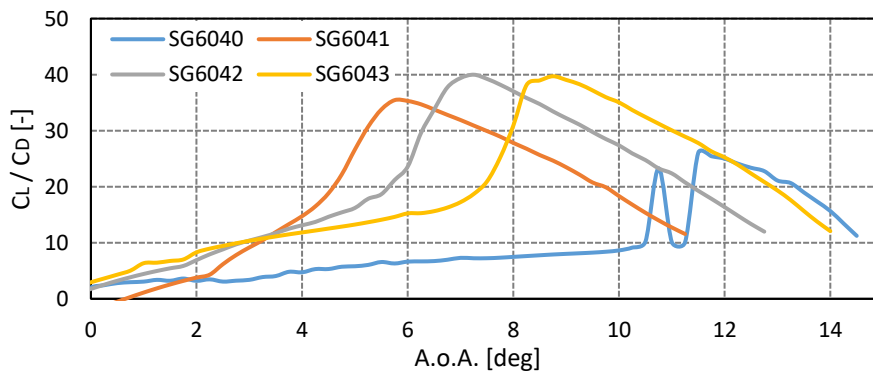
In order to establish their suitability for further implementation in the current rotor blade design, it is important to look at the aerodynamic coefficients, i.e. lift and drag for a low-Reynolds regime ( $=50,000$ ). To this end, Figure 5.2 displays the polars for the aforementioned aerofoils obtained in [77] with the aid of XFOIL.



a. Lift coefficient



b. Drag coefficient



c. Lift to Drag coefficient ratio

Figure 5.2 Polars SG604x aerofoil series at  $Re = 50,000$

Clearly, from the polars shown above, it can be inferred that the SG6040 aerofoil has a unique aerodynamic performance, different in trend to the rest. This is due to its higher relative thickness, which as seen before behaves poorly under low-Reynolds conditions (lowest and inconsistent lift-to-drag ratio), as a consequence of premature flow separation.

However, when examining the subsequent aerofoils, it can be noted that the maximum lift progressively increases towards the tip while the drag decreases. This yields in a lift-to-drag ratio larger than 35 for all three remaining aerofoils, which is already a high performance for low-Reynolds aerofoils. For to these reasons, this series is selected to take part in the current rotor blade design. In detail, they will be placed respectively where the 48%, 36%, 30.1% and 24.1% aerofoils from the full-scale design were initially placed. In other words, the blade root

cylinder is extended up to the space formerly occupied by the thicker aerofoil (~20% of the radius), as presented in Table 5.2. This latter is a setting for the integrated design tool, indicating the starting point for chord and twist optimisation.

Table 5.2 Aerofoil distributions for full- and model-scale

Blade Station	Aerofoil Full-scale	Aerofoil Model-scale
10.23%	Cylinder	Cylinder
17.44%	FFA-W3-600	Cylinder
23.94%	FFA-W3-480	SG6040
33.86%	FFA-W3-360	SG6041
48.71%	FFA-W3-301	SG6042
64.53%	FFA-W3-241	SG6043

This selection of aerofoils renders in a thinner blade compared to the baseline DTU 10MW at the same scale. This can be evidenced in Figure 5.3, where the relative thickness (non-dimensional) is plotted for both turbines.

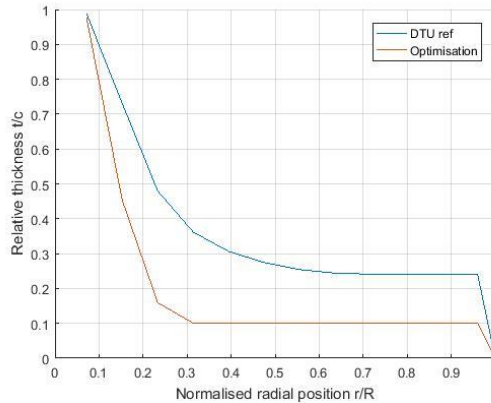


Figure 5.3 Relative thickness distribution for DTU 10MW and model-scale current design

### Blade Chord, Twist and Relative Thickness parametrisation

As introduced before, the aim of the optimisation model is to achieve the goals of minimising the thrust and power differences with respect to the reference performance of the DTU 10MW, by varying the chord and twist distributions. Therefore, a parametrisation of these distributions is necessary and for that purpose, a set of boundaries are proposed, which are displayed in Table 5.3.

In addition to chord and twist distributions, the relative thickness is further incorporated, with the aim of establishing the capabilities of the optimisation module of the integrated design tool. It can be seen from the following parametrisation that more freedom was given to the variables in comparison to the full-scale validation exercise performed in section 4.4.5. This is because there are no major constraints with respect to manufacturing for the chord and twist.

Table 5.3 Blade Chord and twist parametrisation for model-scale

Variable	Parameter	Range (min, max)		Unit
Chord	Chord at the root	0.04	0.14	c/R [m/m]
	Mid-chord	0.04	0.07	c/R [m/m]
	Angle of descent section	2.00	5.00	[deg]

Variable	Parameter	Range (min, max)		Unit
Twist	Twist at the root	0.00	28.65	[deg]
	x-coordinate mid-twist	0.20	0.90	x/R [m/m]
	y-coordinate mid-twist	-2.86	28.65	[deg]
	Twist at the tip	-11.46	5.73	[deg]
Thickness	x-coordinate mid-thickness	0.05	0.30	x/R [m/m]
	y-coordinate mid-thickness	0.01	0.20	t/c [m/m]
	mid-thickness weight	1.00	2.00	[-]
	Thickness at the tip	0.01	0.15	t/c [m/m]

## 5.2.2 Environmental Conditions

### *Scaling Factor*

As seen from section 2.1, defining the proper scaling factor and more importantly the scaling methodology is crucial for this design, given that the operating environment of a FOWT involves loading sources of various kinds, e.g. wind, waves and sea currents. For this reason, there is no doubt that clearly, the most appropriate and consistent approach is the Froude-based, which entails then a low-Reynolds number regime. Several studies suggest that the geometry is completely different. Proof of this is the ample implementation of the Froude-scaling in previous design exercises done for several testing campaigns of FOWTs as illustrated in section 3.1.

The definition of a proper scaling factor depends mainly on the properties of the testing facilities in terms of space and quality of the environmental conditions being replicated, i.e. the capabilities and fidelity of the wind and wave generators. One of the main goals of this work is to set up a procedure for designing rotor blades for their further construction and implementation for testing FOWT platforms in MARIN's Offshore Basin. For that reason, the constraints that this setting entails will determine the scaling factor. For this purpose, Figure 5.4 presented below shows the area of the NREL 5MW rotor that is influenced by the wind inflow coming out of the elliptical nozzle of the wind generation system of the Offshore Basin.

Here it can be evidenced that the scaled-up vertical distance (with  $\lambda = 50$ ) between the lowermost and the uppermost points of the ellipse is 150 m, which means that the rotor of the DTU 10MW (~ 178 m diameter) would not be able to be fit in the area of influence when fully centred. For this reason it is convenient to increase the scale in a factor of  $\sim 180/150 = 1.2$  times the current scale factor used in the design of the MSWT, which as seen before was based on the NREL 5MW. This gives a new  $\lambda$  of 60.

This choice will clearly have an impact on all variables present during the test campaign, and no modification to the wind and wave generators are needed. For instance, every dimension of the entire FOWT, from the rotor blades to the floating platform will decrease in size in a factor of 60 from the full-scale, the frequencies, e.g. rotational speed and wave frequency will increase, and the wind speed will be reduced in a factor of  $\sqrt{\lambda}$  respectively. Fortunately, the increase in wave frequency is covered by the capabilities of the basin since it can generate waves of up to 3.3 Hz [33], when the expected for the North Sea is around 0.2 Hz at full-scale (~1.3 Hz at model-scale).

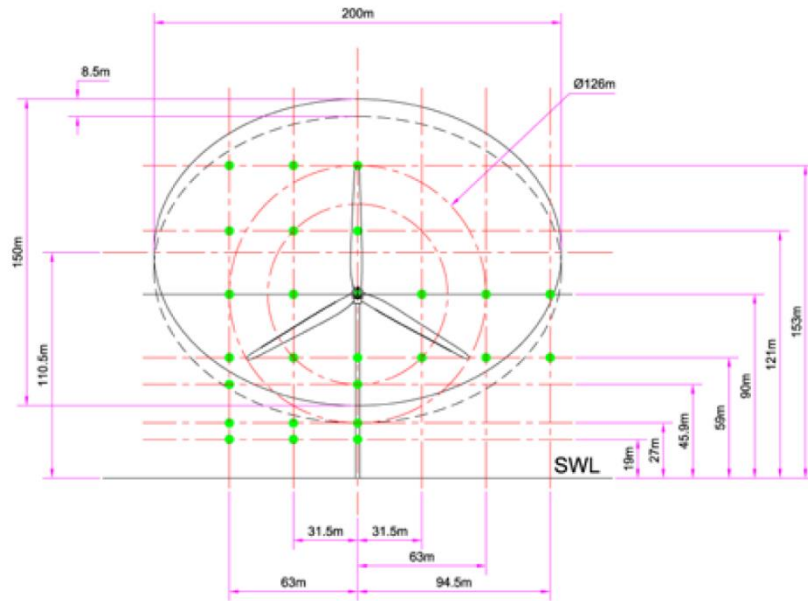
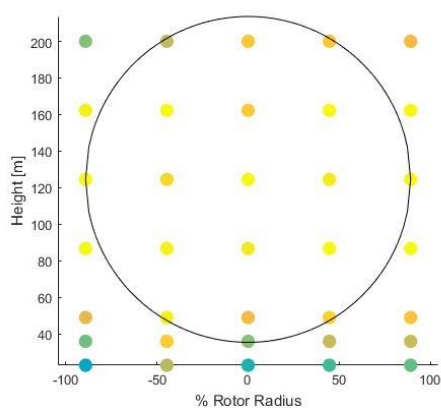


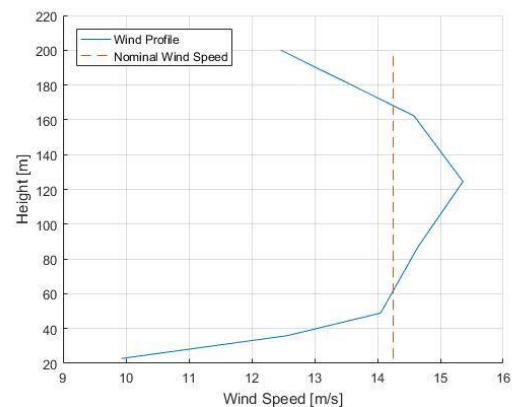
Figure 5.4 Up-scaled elliptical nozzle wind outlet area of influence [39]

### Wind profile

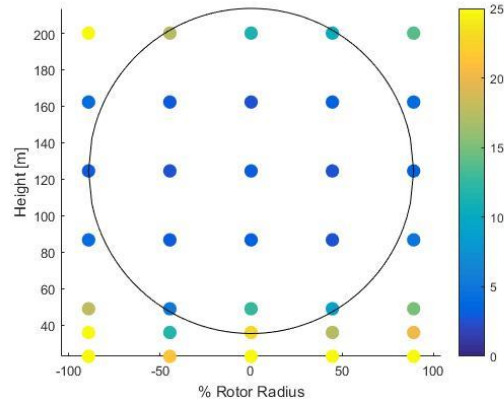
Characterising the wind that represents more accurately the conditions expected during testing is of great value; in this sense, a suitable blade that matches in real-life the predicted performance can be designed. For this purpose, the wind conditions measured at MARIN's offshore basin for a specific nominal wind speed at full-scale of  $14.25 \text{ m/s}$  are to be taken into consideration, which are shown in Figure 5.5. Here, the fraction of the maximum wind speed achieved during the measurement campaign, and the corresponding boundary layer profile within a  $178.3 \text{ m}$  diameter rotor swept area are depicted in (a) and (b) respectively. Furthermore, the turbulence intensity is presented below in (c). This latter has an extensive meaning in terms of flow fluctuation, nonlinearity, vorticity, energy dissipation and diffusivity [78], but in short indicates how large is the standard deviation of the wind speed with respect to the mean value.



a. Fractional wind speed distribution within the rotor swept area



b. Wind profile



c. Turbulence intensity distribution within the rotor swept area

Figure 5.5 Wind profile at MARIN's Offshore Basin

It can be evidenced that in general, the wind speed is relatively uniform, i.e. there is virtually no variation within the rotor swept area. Nevertheless, when taking a close look at the wind profile values, on average the spread is 80% of the nominal wind speed. In addition, from the turbulence intensity spread, it can be seen that in the innermost area is on average below 5%, hence for modelling purposes, it is assumed that the flow is steady. This can be stated because as mentioned before in section 3.2.1, the wind generation is set to be time-independent, i.e. no intermittency in the flow is allowed.

Now, the aforementioned uniform and steady flow conditions are applied to all wind speeds subjected to analysis. This is important because it is desired that the rotor blade performs adequately throughout the entire range of operation, i.e. from cut-in until cut-out points, going through rated wind speed. For this purpose, and bearing the computational cost in mind, seven representative full-scale wind speeds are selected: 6, 10, 11.4 (rated), 12, 16, 20 and 24 m/s.

### 5.2.3 Simulation Parameters

#### RFOIL

In order for RFOIL to compute the aerodynamic coefficients for the set of aerofoils, in which the blade of the current iteration is divided, several inputs need to be entered. These are written by the integrated design tool into an “actions” text file, which is further read by RFOIL, as illustrated in Appendix C. First, the aerofoil geometry data file (.dat) is loaded, which contains the 2-D coordinates ordered such that they start and finish in the same point, leading or trailing edge. Second, the Reynolds number is calculated according to equation (2.1), being  $V$  the magnitude of the relative velocity vector ( $U_{rel}$ ), which responds to equation (2.22), and the characteristic length  $L$  being the chord ( $c$ ) at the radial position at which the aerofoil is located, as introduced in section 3.1.3. This calculation (for a particular thrust-matched model-scale rotor blade) at  $\lambda = 60$  renders in the distribution depicted in Figure 5.6, which agrees with the low-Reynolds number suitable concepts.

Furthermore, the transition from laminar flow to turbulent must be defined. This responds to the  $e^n$  criterion for free transition and tripping for the forced scenario. The first is always active on RFOIL and for that reason the  $N_{crit}$  parameter is to be set. The  $N_{crit}$  is defined as the logarithm of the amplification factor of the most-amplified frequency that initiates the transition, and is selected based on the ambient disturbance level on which the aerofoil operates [79], as seen in Table 5.4. For this case, the average wind tunnel is considered, therefore a value of 9.

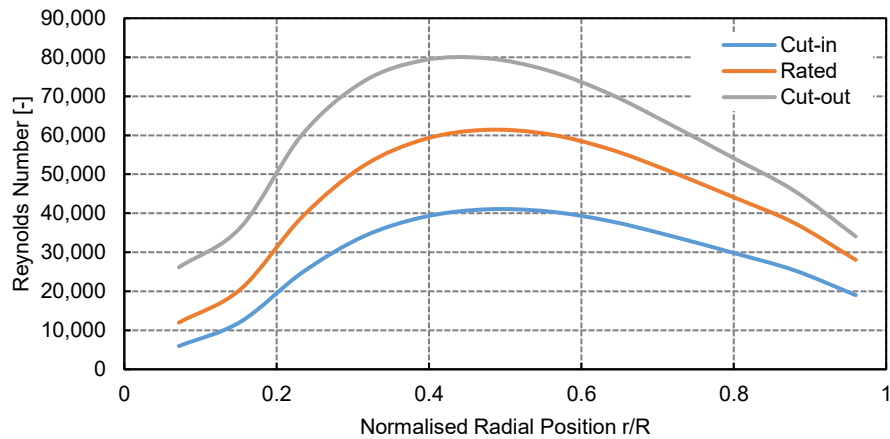


Figure 5.6 Model-scale Reynolds regime

Table 5.4  $N_{crit}$  based on testing ambient condition [79]

Situation	$N_{crit}$
Sailplane	12 – 14
Motorglider	11 – 13
Clean Wind Tunnel	10 – 12
Average Wind Tunnel	9
Dirty Wind Tunnel	4 – 8

Moreover, the rotational effects are to be taken into account and for this purpose, the non-dimensional free stream velocity  $f_0$  and the  $2/3$  of the local solidity  $c/r$  criterion are computed for every station along the blade, which are illustrated in Figure 5.7 for the same low-Reynolds blade geometry. Nevertheless, a sensitivity analysis for the SG6042 at  $Re = 45,000$  displayed in Figure 5.8 proved that RFOIL’s output for low-Reynolds aerofoils remains unaffected when these particulars  $f_0$  are replaced by 1. In addition, unfortunately, when computing the polars for inboard aerofoils at low-Reynolds numbers, i.e. with high local solidity, the solution never converges. That is why for this calculation, all aerofoils are considered with a null local solidity. This is an aspect to be further revised by the developers of RFOIL.

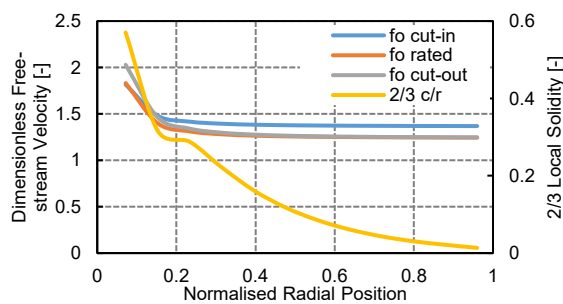


Figure 5.7 Parameters for the incorporation of rotational effects at model-scale

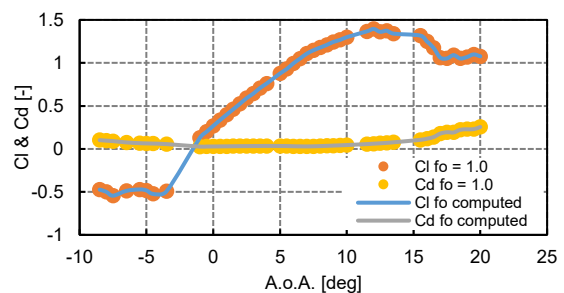


Figure 5.8 Sensitivity Analysis on the dimensionless free-stream velocity for low-Reynolds aerofoils

In light of the need to help RFOIL’s convergence and stability and therefore save CPU time, XFOIL’s developer Mark Drela advises to decrease the “Viscous Solution Acceleration” - VACC parameter to zero for low-Reynolds regimes, which results in “less large-Newton iterations”. Additionally, since there is no incorporation of tripping strips along the aerofoil’s surface, then the forced transition chord station ( $x_{tr,top}$  and  $x_{tr,bottom}$ ) are set to 1, i.e. at the trailing edge [79].

Finally, the range of A.o.A. for the polars was selected to be from  $-10^\circ$  to  $20^\circ$  in increments of  $2^\circ$ , because it was proven to be processed in less than 5s with less risk of incomplete output. However, in order to cope with the incomplete files, due to non-convergence of the solution, a condition of rejection was implemented in the integrated design tool, which only allows polar files with more than 60% of its expected content. This way, if one file was rejected, the entire geometry was discarded.

### *AirfoilPrep*

As mentioned before, AirfoilPrep is quite straightforward when it comes to its inputs. For instance, the extrapolation feature that employs the Viterna-Corrigan approach receives the list of polars previously obtained with RFOIL. Furthermore, the dynamic stall calculator takes the stall angle, which is the first change in slope at a positive A.o.A., i.e. the maximum after the attached-flow region. This will result in a prepared input for every aerofoil to be read by AeroDyn v.14 as displayed in the FAST Aerofoil Input File section of the Appendix D.

### *FAST*

FAST, on the other hand, requires a more extensive set of inputs, which are categorised according to its sub-routine/file, e.g. General file, AeroDyn, ElastoDyn and InflowWind, taking into account that no hydrodynamic loads (HydroDyn) being an onshore setting, nor controller (ServoDyn) are incorporated. The input files are shown in Appendix D and every modification implemented is highlighted in light grey.

First, the general file contains overall instructions about the simulation inputs and outputs and serves as the main bridge between the DOS command window and the executable. In its 'Simulation and Control' section, the total run time and the time step is set. Similarly to the blade discretisation optimisation, these parameters were optimised to 10 and 0.1 s respectively, as seen in Appendix B. Furthermore, the modules are activated and deactivated correspondingly, hence 1 for ElastoDyn, InflowWind and AeroDyn (v.14), and 0 for the others unused. In consequence, the paths to the aforementioned modules are indicated in the subsequent section of the file, which are named with a subscript containing the associated wind speed ( $\_#WS$ ). Finally, the output is set such that the file can be read (.out) and that the time step corresponds to the one of the simulation.

Second, regarding AeroDyn, since the tower influence is not considered, the parameters below the hub and tip losses are set to "False". Moreover, the number of aerofoils is set to 12 according to the blade discretisation described before. Consequently, the aerofoils' path names are written beneath. Lastly, a table is included, which comprises the geometrical description of the rotor blade. Figure 5.9, helps to understand the meaning of the concepts not yet introduced such as RNodes and DRNodes. The first refers to the radial position of the centre of certain node (from the previous discretisation), and the latter is the distance from the current RNode to the previous one. In the case of the first node, it is computed taking into account that the scaled-up hub ends at 2.8 m. For simplification purposes, all DRNodes are set equal to 7.2 m. Therefore the RNodes are calculated according to equation (5.1), as follows:

$$\begin{cases} RNode_n = RNode_{n-1} + DRNode, 2 \leq n \leq 12 \\ \text{with } RNode_1 = 2.8 \text{ m} + \frac{1}{2} \cdot DRNode = 6.4 \text{ m} \end{cases} \quad (5.1)$$

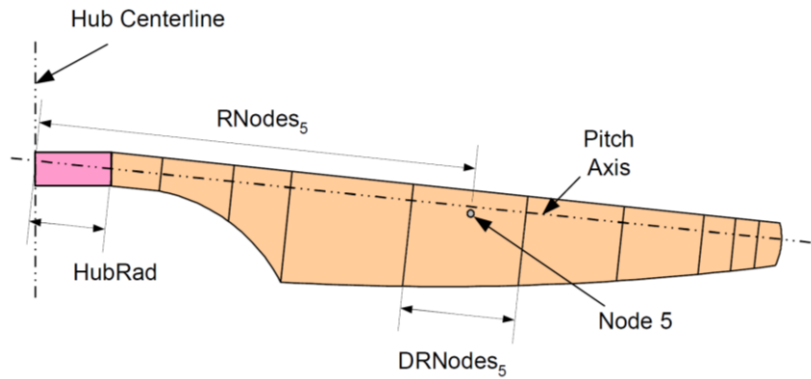


Figure 5.9 Representation of AeroDyn14's input parameters [38]

With respect to ElastoDyn, the corresponding time step for the calculations of motions is entered, which as seen in Appendix B, was optimised to 0.01 s. In addition, the rigid condition for the blades, drivetrain and tower are set by cancelling all related D.o.F., which will effectively restrict the flexibility of such components. In the case of the blades, no flapwise or edgewise bending is allowed. For the drivetrain, there is no torsion, and the rotational speed is fixed to a fixed value, i.e. there is no dominance of the controller whatsoever, even if there would be one. Subsequently, regarding the tower, there is no yaw motion nor fore-aft and side-to-side bending allowed in any of its sections. Finally, the D.o.F. of the floating platform are neglected, provided that these simulations are to be run in an onshore setting.

Furthermore, bearing in mind that there is no controller that is able to vary the rotational speed and the pitching of the blades for every wind speed (CPC), these parameters need to be imposed for all simulations. This is important because the purpose of the controller is to achieve the maximum power in the full-load region and keep the power to the turbine's rating in the partial-load region (before and after rated wind speed respectively).

The combined rotational speed and pitch strategy to be entered was obtained from the equilibrium state of the full-scale simulations run by DTU with a controller, under a rigid non-pre-coned non-pre-bent non-tilted RNA condition, which is depicted in Figure 5.10 below. The main benefit of entering this strategy instead of using the controller is that for coming projects to be developed under the methodology presented in this work, certain flexibility is offered, which allows to focus on the aerodynamics. For the sake of running in batch, the integrated design tool writes these values for every wind speed in an ElastoDyn file, as depicted in Appendix D for rated wind speed.

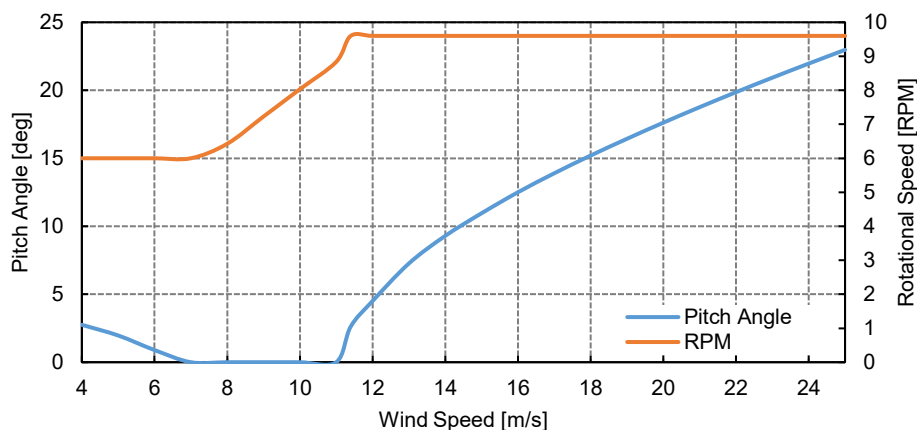


Figure 5.10 Fixed control strategy DTU 10MW [32]

In addition to the D.o.F. and the combinatory control strategy, the RNA axis is set to be completely horizontal and aligned with the incoming wind. For this purpose, the pre-cone values for all three blades and the rot shaft tilt are switched to zero. Finally, the names of the outputs needed for further analysis by the integrated design tool are indicated at the end of the file. Specifically, these are thrust and power, from which the non-dimensional coefficients can be computed. The rotational speed and pitch can be added to verify that they remain constant.

To close, the InflowWind file is modified in two sections: first, the inflow wind speed is set according to the simulation being processed, and second, an individual output to verify this main parameter is instructed to be printed to the final output file. With these, the set of file inputs for FAST is concluded.

### *PropArt*

Setting the sample size is a task of much importance, given the nature of the simulation. Since a genetic algorithm is implemented, it ranks the options from best to worst and then combines the properties of the best in order to mutate into a new geometry. This process goes on until the population of geometries, i.e.  $generations \times geometries / generation$  has entirely been analysed. For this reason, it is necessary that the size is large enough to generate a significant amount of cases, and not that large that it would take a significant amount of time, e.g. longer than a full week. Based on experience from several runs, the number of generations should be at the most 30 and the number of geometries per generation 100. This will also depend on the rate of success, considering that not all geometries are suitable to be analysed, with each one of the individual tools integrated.

## 5.3 Validation Inputs

As seen at the end of previous chapter, the combined effort of Rhinoceros, HEXPRESS and ReFRESCO rendered in a successful validation of the CFD calculations for the DTU 10MW at full-scale. In this sense, this section treats the input parameters to be employed in the validation of the model-scale design of the wind turbine rotor blade, which is the main subject of the present work. For this purpose, the geometry and domain characteristics are introduced, and the meshing and settings for calculations are stated.

### 5.3.1 Geometry

Once the optimal geometry is obtained by means of the integrated design tool, it is then exported with the aid of a Matlab-based script, which writes the parametrisation into a '.ppg' file that is read by Grasshopper, with the help of MARIN's Rhino plugins. With the geometry on Rhinoceros, it is then possible to refine, upscale, replicate, mount it and mesh its surface. It is important to note that the pitch is kept as zero, provided that the calculations will be done based on TSR and not over wind speed, as indicated in the full-scale case. Additionally, the leading edge is straight (non-skewed) and oriented towards the direction of rotation (clockwise). This is important because this is not the case for the visual representation of the rotor on PropArt, although for FAST calculation always a straight leading edge well-oriented is considered.

### 5.3.2 Computational Domain

Just as the geometry is imported in Rhino, the domain is created by the Grasshopper-based algorithm. For this purpose, it is of great importance to set its dimensions since it is desired that the flow making contact with the body is fully developed. Therefore, the domain dimensions should be large enough to prevent the flow layers close to the domain's inner surface from influencing the ones close to the body's external surfaces. According to Make's

work on the numerical study of the NREL 5MW and MSWT with ReFRESCO [70], the dimensions of the domain dimensions should be determined based on Figure 5.11. These are a function of the rotor's diameter. Here sides A, B and C correspond to the inflow, pressure boundary and outflow respectively. For the current simulations, the factor  $n$  is considered as 15 in order to achieve an undisturbed airflow.

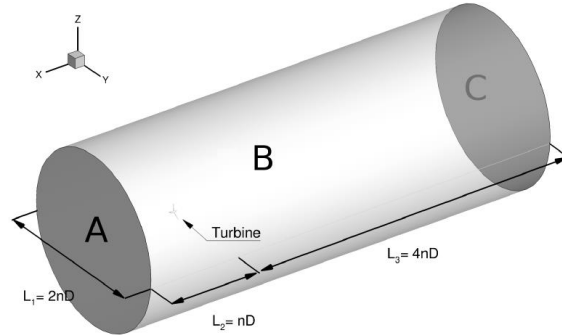


Figure 5.11 3-D Computational Domain for CFD Calculations [70, 80]

### 5.3.3 Grid Refinement

To the end of establishing the most appropriate grid size, generally, a grid refinement study is performed as indicated in section 4.4.2. Nevertheless, for this case, it is also taken into consideration the outcomes from previous numerical study done on the MSWT, which are summarised below in Table 5.5. In order to relate to the concepts contained in it, these are defined as follows: First, the grid refinement ratio is the quotient between the sizes of two adjacent cells preferably located around a surface, such as the blade tip as seen in Appendix A. The errors are measured with respect to a nominal wind speed and the thrust coefficient to the finest grid (No. 5), respectively. Furthermore, the residuals are the normalised errors in response for two timesteps, consecutive for  $L_2$  and with respect to a reference value for  $L_\infty$ . To clarify this, an error is the difference between inputs, whereas the residual is the difference between outcomes. The objective of the residuals is to establish how many iterations should be performed in order to achieve certain level of error.

Table 5.5 Outcomes grid refinement study for MSWT [70]

Grid No.	Total No. of Cells	Grid Refinement Ratio [-]	No. of Iterations	Absolute Error on inflow	Absolute Error on $C_T$	$L_2$ residuals on Velocity [-]	$L_\infty$ residuals on Velocity [-]
1	8,371,928	1.52	8,283	2.78%	0.37%	$1.4 \times 10^{-5}$	$1.24 \times 10^{-2}$
2	13,406,225	1.30	15,000	2.15%	0.23%	$3.4 \times 10^{-5}$	$2.8 \times 10^{-2}$
3	18,559,122	1.17	15,000	1.78%	-0.06%	$7.9 \times 10^{-7}$	$1.6 \times 10^{-3}$
4	23,907,087	1.07	15,000	1.56%	-0.18%	$1.7 \times 10^{-5}$	$9.0 \times 10^{-3}$
5	29,558,234	1.00	15,000	1.39%	0.00%	$1.7 \times 10^{-5}$	$9.1 \times 10^{-3}$

From this exercise, and taking into account that less computational power required is desired, it can be inferred that the grid refinement in the third position is appropriate for its application in the model-scale calculations. The version of HEXPRESS currently employed (6.2), with respect to the one utilised in Make's work (4.1) includes among others an optimised procedure for viscous layer insertion, which improves (decreases) the number of cells. Therefore, upon application of the grid refinement to the set of body and domain, the count adds up to 12 million, which comprise all 7 groups of surfaces: Blade 1, 2 and 3; Hub, Outer; Inflow and Outflow.

### 5.3.4 CFD Calculation Parameters

As seen in the previous section, it is of great relevance to mesh the body and the computational domain in a proper fashion. Therefore, in order to achieve such refinement, subsequent steps to an initial meshing of 30 w x 30 h x 75 d (67,500 cells), must be followed. For this reason, as well as done in the validation of the baseline (at full-scale) in section 4.4.5, the parameters from Table 4.6 remain constant, but the refinement at the blade tip's leading edge is increased to 16.

For every calculation, ReFRESH as well as FAST, requires a file that summarises all the inputs and re-directs some instructions to specific files, i.e. the 'controls' file (not disclosed in this work). For that purpose, the main inputs are presented in Table 5.6. First, the inflow and rotational speed of the rotor are required. It is important to note that all values consigned here have been scaled-down, since CFD calculations can be run at model-scale. For clarification purposes, the here so-called reference velocity is the magnitude of the relative velocity vector  $U_{rel}$  from the Blade Element Theory. This is asked by ReFRESH, as well as the chord length at a 70% radial station, in order to calculate the Reynolds regime. In addition, the only boundary condition stated in this file relates to the non-translation of the RNA, which effectively means that it remains in the same position throughout the entire simulation. That is, the motion is purely rotational.

Table 5.6 Inflow and RNA operational parameters for model-scale CFD calculations

Case No.	TSR [-]	Model-scale Wind Speed [m/s]	Model-Scale Rotational Speed [rad/s]	Reference Velocity at 0.7R [m/s]	Reference Length at 0.7R [m]
1	4.48	2.582	7.787	8.484	0.0732
2	7.50	1.543	7.787	8.191	0.0732
3	9.34	0.774	4.867	5.104	0.0732

Furthermore, these computations are steady, which means that the flow is constant over time at a particular point in the domain circular area of influence. Furthermore, in order to handle rotational motions of the rigid body the Absolute-formulation Method (AFM) is implemented. This means that the RANS equations are solved with the moving reference frame (rotating flow) but written in terms absolute (inertial) reference frames [81]. In addition, the rotation axis is  $\langle 1, 0, 0 \rangle$ , i.e. the horizontal, and the gravity is not taken into account in order to focus on the behaviour of the RNA upon the interaction with the flow.

With regard to the convergence of the solution, Table 5.7 lists all the convergence-related parameters entered into the controls file, including the implicit and explicit relaxation factors, which have an influence on the speed at which the convergence is achieved. Lower values render in more stable and slower convergence [81].

Table 5.7 Convergence parameters for CFD calculations

Parameter	Outer Loop	Momentum Equations	Pressure Equations	Turbulence Equations
Convergence / Divergence Tolerance	$1 \times 10^{-6} / 1 \times 10^9$	0.3	0.05	0.3
Max Iteration	20,000	300	500	200
Implicit Relax Min	N/A	0.25	N/A	0.2
Implicit Relax Max	N/A	0.9	N/A	0.9
Implicit Relax Iterations	N/A	1000	N/A	1000
Explicit Relax	N/A	0.3	0.15	0.3

# 6 Optimal Model-scale Rotor Blade Geometry: Results and Discussion

Several simulations were run with the integrated design tool using the inputs introduced in previous chapter. Product of these, four three-bladed geometries have been realised, which yield from variations of the optimisation model implemented. In this chapter, particularly in section 6.1, these are presented and further assessed in terms of shape and performance. Furthermore, the most suitable one is selected in order to be validated with ReFRESCO, whose results are further displayed and analysed in section 6.2.

## 6.1 Geometries Generated with the Integrated Design Tool

The optimisation model presented in section 4.1 is intended to optimise both the thrust and power coefficients while varying the chord and twist distributions of the rotor blade. However, as it was seen in section 3.1, where the previous design exercises for this very application, testing floating platforms for FOWTs, were introduced, the rotor blades were designed to meet the thrust non-dimensional performance and not the power. This is because, the thrust is one of the main design drivers for floating platforms, provided that it is desired that the support structure is able to withstand wind-, waves- and sea currents-based loading. The aerodynamic power on the other hand, is relevant when testing the performance of a particular wind turbine model, meant for power production. Nevertheless, the case in which the power is set as the secondary objective is also considered.

Furthermore, when validating the integrated design tool with the DTU 10MW, the variables were restricted to chord and twist, whereas for the model-scale in section 5.2.1, the thickness was introduced as variable and a parametrisation was given. The motivation behind this is to determine the impact on the rotor blade final shape of giving the thickness freedom to vary. For the aforementioned reasons, this case is considered as a variation of the constraints. The simulations run and therefore, blade geometries obtained (in the same order) are presented below in Table 6.1.

Table 6.1 Blade geometries from integrated design tool

Simulation Identifier		Variables	
		Chord and Twist	Chord, Twist & Thickness
Objective	Thrust & Power Coefficients	1	2
	Thrust Coefficient alone	3	4

For future references, the blade geometries are presented in the following fashion: first, the optimisation progression is displayed; followed by the 3-D model from PropArt; then the chord, twist and thickness distributions are shown. Finally, the aerodynamic performance is depicted for further analysis.

### 6.1.1 Blade Geometry No. 1

The simulation that yielded in this geometry was run for 2,000 iterations (20 generations of 100 individuals each), contrary to was stipulated for the size of the population in section 5.2.3. This is because there was no further improvement evidenced in the solution between generations (different colour in the optimisation progression figure), as depicted in Figure 6.1. Here it is circled the selected geometry, for being in the lowest apparent point from the Pareto optimal front.

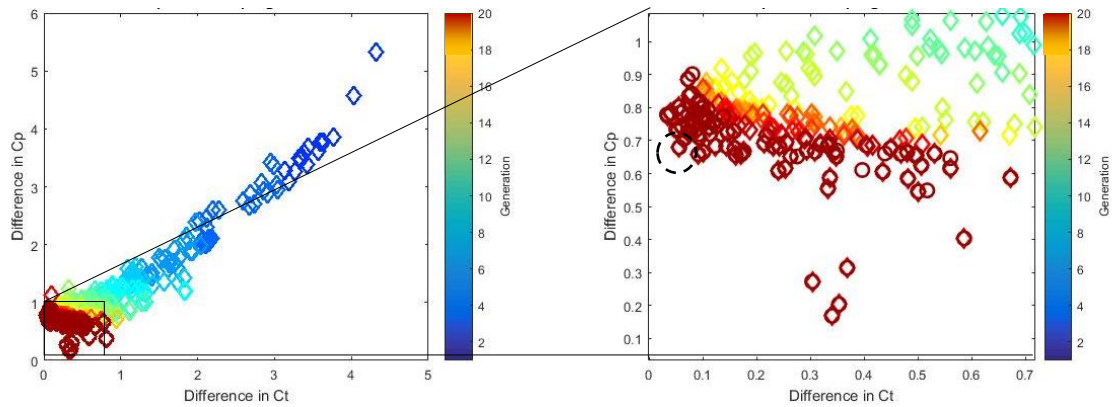


Figure 6.1 Optimisation progression for simulation No. 1

Furthermore, at first sight from Figure 6.2, the blade seems to have an increased chord distribution relative to the slim one from the baseline turbine, in agreement with the similar exercises found in literature. It can be noticed here that the blade is not correctly oriented, since the leading edge is facing the counter-clockwise direction of rotation and it is not straight as examined before. This is merely a visualisation that does not represent accurately the geometry being simulated in FAST, although this was corrected after by modifying the skew distribution. Nevertheless, the cylinder section at the blade root is well kept for the purpose of connecting it to the hub.

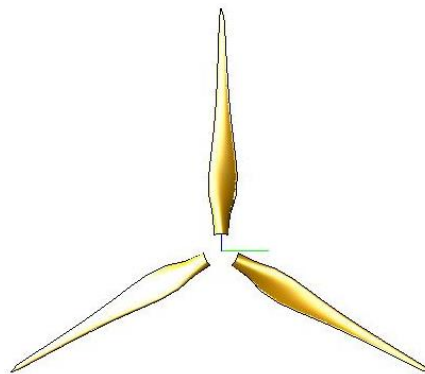
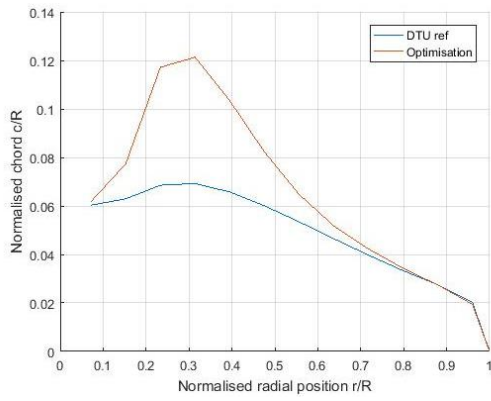


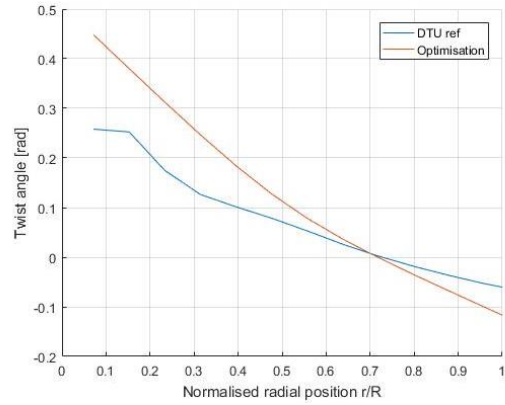
Figure 6.2 3-D Representation of the selected rotor blade geometry from simulation No. 1

With respect to the representative distributions, subjected to variation within the optimisation model, i.e. chord and twist, it can be evidenced that in fact there is a substantial increase in the chord to 12% of the radius in comparison with the baseline, particularly at 30% radial station. This is because at larger Reynolds numbers, which was seen in section 5.2.3 depends directly on the chord, there is a slight increase in the  $C_L/C_D$ , which yields in higher power and thrust. The increase in chord is bound by the constraints in the parametrisation (see section 5.2.1) and the need to connect with the fixed cylinder at the root.

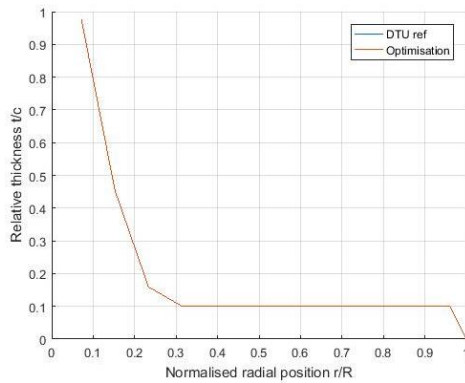
On the other hand, the twist is seen to follow the same decreasing trend, although its starting point is much higher than the reference. This is a consequence of the search for the optimum lift-to-drag ratio, which as seen from Figure 5.2, is close to  $12^\circ$  (0.21 rad) for the innermost aerofoil. As expected, there is no change in relative and absolute thickness distributions with respect to the baseline since this variable was not part of the optimisation.



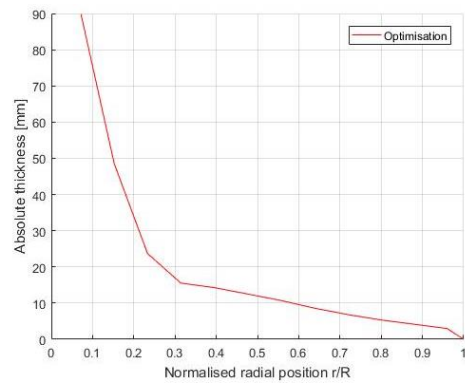
a. Chord



b. Twist



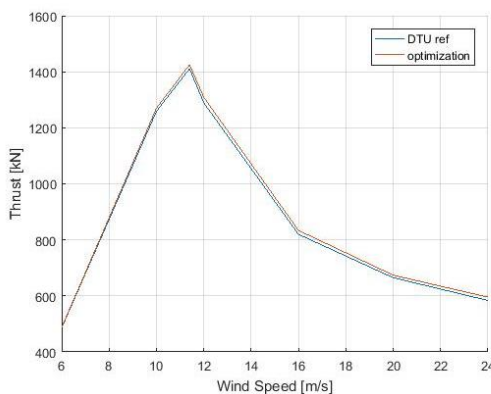
c. Relative thickness



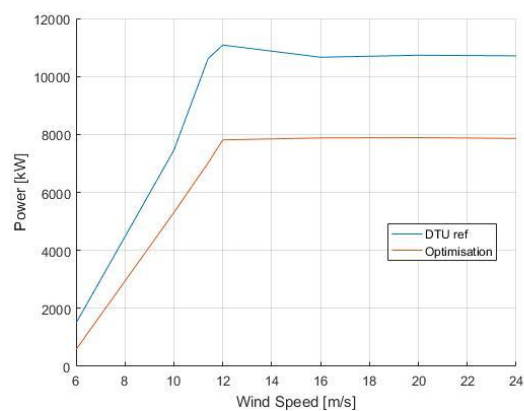
d. Absolute thickness

Figure 6.3 Representative distributions of blade geometry No. 1

When this blade geometry is replicated (to make a 3-bladed assembly) and coupled to the hub, the aerodynamic performance illustrated in Figure 6.4 is obtained. Here, the comparison in thrust and power with respect to the baseline performance is depicted. It is evident that there is a very close match in the thrust for all wind speeds analysed, whilst the power is underestimated for this design. This is because the imposed combination of pitch and rotational speed is sub-optimal for this blade design.



a. Thrust



b. Power

Figure 6.4 Aerodynamic performance of a rotor with blade geometry No. 1

### 6.1.2 Blade Geometry No. 2

Now, the thickness is included into the optimisation, and from this implementation, a blade geometry is obtained. This simulation was run for 5200 iterations (52 geometries x 100 generations). The geometry selected is again highlighted in Figure 6.5 with a circle, under the same assumptions from the previous case.

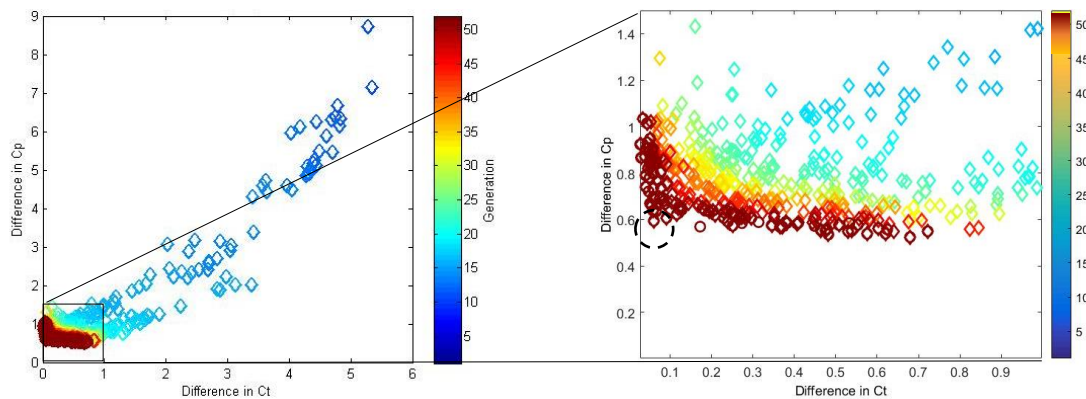


Figure 6.5 Optimisation progression for simulation No. 2

The selected geometry renders in the following 3-D rotor, whose blade is in fact, slimmer in chord than blade No. 1, yet more pronounced than the baseline design.

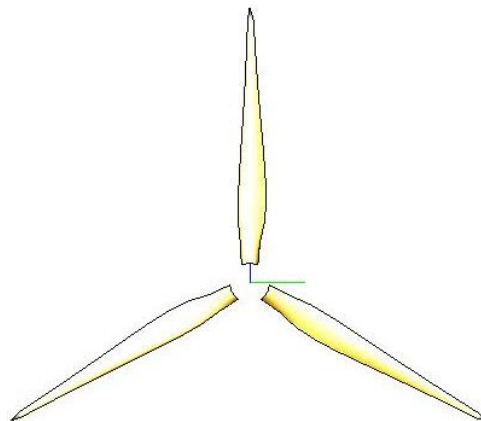
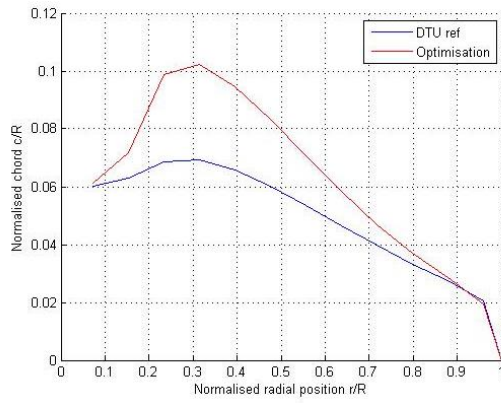


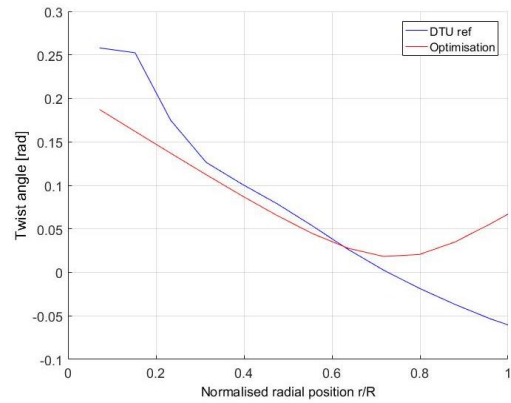
Figure 6.6 3-D Representation of the selected rotor blade geometry from simulation No. 2

In detail, Figure 6.7 displays the representative distributions for blade geometry No. 2. Here, it can be evidenced that the chord has a peak slightly higher than  $0.1R$  at 30% blade station, which is still lower than the benchmark values, yet reasonable. In addition, with respect to the twist, its shape does not agree with the expected trend since after 70% of the blade span the angle starts to increase. This is an abnormal behaviour, which indicates that the high inflow angle gives priority to tangential forces rather than to the normal ones, derived from the lift and drag respectively in the Blade Element Theory (explained in section 2.2.1).

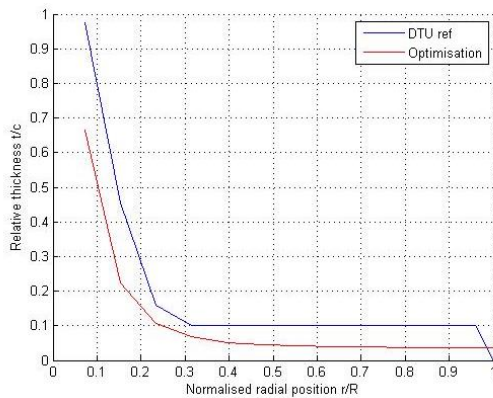
With regard to the thickness yielded from the optimisation, it can be noted that it is yet lower than the baseline with the implementation of the thinner aerofoils for low-Reynolds. This is undesirable since the manufacturing constraint must be respected. To verify this, the absolute thickness is plotted compared to the thin baseline, and it shows that in fact, the values at before the tip are close to 1 mm, which is inadmissible from the manufacturing point of view.



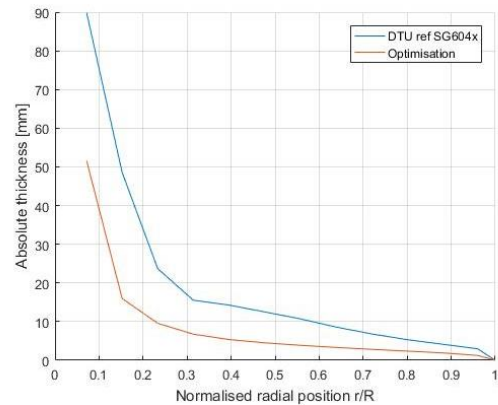
a. Chord



b. Twist



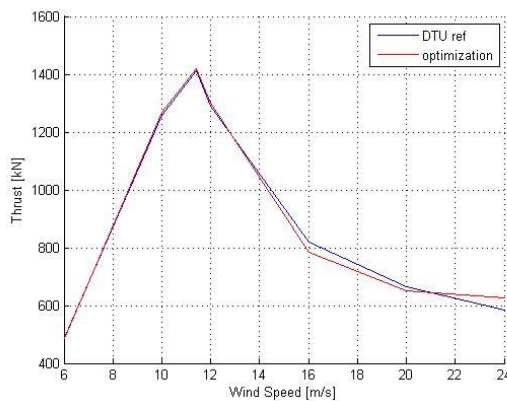
c. Relative thickness



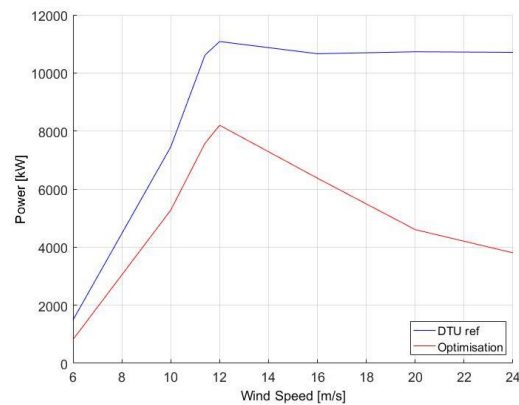
d. Absolute Thickness

Figure 6.7 Representative distributions of blade geometry No. 2

Regardless of the shape of the resulting blade, the aerodynamic performance is here analysed. From Figure 6.8 it can be inferred that there is an almost perfect match for the thrust for all wind speeds under 16 m/s, and from then minor discrepancies are noted. However, the case of the power is much more severe, since there is no match within the range of analysis for the reason presented for the previous blade geometry. In addition, beyond rated wind speed the power drops, as a consequence of the non-conventional twist and thickness distributions, which distort the aerodynamic performance of the initially selected aerofoils.



a. Thrust



b. Power

Figure 6.8 Aerodynamic performance of a rotor with blade geometry No. 2

### 6.1.3 Blade Geometry No. 3

The following simulations focus on optimising the thrust, i.e. minimising the difference in the thrust coefficient with respect to reference values from the DTU 10MW for several wind speeds. The results of the first run that do not consider the thickness as variable in the optimisation model are presented in Figure 6.9. In this case, there is an obvious choice, the last point in the optimisation progression after 3,000 iterations, since it is assured the least difference in  $C_T$ .

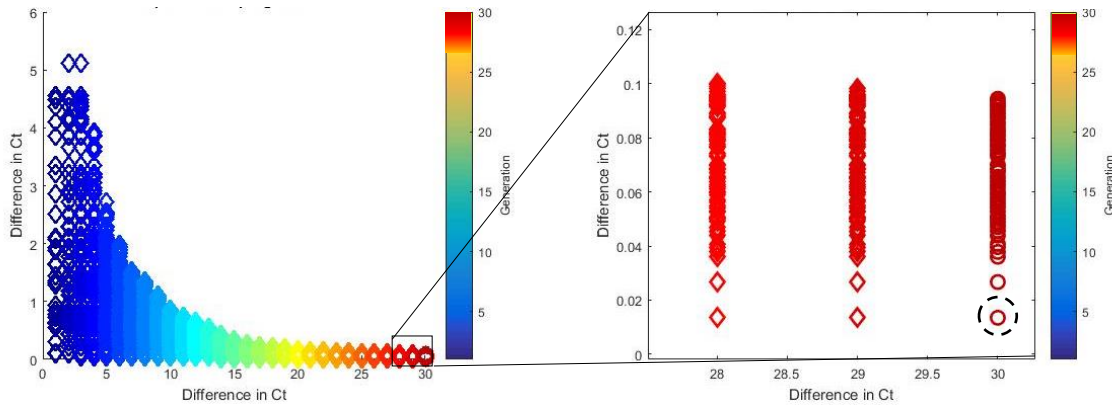


Figure 6.9 Optimisation progression for simulation No. 3

This blade geometry, depicted in Figure 6.10 seems at first sight similar in shape to No. 1. This needs to be confirmed with a close look at the distributions.

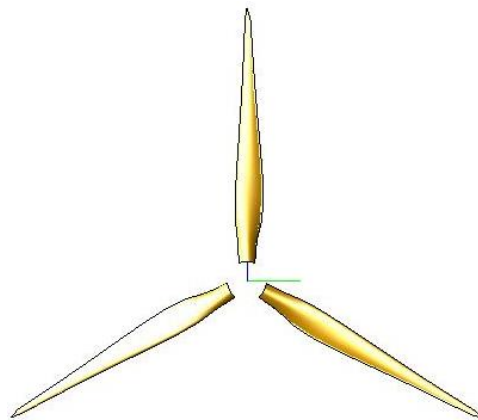
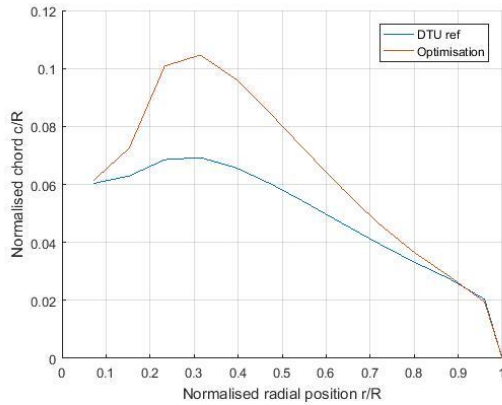
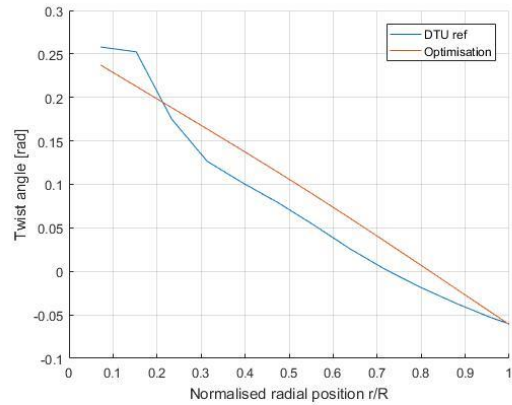


Figure 6.10 3-D Representation of the selected rotor blade geometry from simulation No. 3

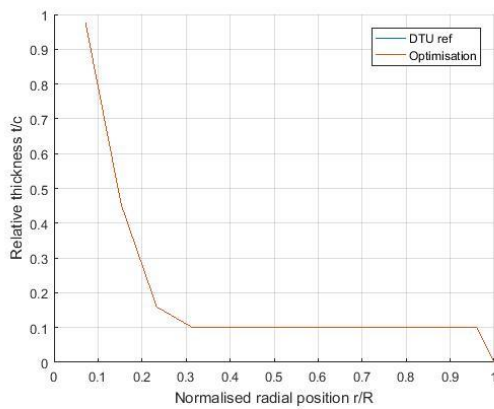
Likewise, the representative distributions are presented below in Figure 6.11. From these, the decreasing straight twist distribution stands out, which does not incorporate extreme values to achieve good aerodynamic performance at the blade root. Although there are no constraints in this respect, this blade geometry also brings advantages from the manufacturing point of view. Furthermore, the chord distribution shows no significant differences with respect to blade geometry No. 1, being the maximum also at 30% radial position, with a value of 10.5%, as opposed to 12%.



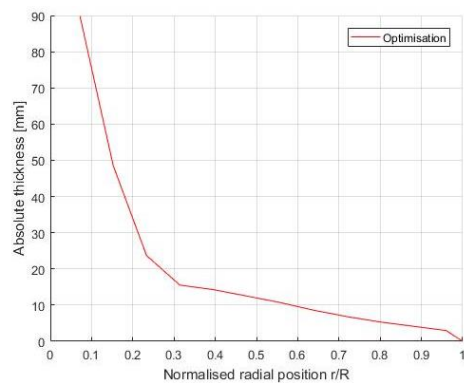
a. Chord



b. Twist



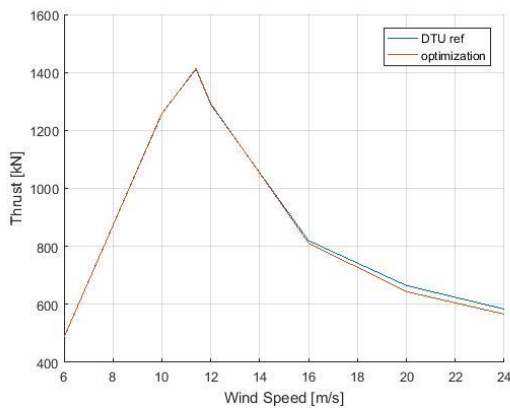
c. Relative Thickness



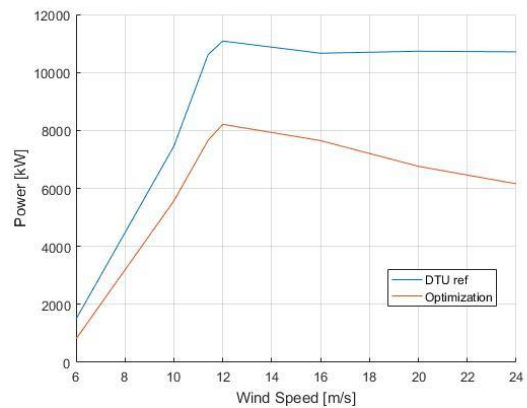
d. Absolute Thickness

Figure 6.11 Representative distributions of blade geometry No. 3

The aerodynamic behaviour, i.e. the thrust and power is depicted in Figure 6.12. Naturally, it was not expected an agreement in the power with respect to the reference values, since this optimisation did not incorporate the power as an objective function, which is evidenced here. Nevertheless, the match of the thrust is almost perfect, which goes in line with the goal of this exercise.



a. Thrust



b. Power

Figure 6.12 Aerodynamic performance of a rotor with blade geometry No. 3

### 6.1.4 Blade Geometry No. 4

The final set of simulations is here presented. In this case, 5,000 iterations were run for optimising the thrust alone with the incorporation of the thickness as variable. As explained before, one geometry from the last generation is chosen, expecting the minimum difference in the thrust coefficient as seen in Figure 6.13.

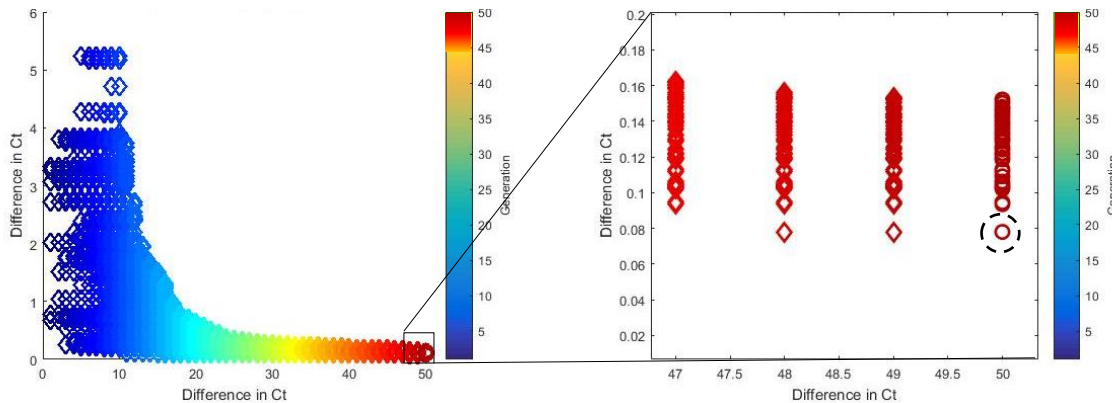


Figure 6.13 Optimisation progression for simulation No. 4

From this selection, the 3-D representation presented in Figure 6.14 shows a blade with a slight increase in the chord with respect to the baseline. This fact can be confirmed by Figure 6.15.

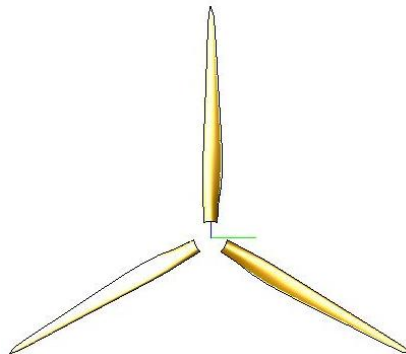
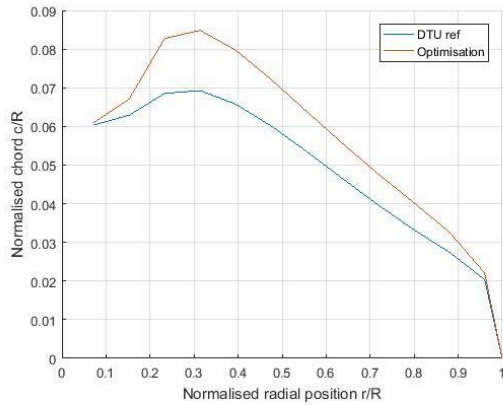


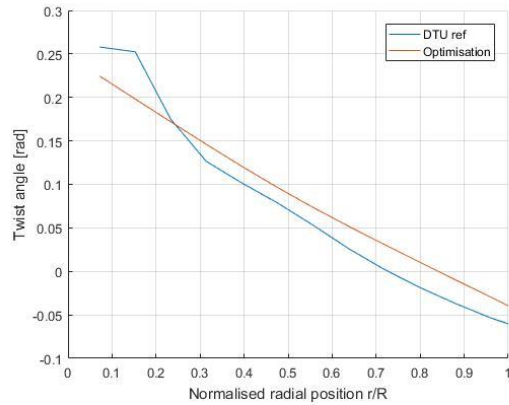
Figure 6.14 3-D Representation of the selected rotor blade geometry from simulation No. 4

This blade's chord distribution shows a minor increase at 30% radial position when compared with the afore-described geometries, which renders in a slow transition towards the tip. This means that the chord seems displaced upwards from the baseline case. Nonetheless, the twist presents a reasonable shape, analogue to geometry No. 3, with a lower starting point and descent above the baseline.

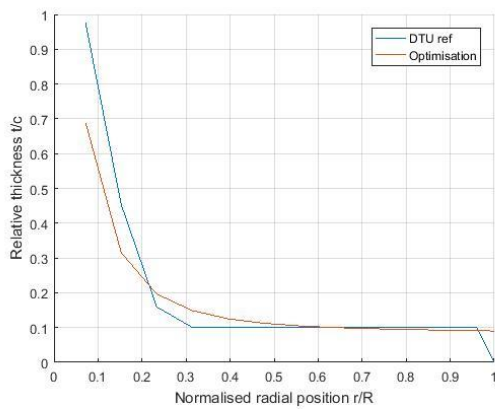
The thickness optimisation shows in the last sections a convergence to the baseline original setting. This is positive because it can be inferred that the baseline aerofoil selection is already suitable for this design, which effectively reduces the variables to be considered within the optimisation model. However, at the beginning, there is a considerable step from the cylinder to the first section at 10% radial position. In spite these advantages and disadvantages, the manufacturing constraint is not violated since the minimum absolute thickness before the tip is 2.9 mm.



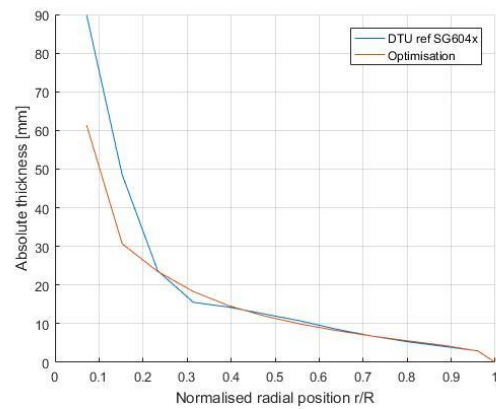
a. Chord



b. Twist



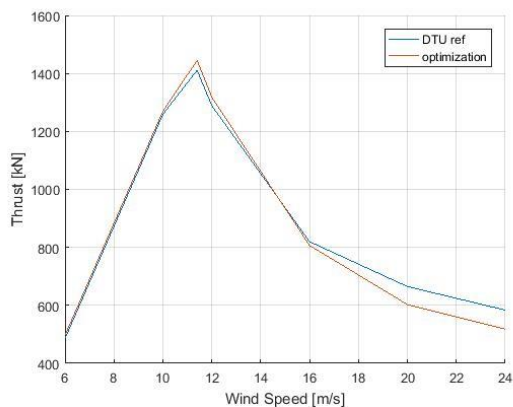
c. Relative Thickness



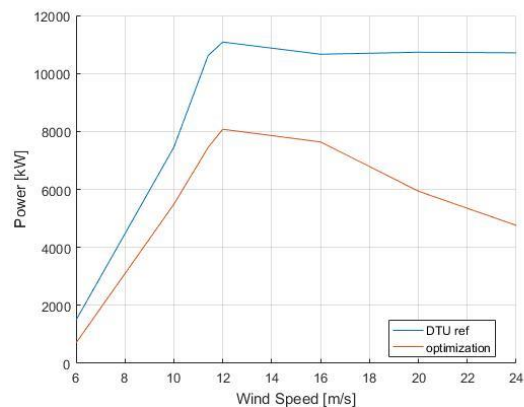
d. Absolute Thickness

Figure 6.15 Representative distributions of blade geometry No. 4

As for the aerodynamic performance since the chord distribution is not considerably higher than the baseline, yet still comprising low-Reynolds aerofoils, it is expected that the thrust does not fully agree with the reference values. This can be evidenced in Figure 6.16, where there is a mismatch at rated wind speed and larger beyond 16 m/s. Likewise the power curve displays a poor behaviour, similar to all of the above geometries.



Thrust



Power

Figure 6.16 Aerodynamic performance of a rotor with blade geometry No. 4

### 6.1.5 Selection of Optimal Blade Geometry

Four blade geometries have been introduced and one is to be selected for validating its performance with the aid of CFD computations. Here a comparison is made and the most suitable blade geometry to carry out the task is chosen.

Stepping aside from the fact that matching the power, and therefore the power coefficient brings some challenges when there is no active pitch control, clearly, there are many options to choose from when designing a rotor blade. This is because there is a large amount of combinations possible between variables that can yield in similar performance. For instance, a slight difference in chord and different twist distributions between two geometries can render in a close match in the thrust with respect to the baseline reference values and similar power outputs, e.g. blades No. 1 and No. 3. Ideally, more than one geometry could have been selected for every combination of the changes in the optimisation model, in order to achieve statistical significance. Nonetheless, only one blade geometry was further assessed taking into account the aforementioned criteria.

When looking at the incorporation of the thickness as an optimisation variable, it can be inferred that there is nothing but loss of quality in the outcomes. This is seen in both blade geometries No. 2 and No. 4. For instance, blade No. 2 resulted with a non-conventional-shaped twist distribution and the thickness itself achieved very low values, which are not suitable for manufacturing purposes. Even though the thrust behaves properly, the power drops rapidly after rated wind speed. On the other hand, the quality of the chord distribution achieved for blade No. 4 is relatively poor, rendering in a mismatch in the thrust at extreme wind speeds. For those reasons, neither of these two blade geometries are further considered for analysis.

In order to select the most suitable blade geometry among the remaining two options, i.e. No. 1 and 3, it all comes to determining what the influence of considering the power as a secondary objective is into the resulting blade shapes. In this sense, it can be inferred that when trying to achieve certain power rating, the chord increases in search for a higher Reynolds number as explained before, this yields in a more pronounced crest at 0.3R of the blade No. 1 in contrast to blade No. 3. In addition, the twist varies accordingly to the end of achieving higher lift-to-drag ratio, responsible for the increase in power.

To conclude, the inclusion of the power as a secondary objective in the optimisation model is not detrimental for the thrust, yet it generates minor changes on the shape of the blade. Since neither of the geometries was able to perform well on the power, the comparison is made based on the shape and thrust-matching capabilities. Therefore, for simplification purposes and for future references, the optimisation model is restricted to minimise the difference in the thrust coefficient, which means that the selected geometry is No. 3, described in Table 6.2.

*Table 6.2 Description selected blade geometry*

Section No.	r/R [m/m]	c/R [m/m]	$\theta_T$ [deg]	t/c [m/m]	t [ $\times 10^{-3}$ m]
1	0.072	0.061	13.590	0.975	89.018
2	0.153	0.072	12.188	0.454	48.845
3	0.233	0.101	10.784	0.159	23.882
4	0.314	0.105	9.375	0.100	15.624
5	0.395	0.096	7.954	0.100	14.325
6	0.476	0.084	6.511	0.100	12.542
7	0.556	0.071	5.037	0.100	10.605
8	0.637	0.058	3.524	0.100	8.700
9	0.718	0.047	1.982	0.100	6.949
10	0.799	0.037	0.421	0.100	5.467

Section No.	r/R [m/m]	c/R [m/m]	$\theta_T$ [deg]	t/c [m/m]	t [ $\times 10^{-3}$ m]
11	0.879	0.028	-1.149	0.100	4.219
12	0.960	0.019	-2.723	0.100	2.893
Tip	1.000	0.000	-3.503	0.000	0.000

## 6.2 Validation of Selected Blade Geometry

With the optimal blade geometry selected, it is important to establish the reproducibility of its aerodynamic performance values; and for that purpose, in this section the validation outcomes are analysed. To this end, blade geometry No. 3 was simulated with the aid of ReFRESKO (MARIN's in-house RANS solver) using the inputs previously described in section 5.3. Now, as done in the full-scale validation exercise, the quality of the results is examined through the analysis of the non-dimensional wall distance and the flow visualisation, illustrated in Figure 6.17 and Figure 6.18 respectively.

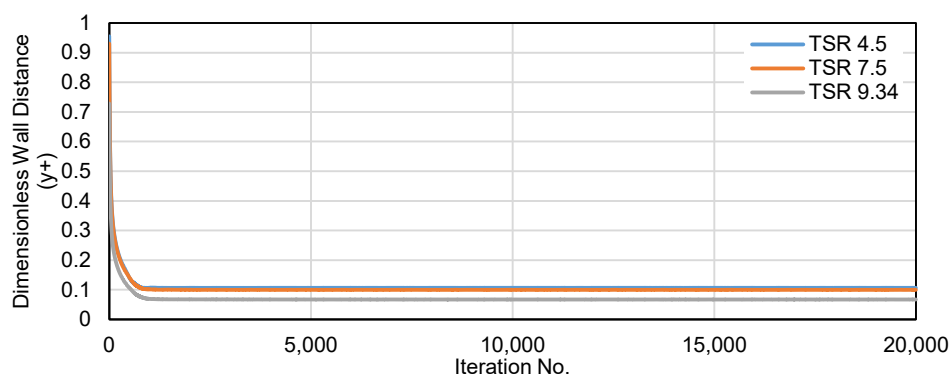
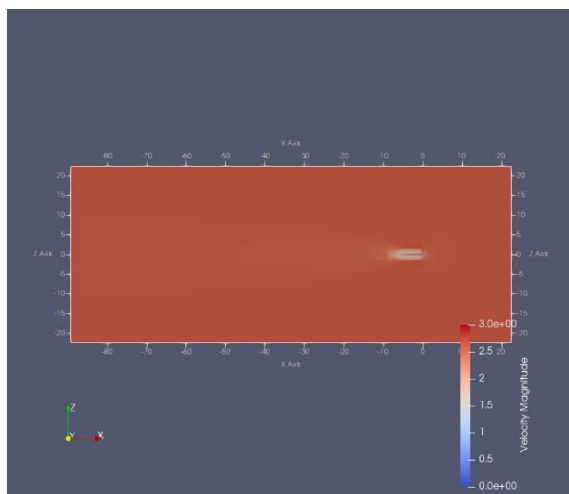
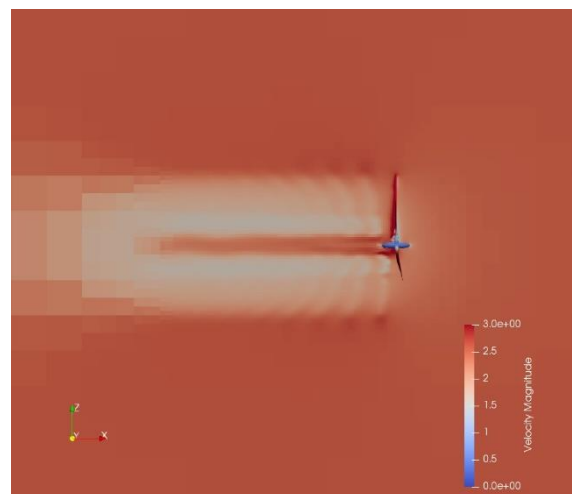


Figure 6.17 Dimensionless Wall Distance for Modell-scale CFD Simulations

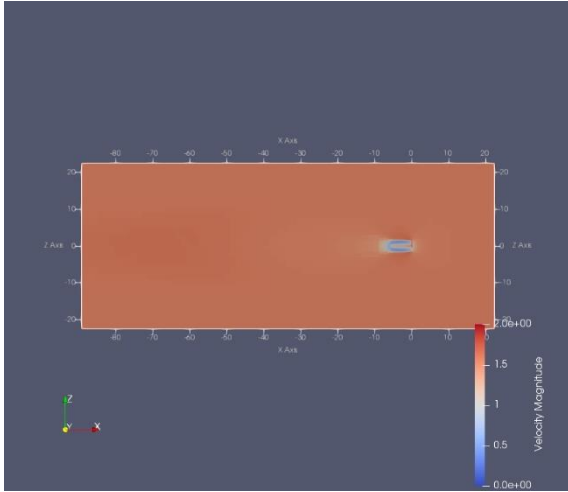
From the above, it can be inferred that the  $y^+$  criterion is met throughout the duration of the simulations, i.e. a value lower than 1.0 was achieved. On the other hand, in the flow visualisation below it can be seen the rotating wake behind the rotor for all TSRs subjected to analysis (9.34, 7.5 and 4.5, related to full-scale wind speeds of 6, 11.4 and 20 m/s). This comes with a natural wind speed reduction due the energy extraction from the incoming flow. No vortices nor unsteadiness are evidenced, which means that the steady-flow condition was kept, achieving convergence of the results.



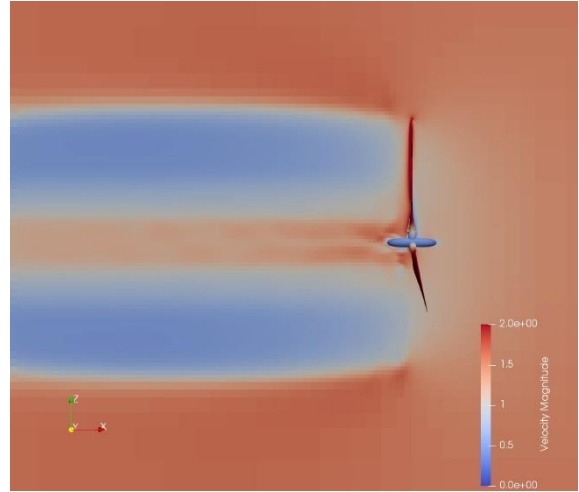
a. Overall Flow at TSR = 4.5



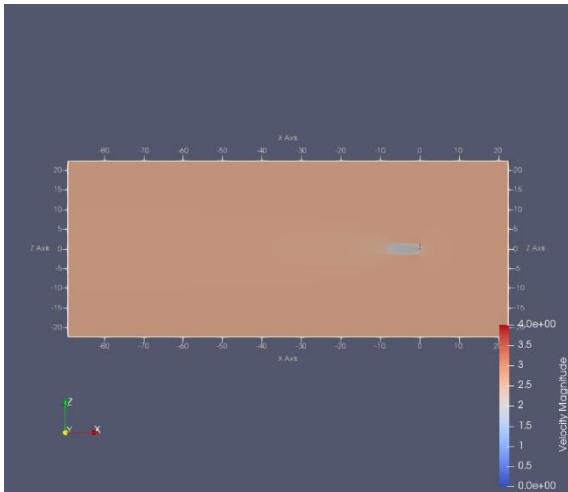
b. Localised Flow at TSR = 4.5



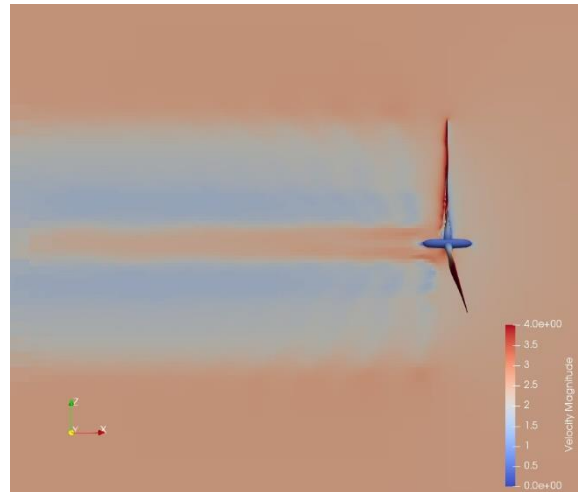
c. Overall Flow at TSR = 7.5



d. Localised Flow at TSR = 7.5



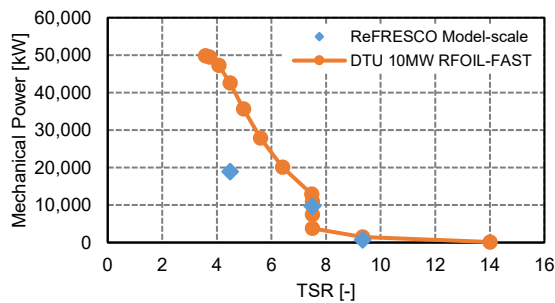
e. Overall Flow at TSR = 9.34



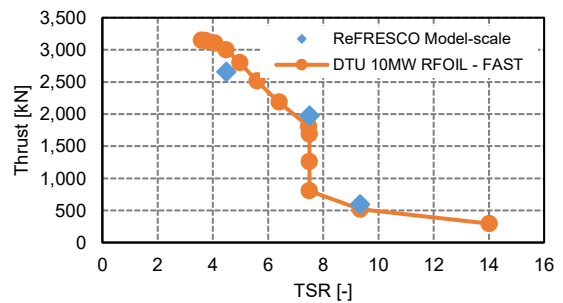
f. Localised Flow at TSR = 9.34

Figure 6.18 Visualisation of the flow for the model-scale wind turbine at 3 TSRs

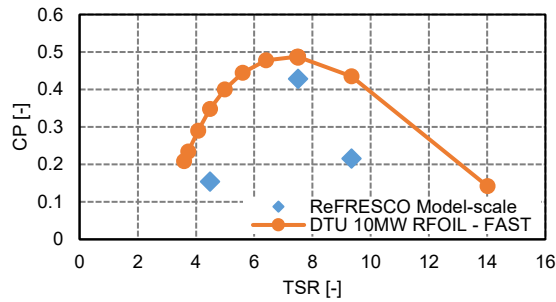
With regard to the results, as well as in the full-scale, the point of reference is the outcome from the simulation of the DTU 10MW using RFOIL and FAST without a controller. Figure 6.19 displays the comparative results for the aforementioned TSRs.



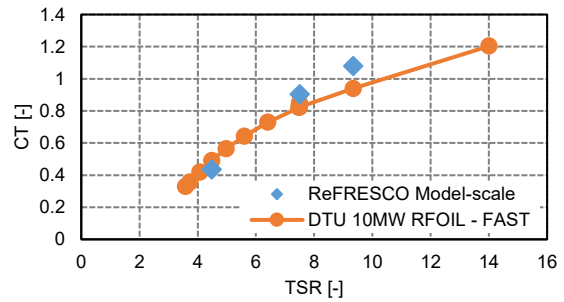
a. Power



b. Thrust



c. Power Coefficient



d. Thrust Coefficient

Figure 6.19 Aerodynamic performance of Blade Geometry No. 3 and the DTU 10MW with ReFRESCO and RFOIL-FAST

Considering that the optimal blade was designed to match the thrust and not the power, it was expected that this feature would not perform well, especially beyond rated wind speed. This is evidenced for the TSR corresponding to 20 m/s, where there is a large mismatch in the power. In addition, variations that are imperceptible by the naked eye render in a larger discrepancy in the non-dimensional power.

On the other hand, CFD values for the thrust, and consequently the thrust coefficient agree with the reference. From this, two main conclusions can be drawn: first, that in fact the selected blade yields in a thrust coefficient close to the one pertaining to the DTU 10MW. This means that when it is constructed and implemented for its testing in MARIN's Offshore Basin, it would accomplish its goal of reproducing the thrust required during the testing of the floating foundation. Second, the agreement of the CFD values is also a reflection of an appropriate set of inputs for validation purposes, i.e. the selection of the computational domain and proper meshing.

# 7 Conclusions and Recommendations

In this chapter, the concluding remarks are provided for every research objective traced for this work and reflected in this report. Additionally, recommendations to be taken into account for future research exercises are given.

## 7.1 Concluding Remarks

### 7.1.1 Theoretical Objectives

*Investigate the scaling methodologies available and find the most suitable that decreases the impact of the Reynolds effects on the wind turbine rotor blade design, when a Froude-based approach is implemented.*

Among the scaling methodologies available for testing FOWTs, model-scale blade design exercises performed in the past suggest that the Froude-based approach has proven to be the most suitable and consistent methodology. However, its implementation brings the so-called scaling effects when the aerodynamic performance is analysed, i.e. low-Reynolds regimes. Therefore, a new design of a wind turbine rotor blade was realised to cope with these effects. Other approaches to address this problem have been introduced in the past, however they face challenges when moving from the theory to the real-life implementation.

*Determine how important the incorporation of rotational effects into the aerodynamic performance of an aerofoil is in the wind turbine rotor blade design process.*

In the design of a wind turbine rotor blade, it is of great importance to take into account the rotational effects that yield in 3-Dimensional flow, which consequently renders into flow separation along the blade span. This phenomena induces stall delay and anticipation, inboards and outboards respectively, which are significant for the blade performance and therefore have repercussions into the blade final shape.

*Establish the significance of considering the effect of floating dynamics into the aerodynamic performance of the rotor blade during the design process.*

Clearly, the motions of the floating foundation have an effect on the blade's aerodynamic performance, which are characterised for a series of events that represent the unsteadiness of the surrounding air flow. Nevertheless, when analysing closely the impact on the aerodynamic outcome, these effects can be neglected for design purposes. Proof of this is the comparison between a spar- and an onshore-based simulations on FAST for a baseline turbine, which yielded in virtually no difference in both the thrust and power for the same wind speed.

### 7.1.2 Practical Objectives

*Define a reliable methodology for carrying out the aerodynamic design of a scaled-down wind turbine rotor blade, to be used in the testing of a floating foundation in a wind/wave basin.*

The methodology for the design of the wind turbine rotor blade at model scale that was capable of reproducing the non-dimensional aerodynamic performance of the DTU 10MW, introduced in this work proved to be efficacious, i.e. the integration of tools yielded successful results. Proof of this is that a blade design was reached, whose performance, computed with BEMT and validated with CFD 3-D, matched the thrust coefficient of the baseline, as intended for its implementation in the testing of a floating foundation in a wind/wave tank.

*Find and integrate reliable aerodynamic-based design tools capable of working together in an automated way for the purpose of designing a wind turbine rotor blade.*

The tools implemented to carry out the design and further validation were selected based on their availability, whether due to their individual open-source nature or the easiness to access them at the promotor's (MARIN) or at TU Delft's facilities. The combination of all the design tools resulted in a reliable integrated tool capable receiving overall inputs and transforming them into intermediate files to be read and further processed individually. In addition, in order to make this tool more efficient and therefore increase its effectiveness, a successful optimisation of the individual processing times of RFOIL and FAST was performed, without degrading the solution.

### 7.1.3 Design Objectives

*Determine the shape of the optimal geometry of a scaled-down wind turbine rotor blade that reproduces the non-dimensional aerodynamic performance of the full-scale DTU 10MW Reference Wind Turbine.*

The design methodology was successfully implemented with the aid of the integrated design tool at 1/60<sup>th</sup> scale and by incorporating SG604x series baseline aerofoils. These latter, were chosen for their improved aerodynamic properties, resulting from their relatively thin shape and low flow separation characteristics at the boundary layer. This exercise yielded in four geometries resulting from the combinations of whether the power as a secondary objective and the thickness as a variable should be included in the optimisation model. The outcome was negative for both, yielding in the selection of a blade geometry (No. 3), which was meant to match the thrust coefficient alone and keep the thinner baseline aerofoil distribution. As expected, the normalised chord distribution was larger than the DTU 10MW, and the twist followed an almost linear decreasing trend. Since it was not part of the optimisation, the thickness distribution remained unaffected.

Although the rotational effects were partially taken into account due to RFOIL's convergence issues, the non-dimensional aerodynamic performance obtained with the BEMT approach, i.e. the thrust coefficient is remarkably similar to the reference. On the other hand, the power curve displays a poor performance, resulting from the sub-optimal control strategy since the one employed has been optimised for the DTU 10MW. This fact can be confirmed by the power curve obtained for full-scale during the validation of the integrated design tool, where an almost-perfect match was achieved.

*Validate the aerodynamic performance of the designed wind turbine rotor blade, with the use of an alternative method.*

The thrust-matched blade design selected (geometry No. 3) was assessed in its performance by ReFRESKO 3-D (MARIN's in-house CFD solver) in order to establish the reproducibility of the results obtained by means of the BEMT with RFOIL and FAST. The converged simulations yielded in a close match on the non-dimensional thrust, and as expected, a disagreement in the power outcome, especially for the TSR corresponding to a wind speed beyond rated. This means that BEMT predictions were accurate and that when constructed and implemented in the test setting of a floating foundation, it is likely to obtain similar results if the settings agree with the simulation parameters.

## 7.2 Recommendations for future research

For future design exercises and given the importance of incorporating thoroughly the rotational effects into the aerofoil performance, it would be valuable to employ a CFD 2-D code instead of RFOIL, e.g. ReFRESKO 2-D in order to compute accurately the polars. This is because it was evidenced during the development of the current wind turbine blade that RFOIL faces some convergence issues when it comes to low-Reynolds aerofoils. The downside of this proposal is that the computations become costly. Nevertheless, if this last addition is not feasible, then RFOIL needs to be refined to cope with the aforementioned issues or XFOIL be applied (without the inclusion of rotational effects) with further 3-D flow corrections by using the methods described in this report for this purpose.

Furthermore, an intermediate CFD 3-D thrust and power correction step can be implemented after certain number of iterations in order to keep the cost of the simulations low. This is possible based on the outcomes of the geometry generator, connecting directly to the decision of whether there is a match or not in the non-dimensional coefficients.

For either one of the CFD implementations into the design loop, it is necessary to automate all the CFD-related tools, including pre- and post-processing, such that their outputs can be read and processed by the integrated design tool. This means creating a general code that enables a single set of inputs and that delivers the computed non-dimensional performance

Moreover, in addition to this implementation, the integrated design tool should be able to take the initial aerofoil distribution as input in order to create its own aerofoils. For this purpose, a rigorous aerofoil shape parametrisation algorithm needs to be applied, e.g. with the aid of Bézier curves. This would also mean that there is free optimisation around the thickness.

To the end of improving the BEMT-based results, it is of great importance to incorporate the appropriate control settings (pitch and rotational speed) to be used during the tests while in the design stage. This would render in more accurate performance predictions, and therefore in a more suitable blade shape.

Finally, when the selected blade is constructed and implemented for testing, it would be of great value to compare the aerodynamic performance with the predictions from this work, in order to gain even more trust in the methodology for future designs.

# Bibliography

- [1] DNV GL AS, "Electrifying the future: Third Generation Wind Power," 2016. [Online]. Available: <https://www.dnvgl.com/technology-innovation/broader-view/electrifying-the-future/third-generation-wind-power.html>. [Accessed 20 February 2017].
- [2] GWEC, "Offshore wind power," Global Wind Energy Council, 2017. [Online]. Available: <http://gwec.net/global-figures/global-offshore/>. [Accessed 15 May 2017].
- [3] IRENA, "Innovation Outlook: Offshore Wind," International Renewable Energy Agency, Abu Dhabi, 2016.
- [4] M. C. Holtslag, *Far Offshore Wind Conditions in Scope of Wind Energy*, Delft, The Netherlands: Delft University of Technology, 2016.
- [5] IRENA, "Floating Foundations: A Game Changer for Offshore Wind Power - A Supplement to Innovation Outlook: Offshore Wind (IRENA, 2016)," International Renewable Energy Agency, Abu Dhabi, 2016.
- [6] M. Strach-Sonsalla and M. Muskulus, "Dynamics and Design of Floating Wind Turbines," in *Proceedings of the Twenty-sixth (2016) International Ocean and Polar Engineering Conference*, Rhodes, Greece, 2016.
- [7] E. I. Konstantinidis and P. Botsaris, "Wind turbines: current status, obstacles, trends and technologies," *20th Innovative Manufacturing Engineering and Energy Conference (IManEE)*, no. 161, 2016.
- [8] J. Rhodri and M. Costa Ros, "Floating Offshore Wind: Market & Technology Review - Prepared for the Scottish Government," The Carbon Trust, London, United Kingdom, 2015.
- [9] Offshore WIND, "BNEF: 237MW of Floating Offshore Wind by 2020," 20 March 2017. [Online]. Available: <http://www.offshorewind.biz/2017/03/20/bnef-237mw-of-floating-offshore-wind-by-2020/>. [Accessed 05 July 2017].
- [10] A. Robertson, "Phase II Results of a Floating Semisubmersible Wind System," in *EWEA Offshore Conference*, Frankfurt, Germany, 2013.
- [11] F. M. White, "Dimensional Analysis and Similarity," in *Fluid Mechanics*, New York, McGraw-Hill, 2011, p. 313.
- [12] H. R. Martin, "Development of a Scale Model Wind Turbine for Testing of Offshore Floating Wind Turbine Systems: Civil Engineering M.Sc. Thesis," University of Maine, Orono, Maine, United States, 2011.
- [13] V. Heller, "Model-Prototype Similarity," in *4th CoastLab Teaching School: Wave and Tidal Energy*, Porto, Portugal, 2012.
- [14] S. Martin, S. Day and C. B. Gilmour, "Rotor Scaling Methodologies for Small Scale Testing of Floating Wind Turbine Systems," in *Proceedings of the ASME 2015 34th International Conference on Ocean, Offshore and Arctic Engineering OMAE2015*, St. John's, Newfoundland, Canada, 2015.
- [15] I. Bayati, M. Belloli and L. Bernini, "Qualification of innovative floating substructures for 10MW wind turbines and water depths greater than 50m: Deliverable D3.1 AeroDyn validated model," EU LIFES50+ Project, Milano, Italy, 2016.
- [16] F. Campagnolo, A. E. Koumarios and C. L. Bottasso, "Floating offshore wind turbine testing with non Froude-scaled models," in *EWEA Offshore 2015*, Copenhagen, Denmark, 2015.
- [17] T. Burton, D. Sharpe, N. Jenkins and E. Bossanyi, "Aerodynamics of Horizontal-Axis Wind Turbines," in *Wind Energy Handbook*, Chichester, UK, John Wiley & Sons Ltd, 2001, pp. 41-150.

- [18] J. Manwell, J. McGowan and A. Rogers, "Aerodynamics of Wind Turbines," in *Wind Energy Explained: Theory, Design and Application - Second Edition*, West Sussex, United Kingdom, John Wiley & Sons Ltd., 2009, pp. 91-153.
- [19] S. Schreck, "Wind Turbine Aerodynamics Part B: Turbine Blade Flow Fields," in *Wind Turbine Technology: Fundamental Concepts of Wind Turbine Engineering - Second Edition*, Golden, Colorado, USA, ASME Press, 2009, pp. 351 - 364.
- [20] H. Dumitrescu, C. Vladimir and F. Frunzulica, "An insight into the rotational stall delay," *Proceedings in Applied Mathematics and Mechanics*, vol. 12, pp. 457-458, 2012.
- [21] M. S. Selig, "Low Reynolds Number Airfoil Design: Lecture Notes," Department of Aerospace Engineering - University of Illinois at Urbana-Champaign, Urbana, Illinois, USA, 2003.
- [22] C. Bak, J. Johansen and P. B. Andersen, "Three-Dimensional Corrections of Airfoil Characteristics Based on Pressure Distributions," in *European Wind Energy Conference & Exhibition (EWEC)*, Athens, Greece, 2006.
- [23] W. Timmer, "Aerodynamic characteristics of wind turbine," in *TORQUE: The Science of Making Torque from Wind*, Crete, Greece, 2010.
- [24] A. Bianchini, F. Balduzzi, J. M. Rainbird, J. Peiro, J. M. R. Graham, G. Ferrara and L. Ferrari, "An Experimental and Numerical Assessment of Airfoil Polars for Use in Darrieus Wind Turbines—Part II: Post-stall Data Extrapolation Methods," *Journal of Engineering for Gas Turbines and Power*, vol. 138, 2016.
- [25] D. A. Spera, "Models of Lift and Drag Coefficients of Stalled and Unstalled Airfoils in Wind Turbines and Wind Tunnels," NASA, Cleveland, Ohio, 2008.
- [26] T.-T. Tran and D.-H. Kim, "The platform pitching motion of floating offshore wind turbine: A preliminary unsteady aerodynamic analysis," *Journal of Wind Engineering and Industrial Aerodynamics*, vol. 142, pp. 65-81, 2015.
- [27] D. Matha, "Modelling of Floating Offshore Wind: Aerodynamic Considerations for Floating Wind Turbines," in *Floating Offshore Wind Energy: The Next Generation of Wind Energy*, Hamburg, Germany, Springer, 2016, pp. 141 - 145.
- [28] T. Sebastian and M. Lackner, "Characterization of unsteady aerodynamics of offshore floating wind turbines," in *Wind Energy*, Amherst, Massachusetts, United States, John Wiley & Sons, Ltd., 2012, pp. 339-352.
- [29] D. Matha, F. Wendt, M. Werner and P. W. Cheng, "Aerodynamic Inflow Conditions on Floating Offshore Wind Turbine Blades for Airfoil Design Purposes," in *International Offshore and Polar Engineering Conference*, Rhodes, Greece, 2012.
- [30] J. Jonkman, S. Butterfield, M. Musial and G. Scott, "Definition of a 5-MW Reference Wind Turbine for Offshore System Development," National Renewable Energy Laboratory, Golden, Colorado, United States, 2009.
- [31] C. Bak, R. Bitsche, A. Yde, T. Kim, M. H. Hansen, F. Zahle, M. Gaunaa, J. P. Blasques, M. Døssing, J.-J. W. Heinen and T. Behrens, "Light Rotor: The 10-MW Reference Wind Turbine," DTU Wind Energy | Vestas Wind Systems A/S, Roskilde | Aarhus, Denmark, 2012.
- [32] C. Bak, F. Zahle, R. Bitsche, T. Kim, Y. Anders, L. C. Henriksen, A. Natarajan and M. H. Hansen, "Description of the DTU 10 MW Reference Wind Turbine," Technical University of Denmark, Roskilde, Denmark, 2013.
- [33] B. Buchner, J. Wichers and J. de Wilde, "Features of the State-of-the-art Deepwater Offshore Basin," Offshore Technology Conference, Houston, Texas, United States, 1999.
- [34] UIUC Applied Aerodynamics Group, Department of Aerospace Engineering, University of Illinois at Urbana-Champaign, "UIUC Airfoil Coordinates Database," 2017. [Online]. Available: [http://m-selig.ae.illinois.edu/ads/coord\\_database.html](http://m-selig.ae.illinois.edu/ads/coord_database.html). [Accessed 10 February 2017].

- [35] H. R. Martin, R. W. Kimball, A. M. Viselli and A. J. Goupee, "Methodology for Wind/Wave Basin Testing of Floating Offshore Wind Turbines," *Journal of Offshore Mechanics and Arctic Engineering*, vol. 136, 2014.
- [36] M. J. Fowler, R. W. Kimball, D. A. Thomas (III) and A. J. Goupee, "Design and Testing of Scale Model Wind Turbines for Use in Wind/Wave Basin Model Tests of Floating Offshore Wind Turbines," in *ASME 32nd International Conference on Ocean, Offshore and Arctic Engineering*, Nantes, France, 2013.
- [37] P. J. Moriarty and A. C. Hansen, "AeroDyn Theory Manual," National Renewable Energy Laboratory, Golden, Colorado | Salt Lake City, Utah - USA, 2005.
- [38] J. M. Jonkman and M. L. J. Buhl, "FAST User's Guide," National Renewable Energy Laboratory, Golden, Colorado, 2005.
- [39] E.-J. de Ridder, W. Otto, G.-J. Zondervan, F. Huijs and G. Vaz, "Development of a Scaled-down Floating Wind Turbine for Offshore Basin Testing," in *ASME 2014 33rd International Conference on Ocean, Offshore and Arctic Engineering*, San Francisco, California, USA, 2014.
- [40] M. Drela, "XFOIL: An Analysis and Design System for Low Reynolds Number Airfoils," in *Conference on Low Reynolds Number Airfoil Aerodynamics*, University of Notre Dame, 1989.
- [41] Department of Aerospace Engineering, UIUC Applied Aerodynamics Group, "PropID for Horizontal Axis Wind Turbines," 2017. [Online]. Available: <http://m-selig.ae.illinois.edu/propid.html>. [Accessed 20 February 2017].
- [42] MARIN, "ReFRESCO," 2017. [Online]. Available: <http://www.refresco.org/>. [Accessed 10 March 2017].
- [43] R. Kimball, A. J. Goupee, M. J. Fowler, E.-J. de Ridder and J. Helder, "Wind/Wave Basin Verification of a Performance-Matched Scale-model Wind Turbine on a Floating Offshore Wind Turbine Platform," in *ASME 2014 33rd International Conference on Ocean, Offshore and Arctic Engineering*, San Francisco, California, USA, 2014.
- [44] European Union's Seventh Framework Programme, "INNWIND.EU (Innovative Wind Conversion Systems (10-20MW) For Offshore Applications)," 2017. [Online]. Available: <http://www.innwind.eu/>. [Accessed 02 March 2017].
- [45] CENER; SWE; DNV-GL; DTU; PoliMi, "Description of Floating Wind Model Tests at ECN and DHI - Deliverable 4.2.4: Results of wave tank tests - INNWIND.EU Programme," DTU Wind, 2016.
- [46] M. S. Selig, J. J. Guglielmo, A. P. Broeren and P. Giguere, "Summary of Low-Speed Airfoil Data: Volume 1," SoarTech Publications, Virginia Beach, Virginia, USA, 1995.
- [47] I. Bayati, M. Belloli, L. Bernini and A. Zasso, "Aerodynamic design methodology for wind tunnel tests of wind turbine rotors," *Journal of Wind Engineering & Industrial Aerodynamics*, vol. 167, pp. 217-227, 2017.
- [48] C. A. Lyon, A. P. Broeren, P. Giguere, A. Gopalathnam and M. S. Selig, "Summary of Low-Speed Airfoil Data: Volume 3," SoarTech Publications, Virginia Beach, Virginia, USA, 1997.
- [49] R. Mikkelsen, "The DTU 10MW 1:60 model scale wind turbine blade," DTU Wind, Lyngby, Denmark, 2015.
- [50] H. Bredmose, R. Mikkelsen, A. M. Hansen, R. Laugesen, N. Heilskov, B. Jensen and J. Kirkegaard, "Experimental study of the DTU 10 MW wind turbine on a TLP floater in waves and wind," in *EWEA Offshore 2015 Conference*, Copenhagen, Denmark, 2015.
- [51] M. J. Fowler, A. J. Goupee and A. M. Viselli, "Advances in Model Scale Testing of Floating Offshore Wind Turbines Utilizing the W<sup>2</sup> Wind/Wave Basin," in *Offshore Technology Conference*, Houston, Texas, USA, 2016.
- [52] J. Helder and M. Pietersma, "UMaine – DeepCWind/OC4 Semi Floating Wind Turbine Repeat Tests," MARIN, Wageningen, The Netherlands, 2013.

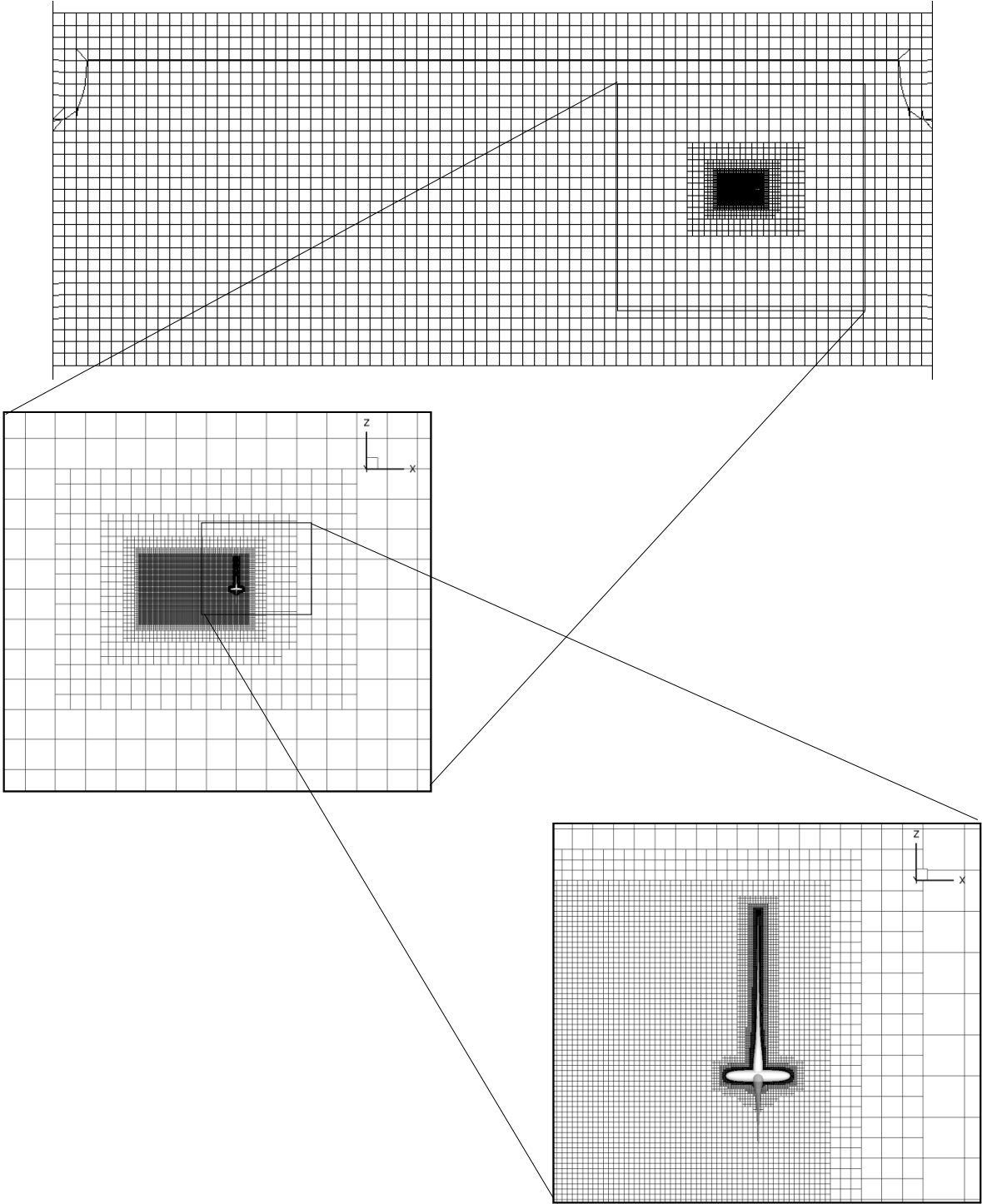
- [53] IDEOL, “Modelling of wind turbines for model testing,” La Ciotat, France, 2017.
- [54] J. Azcona, F. Bouchotrouch, M. González, J. Garciandía, X. Munduate, F. Kelberlau and T. A. Nygaard, “Aerodynamic Thrust Modelling in Wave Tank Tests of Offshore Floating Wind Turbines Using a Ducted Fan,” *Journal of Physics: Conference Series 524*, vol. The Science of Making Torque from Wind, 2014.
- [55] CENER, “Ocean basin tests,” Navarra, Spain, 2017.
- [56] A. Jurado, J. Sarmiento, J. A. Armesto, A. Meseguer, R. Guanche, B. Couñago, J. Urbano and J. Serna, “Experimental Modelling and Numerical Model Calibration of Telwind: An Innovative Floating Wind Offshore Concept,” in *Marine Energy Week*, Bilbao, Spain, 2017.
- [57] E.-J. de Ridder, *Winch-controlled testing model*, Wageningen, The Netherlands: MARIN, 2017.
- [58] W. Du, Y. Zhao, M. Wang, Y. He and R. Jiang, “Design and Analysis of a Model Wind Turbine Blade for Wave Basin Test of Floating Wind Turbines,” in *International Offshore and Polar Engineering*, Anchorage, Alaska, USA, 2013.
- [59] B. Montgomerie, A. Brand, J. Bosschiers and R. van Rooij, *Three-Dimensional Effects in Stall*, Petten, The Netherlands: ECN, 1997.
- [60] C. Bak, F. Zahle, R. Bitsche and T. Kim, “The DTU 10MW Reference Wind Turbine Project Site,” DTU Wind Energy, 2013. [Online]. Available: <https://dtu-10mw-rwt.vindenergi.dtu.dk/projects>. [Accessed 03 April 2017].
- [61] J. Jonkman, “FAST,” National Wind Turbine Center Information Portal, 19 March 2015. [Online]. Available: <https://nwtc.nrel.gov/FAST>. [Accessed 27 May 2017].
- [62] A. Cordle and J. Jonkman, “State of the Art in Floating Wind Turbine Design Tools,” in *International Offshore and Polar Engineering Conference*, Maui, Hawaii, USA, 2011.
- [63] T. W. Sederberg, “Bézier Curves,” in *Computer Aided Geometric Design Course Notes*, Brigham, UK, Brigham Young University, 2014, pp. 17-.
- [64] K. Deb, A. Pratap, S. Agarwal and T. Meyarivan, “A Fast and Elitist Multiobjective Genetic Algorithm:,” *IEEE Transactions on Evolutionary Computation*, vol. 6, no. 2, pp. 182-197, 2002.
- [65] Robert McNeel & Associates, “Rhino 5 Features,” 2017. [Online]. Available: [www.rhino3d.com](http://www.rhino3d.com). [Accessed 20 May 2017].
- [66] S. Jongsma, “Shape Parametrization,” in *On a Method for Simulation-Based Wind Turbine Blade Design*, Enschede, The Netherlands, University of Twente, 2014, pp. 17-31.
- [67] S. Davidson, “Grasshopper: Algorithmic Modeling for Rhino,” NING, 2017. [Online]. Available: [www.grasshopper3d.com](http://www.grasshopper3d.com). [Accessed 14 August 2017].
- [68] NUMECA International, “HEXPRESS™,” 2016. [Online]. Available: <http://www.numeca.be/product/hexpress>. [Accessed 20 February 2017].
- [69] S. Burmester, S. Gueydon and M. Make, “Determination of Scaled Wind Turbine Rotor Characteristics from Three Dimensional RANS,” *TORQUE: The Science of Making Torque from Wind*, no. 753, 2016.
- [70] M. Make, “Predicting scale effects on floating offshore wind turbines: A numerical analysis of model- and full-scale wind turbines using a RANS CFD solver,” TU Delft, Delft, The Netherlands, 2014.
- [71] CFD Online, “Dimensionless wall distance (y plus),” 28 March 2014. [Online]. Available: [https://www.cfd-online.com/Wiki/Dimensionless\\_wall\\_distance\\_\(y\\_plus\)](https://www.cfd-online.com/Wiki/Dimensionless_wall_distance_(y_plus)). [Accessed 10 August 2017].
- [72] Kiteware, “Paraview,” 2017. [Online]. Available: <https://www.paraview.org/>. [Accessed 20 March 2017].

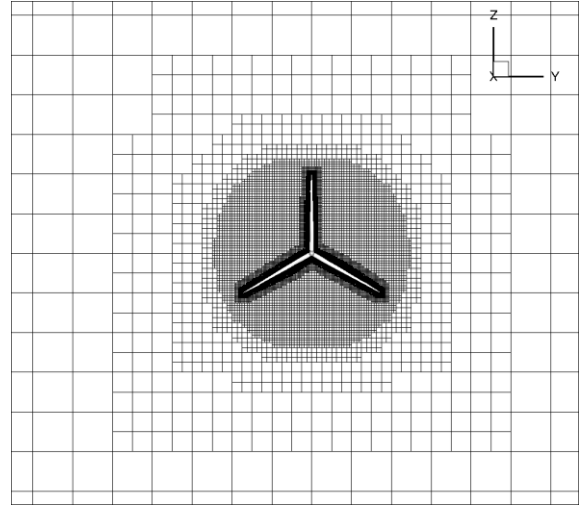
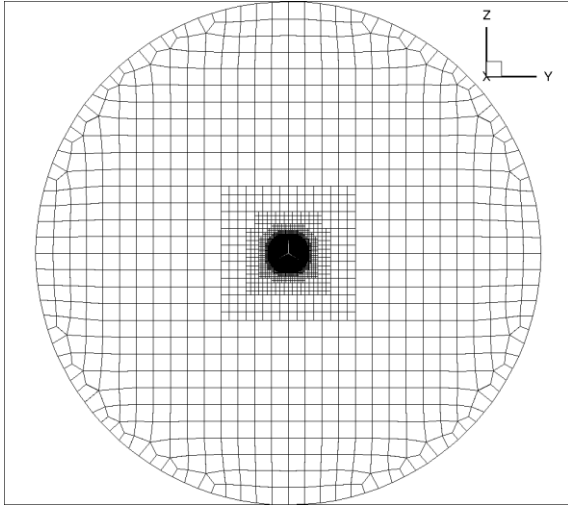
- [73] Tecplot, "Tecplot 360," 2017. [Online]. Available: <http://www.tecplot.com/products/tecplot-360/>. [Accessed 20 August 2017].
- [74] M. S. Selig, C. A. Lyon, P. Giguere, C. P. Ninham and J. J. Guglielmo, "Summary of Low-Speed Airfoil Data: Summary of Low-Speed Airfoil Dataolome 2," Soartech Publications, Virginia Beach, Virginia, USA, 1996.
- [75] M. M. Selig and B. D. McGranahan, "Wind Tunnel Aerodynamic Tests of Six Airfoils for Use on Small Wind Turbines," National Renewable Energy Laboratory, Golden, Colorado, USA, 2003.
- [76] D. Wood, "Aerofoils: Lift, Drag, and Circulation," in *Small Wind Turbines: Analysis, Design and Application*, Calgary, Alberta, Canada, Springer: Green Energy and Technology, 2011, pp. 57-59.
- [77] Airfoil Tools, "Airfoil database," 2017. [Online]. Available: <http://airfoiltools.com/>. [Accessed 10 May 2017].
- [78] P. K. Kundu, I. M. Cohen and D. R. Dowling, "Turbulence," in *Fluid Mechanics: 5th Edition*, Waltham, Massachusetts, USA, Elsevier, 2012, pp. 542-543.
- [79] M. Drela, "XFOIL 6.9 User Primer," 30 November 2001. [Online]. Available: [http://web.mit.edu/drela/Public/web/xfoil/xfoil\\_doc.txt](http://web.mit.edu/drela/Public/web/xfoil/xfoil_doc.txt). [Accessed 15 February 2017].
- [80] G. Vaz, "Refresco for Floating Wind and Current Turbines," MARIN, Wageningen, The Netherlands, 2014.
- [81] MARIN, "ReFRESCO Documentation - Tutorials: Version 2.3.0," Wageningen, The Netherlands, 2017.

# Appendix A Figures Full-Scale CFD Pre- & Post-processing

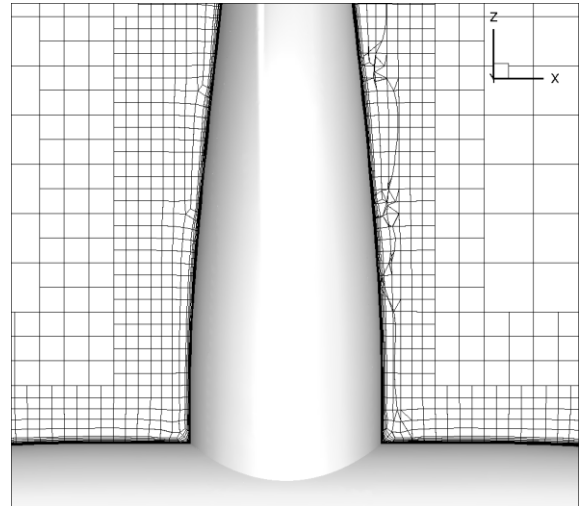
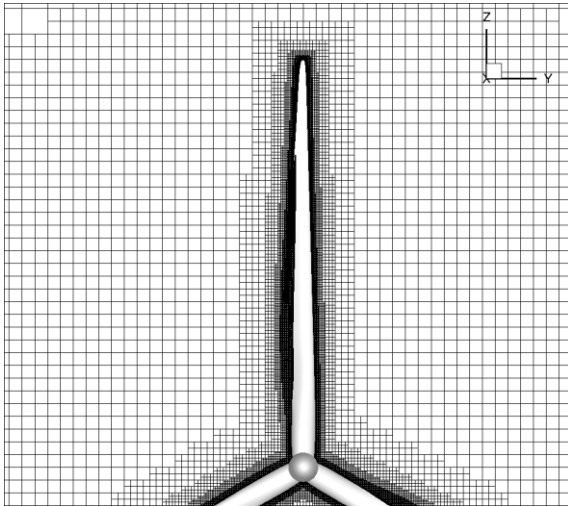
## Preprocessing with HEXPRESS

*Meshing of the Domain and Viscous Layer*



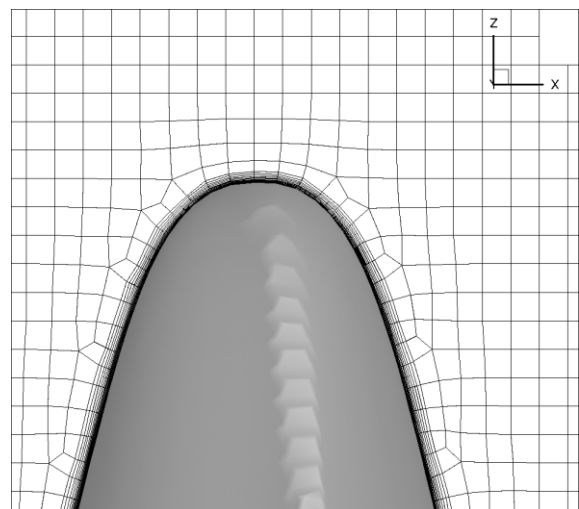
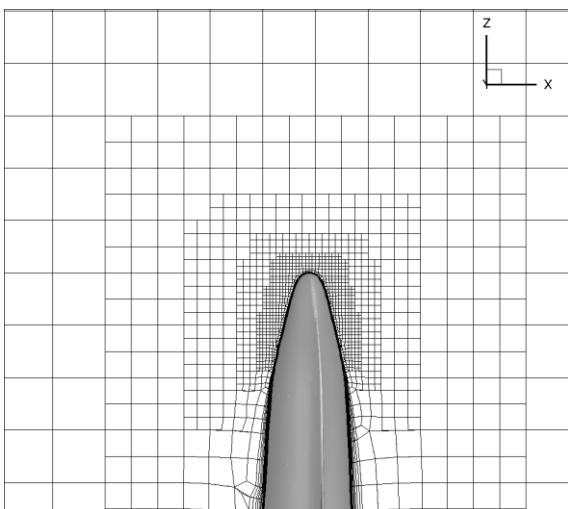


a. Front view computational domain



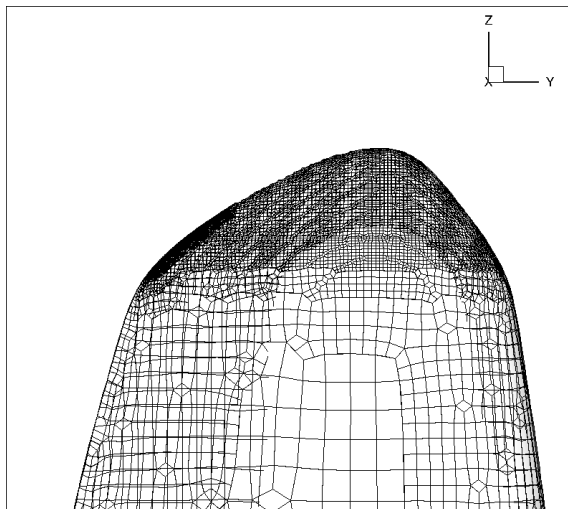
b. Front view meshing around rotor assembled

c. Closeup trailing edge inboards

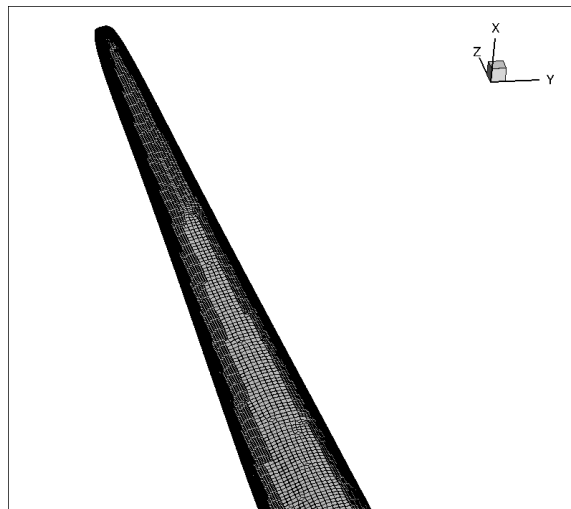


d. Trailing Edge at Blade tip

## Meshing of the Blades



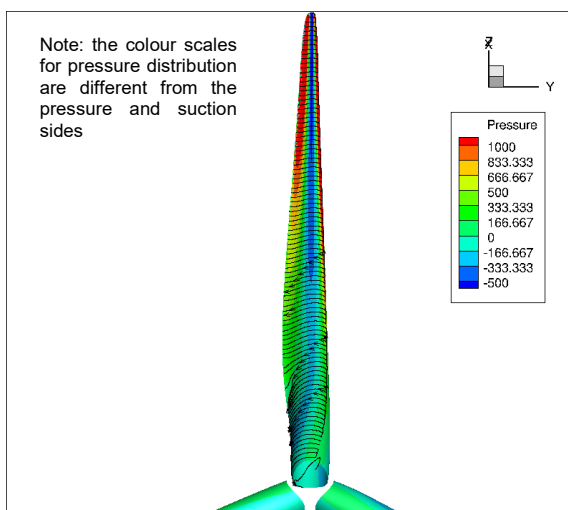
a. Blade tip



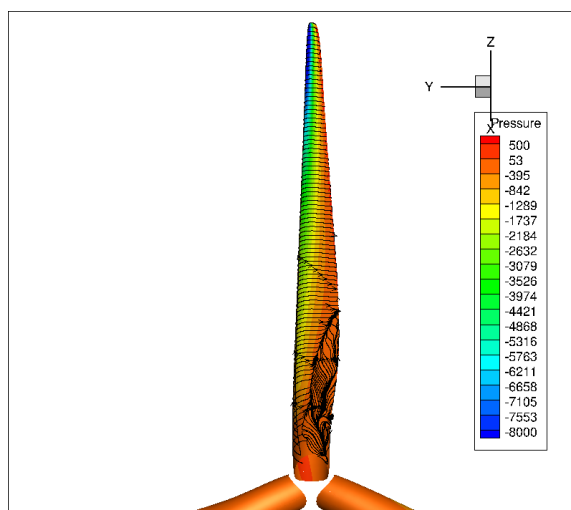
b. Blade mid- and outboard

## Post-processing with Tecplot

### Flow over pressure and suction sides

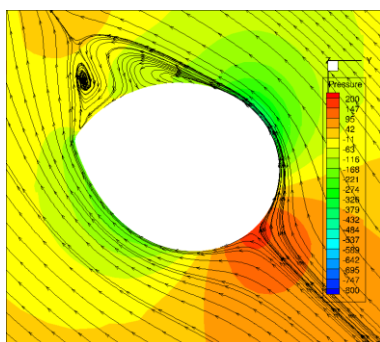


a. Pressure side

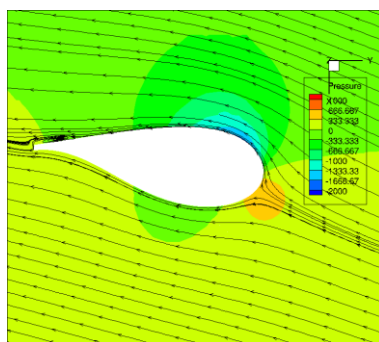


b. Suction side

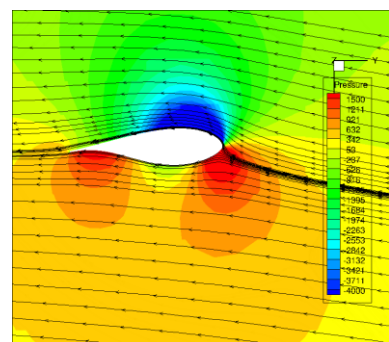
### Flow over the blade at specific stations



$r = 12 \text{ m}$



$r = 30 \text{ m}$



$r = 80 \text{ m}$

# Appendix B FAST Inputs Optimisation

Type / unit	Variables	Original									Optimal
Turbine Configuration	Onshore	X	X	X	X	X	X	X	X	X	X
Timestep [s]	Simulation time	400	400	400	400	400	400	400	400	400	10
	DT_glue	0.0125	0.05	0.1	0.1	0.1	0.1	0.1	0.1	0.1	0.1
	DT_ElastoDyn	0.0025	0.0025	0.0025	0.01	0.01	0.01	0.01	0.01	0.01	0.01
	Tout	0.0125	0.05	0.1	0.1	0.1	0.1	0.1	0.1	0.1	0.1
Blade Discretisation	37	X	X	X	X						
	17					X					
	12						X	X	X	X	X
Blades Flexibility	Elastic	X	X	X	X	X	X				
	Rigid							X	X	X	X
Tower Flexibility	Elastic	X	X	X	X	X	X	X			
	Rigid								X	X	X
Controller	Active	X	X	X	X	X	X	X	X		
	Imposed Pitch & RPM									X	X
Results											
[min]	Simulation time FAST rated	4.164	3.747	3.582	0.909	0.585	0.486	0.480	0.440	0.414	0.012
[RPM]	Rotational Speed	9.600	9.602	9.625	9.625	9.638	9.633	9.623	9.622	9.600	9.600
[kN]	Thrust	1,608	1,608	1,616	1,616	1,670	1,652	1,605	1,576	1,569	1,570
[kW]	Power	10,420	10,420	10,444	10,444	10,457	10,452	10,442	10,441	10,417	10,416
[kNm]	Torque	10,360	10,360	10,360	10,360	10,360	10,360	10,360	10,360	10,362	10,363
[-]	TSR	7.863	7.865	7.884	7.884	7.894	7.890	7.882	7.881	7.863	7.863
[-]	Ct	0.809	0.809	0.813	0.813	0.840	0.831	0.807	0.793	0.790	0.790
[-]	Cp	0.460	0.460	0.461	0.461	0.462	0.461	0.461	0.461	0.460	0.460

# Appendix C RFOIL Actions

```
LOAD
$airfoil_name$.dat
$aerofoil_name$
OPER
VPAR
N
9
f
$dimensionless free-stream velocity$
cr
$local solidity $
vacc
0
XTR
1.0000
1.0000

VISC
$Reynolds number$
MACH
0.0
ALFA
0.0000
INIT
PACC
$airfoil_name$_polar.txt

ALFA
-10
ALFA
-8
ALFA
-6
ALFA
-4
ALFA
-2
ALFA
0
ALFA
2
ALFA
4
ALFA
6
ALFA
8
ALFA
10
... Continues in the next column
```

```
...
ALFA
12
ALFA
14
ALFA
16
ALFA
18
ALFA
20
PACC

QUIT
```

# Appendix D FAST Input Files

## FAST v8.12 General Input File

```
----- FAST v8.12.* INPUT FILE -----
FAST model of the DTU 10MW Reference Wind Turbine, onshore version 1.00
----- SIMULATION CONTROL -----
False Echo - Echo input data to <RootName>.ech (flag)
"FATAL" AbortLevel - Error level when simulation should abort (string) {"WARNING", "SEVERE",
"FATAL"}
10 TMax - Total run time (s)
0.1 DT - Recommended module time step (s)
1 InterpOrder - Interpolation order for input/output time history (-) {1=linear, 2=quadratic}
0 NumCrctn - Number of correction iterations (-) {0=explicit calculation, i.e. no corrections}
999999 DT_UJac - Time between calls to get Jacobians (s)
1E+06 UJacScfFact - Scaling factor used in Jacobians (-)
----- FEATURE SWITCHES AND FLAGS -----
1 CompElast - Compute structural dynamics (switch) {1=ElastoDyn; 2=ElastoDyn + BeamDyn for
blades}
1 CompInflow - Compute inflow wind velocities (switch) {0=still air; 1=InflowWind; 2=external from
OpenFOAM}
1 CompAero - Compute aerodynamic loads (switch) {0=None; 1=AeroDyn v14; 2=AeroDyn v15}
0 CompServo - Compute control and electrical-drive dynamics (switch) {0=None; 1=ServoDyn}
0 CompHydro - Compute hydrodynamic loads (switch) {0=None; 1=HydroDyn}
0 CompSub - Compute sub-structural dynamics (switch) {0=None; 1=SubDyn}
0 CompMooring - Compute mooring system (switch) {0=None; 1=MAP++; 2=FEAMooring; 3=MoorDyn;
4=OrcaFlex}
0 CompIce - Compute ice loads (switch) {0=None; 1=IceFloe; 2=IceDyn}
----- INPUT FILES -----
"10MWRWT\DTU_10MW_RWT_ElastoDyn_11.4.dat" EDFFile - Name of file containing ElastoDyn input
parameters (quoted string)
"unused" BDBldFile(1) - Name of file containing BeamDyn input parameters for blade 1 (quoted string)
"unused" BDBldFile(2) - Name of file containing BeamDyn input parameters for blade 2 (quoted string)
"unused" BDBldFile(3) - Name of file containing BeamDyn input parameters for blade 3 (quoted string)
"10MWRWT\DTU_10MW_InflowWind_11.4.dat" InflowFile - Name of file containing inflow wind input
parameters (quoted string)
"10MWRWT\DTU_10MW_RWT_AeroDyn.dat" AeroFile - Name of file containing aerodynamic input
parameters (quoted string)
"unused" ServoFile - Name of file containing control and electrical-drive input parameters (quoted string)
"unused" HydroFile - Name of file containing hydrodynamic input parameters (quoted string)
"unused" SubFile - Name of file containing sub-structural input parameters (quoted string)
"unused" MooringFile - Name of file containing mooring system input parameters (quoted string)
"unused" IceFile - Name of file containing ice input parameters (quoted string)
----- OUTPUT -----
True SumPrint - Print summary data to "<RootName>.sum" (flag)
2 StsTime - Amount of time between screen status messages (s)
99999 ChkptTime - Amount of time between creating checkpoint files for potential restart (s)
0.1 DT_Out - Time step for tabular output (s)
0 TStart - Time to begin tabular output (s)
1 OutFileFmt - Format for tabular (time-marching) output file (switch) {1: text file [<RootName>.out], 2:
binary file [<RootName>.outb], 3: both}
True TabDelim - Use tab delimiters in text tabular output file? (flag) {uses spaces if false}
"ES10.3E2" OutFmt - Format used for text tabular output, excluding the time channel. Resulting field
should be 10 characters. (quoted string)
```

## FAST AeroDyn v.14.04 Input File

```
----- AeroDyn v14.04.* INPUT FILE -----
DTU 10.0 MW onshore baseline aerodynamic input properties;Compatible with AeroDyn v14
BEDDOES StallMod - Dynamic stall included [BEDDOES or STEADY] (unquoted string)
USE_CM UseCm - Use aerodynamic pitching moment model? [USE_CM or NO_CM] (unquoted string)
EQUIL InfModel - Inflow model [DYNIN or EQUIL] (unquoted string)
SWIRL IndModel - Induction-factor model [NONE or WAKE or SWIRL] (unquoted string)
0.005 AToler - Induction-factor tolerance (convergence criteria) (-)
PRANDtl TLModel - Tip-loss model (EQUIL only) [PRANDtl, GTECH, or NONE] (unquoted string)
PRANDtl HLMModel - Hub-loss model (EQUIL only) [PRANDtl or NONE] (unquoted string)
"NEWTOWER" TwrShad - INSTEAD OF: 0.0 TwrShad - Tower-shadow velocity deficit (-)
False TwrPotent - Calculate tower potential flow (flag) INSTEAD OF 9999.9 ShadHWid - Tower-shadow
half width (m)
False TwrShadow - Calculate tower shadow (flag) INSTEAD OF 9999.9 T_Shad_Refpt- Tower-shadow
reference point (m)
"unused" TwrFile - Tower drag file name (quoted string)
False CalcTwrAero - Calculate aerodynamic drag of the tower at the ElastoDyn nodes. TwrPotent must
be true.
1.225 AirDens - Air density (kg/m^3)
1.464E-5 KinVisc - Kinematic air viscosity [CURRENTLY IGNORED] (m^2/sec)
default DTAero - Time interval for aerodynamic calculations (sec) !bjj: was 0.02479
12 NumFoil - Number of airfoil files (-)
"AeroData\Cylinder.dat" FoilNm - Names of the airfoil files [NumFoil lines] (quoted strings)
"AeroData\Cylinder.dat"
"AeroData\11_100geo_100gen_aero_MS_00011_014_001_r3_FAST.dat"
"AeroData\11_100geo_100gen_aero_MS_00011_014_001_r4_FAST.dat"
"AeroData\11_100geo_100gen_aero_MS_00011_014_001_r5_FAST.dat"
"AeroData\11_100geo_100gen_aero_MS_00011_014_001_r6_FAST.dat"
"AeroData\11_100geo_100gen_aero_MS_00011_014_001_r7_FAST.dat"
"AeroData\11_100geo_100gen_aero_MS_00011_014_001_r8_FAST.dat"
"AeroData\11_100geo_100gen_aero_MS_00011_014_001_r9_FAST.dat"
"AeroData\11_100geo_100gen_aero_MS_00011_014_001_r10_FAST.dat"
"AeroData\11_100geo_100gen_aero_MS_00011_014_001_r11_FAST.dat"
"AeroData\11_100geo_100gen_aero_MS_00011_014_001_r12_FAST.dat"
12 BldNodes
RNodes AeroTwst DRNodes Chord NFoil PrnElm
6.400 13.590 7.200 5.476 1 NOPRINT
13.600 12.188 7.200 6.462 2 NOPRINT
20.800 10.784 7.200 8.989 3 NOPRINT
28.000 9.375 7.200 9.330 4 NOPRINT
35.200 7.954 7.200 8.586 5 NOPRINT
42.400 6.511 7.200 7.501 6 NOPRINT
49.600 5.037 7.200 6.344 7 NOPRINT
56.800 3.524 7.200 5.210 8 NOPRINT
64.000 1.982 7.200 4.163 9 NOPRINT
71.200 0.421 7.200 3.275 10 NOPRINT
78.400 -1.149 7.200 2.528 11 NOPRINT
85.600 -2.723 7.200 1.734 12 NOPRINT
```

## FAST Aerofoil Input File

```
11_100geo_30gen_aero_MS_00011_014_001_r7 at radii 0.55627
1
0.0
12.00 Stall angle (deg)
0 No longer used
0 No longer used
0 No longer used
-4.0302 Zero Cn angle of attack (deg)
6.6166 Cn slope for zero lift (dimensionless)
1.8512 Cn extrapolated to value at positive stall angle of attack
-0.8000 Cn at stall value for negative angle of attack
8.00 Angle of attack for minimum CD (deg)
0.0285 Minimum CD value
-180.00 0.000 0.0266 0.0000
-170.00 0.490 0.0651 0.4000
-160.00 0.834 0.1759 0.5275
-150.00 0.707 0.3455 0.4283
-140.00 0.637 0.5534 0.4118
-130.00 0.558 0.7741 0.4207
-120.00 0.452 0.9808 0.4359
-110.00 0.316 1.1482 0.4472
-100.00 0.161 1.2557 0.4482
-90.00 0.000 1.2900 0.4349
-80.00 -0.161 1.2557 0.4089
-70.00 -0.316 1.1482 0.3712
-60.00 -0.452 0.9808 0.3266
-50.00 -0.558 0.7741 0.2801
-40.00 -0.637 0.5534 0.2349
-30.00 -0.707 0.3455 0.1890
-20.00 -0.834 0.1759 0.1194
-10.00 -0.409 0.1302 -0.0301
-8.00 -0.406 0.1073 -0.0348
-6.00 -0.275 0.0617 -0.0899
-2.00 0.236 0.0316 -0.1317
4.00 0.927 0.0315 -0.1366
6.00 1.137 0.0298 -0.1277
8.00 1.314 0.0285 -0.1104
10.00 1.383 0.0382 -0.0877
12.00 1.444 0.0518 -0.0716
18.00 1.260 0.1485 -0.0865
20.00 1.192 0.1759 -0.1221
30.00 1.010 0.3455 -0.2146
40.00 0.910 0.5534 -0.2652
50.00 0.798 0.7741 -0.3072
60.00 0.645 0.9808 -0.3459
70.00 0.452 1.1482 -0.3813
80.00 0.230 1.2557 -0.4117
90.00 0.000 1.2900 -0.4349
100.00 -0.161 1.2557 -0.4482
110.00 -0.316 1.1482 -0.4472
120.00 -0.452 0.9808 -0.4359
130.00 -0.558 0.7741 -0.4207
140.00 -0.637 0.5534 -0.4118
150.00 -0.707 0.3455 -0.4283
160.00 -0.834 0.1759 -0.5275
170.00 -0.490 0.0651 -0.5000
180.00 0.000 0.0266 0.0000
```

## FAST ElastoDyn Input File

```
----- ELASTODYN V1.01.* INPUT FILE -----
FAST model of the DTU 10MW Reference Wind Turbine, onshore version 0.1
----- SIMULATION CONTROL -----
False Echo - Echo input data to "<RootName>.ech" (flag)
3 Method - Integration method: {1: RK4, 2: AB4, or 3: ABM4} (-)
0.01 DT - Integration time step (s)
----- ENVIRONMENTAL CONDITION -----
9.80665 Gravity - Gravitational acceleration (m/s^2)
----- DEGREES OF FREEDOM -----
False FlapDOF1 - First flapwise blade mode DOF (flag)
False FlapDOF2 - Second flapwise blade mode DOF (flag)
False EdgeDOF - First edgewise blade mode DOF (flag)
False TeetDOF - Rotor-teeter DOF (flag) [unused for 3 blades]
False DrTrDOF - Drivetrain rotational-flexibility DOF (flag)
False GenDOF - Generator DOF (flag)
False YawDOF - Yaw DOF (flag)
False TwFADOF1 - First fore-aft tower bending-mode DOF (flag)
False TwFADOF2 - Second fore-aft tower bending-mode DOF (flag)
False TwSSDOF1 - First side-to-side tower bending-mode DOF (flag)
False TwSSDOF2 - Second side-to-side tower bending-mode DOF (flag)
False PtfmSgDOF - Platform horizontal surge translation DOF (flag)
False PtfmSwDOF - Platform horizontal sway translation DOF (flag)
False PtfmHvDOF - Platform vertical heave translation DOF (flag)
False PtfmRDOF - Platform roll tilt rotation DOF (flag)
False PtfmPDOF - Platform pitch tilt rotation DOF (flag)
False PtfmYDOF - Platform yaw rotation DOF (flag)
----- INITIAL CONDITIONS -----
0 OoPDefl - Initial out-of-plane blade-tip displacement (meters)
0 IPDefl - Initial in-plane blade-tip deflection (meters)
2.63 BIPitch(1) - Blade 1 initial pitch (degrees)
2.63 BIPitch(2) - Blade 2 initial pitch (degrees)
2.63 BIPitch(3) - Blade 3 initial pitch (degrees) [unused for 2 blades]
0 TeetDefl - Initial or fixed teeter angle (degrees) [unused for 3 blades]
0 Azimuth - Initial azimuth angle for blade 1 (degrees)
9.6 RotSpeed - Initial or fixed rotor speed (rpm)
0 NacYaw - Initial or fixed nacelle-yaw angle (degrees)
0 TTDspFA - Initial fore-aft tower-top displacement (meters)
0 TTDspSS - Initial side-to-side tower-top displacement (meters)
0 PtfmSurge - Initial or fixed horizontal surge translational displacement of platform (meters)
0 PtfmSway - Initial or fixed horizontal sway translational displacement of platform (meters)
0 PtfmHeave - Initial or fixed vertical heave translational displacement of platform (meters)
0 PtfmRoll - Initial or fixed roll tilt rotational displacement of platform (degrees)
0 PtfmPitch - Initial or fixed pitch tilt rotational displacement of platform (degrees)
0 PtfmYaw - Initial or fixed yaw rotational displacement of platform (degrees)
----- TURBINE CONFIGURATION -----
3 NumBl - Number of blades (-)
89.2 TipRad - The distance from the rotor apex to the blade tip (meters)
2.8 HubRad - The distance from the rotor apex to the blade root (meters)
0 PreCone(1) - Blade 1 cone angle (degrees)
0 PreCone(2) - Blade 2 cone angle (degrees)
0 PreCone(3) - Blade 3 cone angle (degrees) [unused for 2 blades]
0.0 HubCM - Distance from rotor apex to hub mass [positive downwind] (meters)
0.0 UndSling - Undersling length [distance from teeter pin to the rotor apex] (meters) [unused for 3 blades]
0 Delta3 - Delta-3 angle for teetering rotors (degrees) [unused for 3 blades]
0 AzimB1Up - Azimuth value to use for I/O when blade 1 points up (degrees)
-7.1 OverHang - Distance from yaw axis to rotor apex [3 blades] or teeter pin [2 blades] (meters)
```

3.55 ShftGagL - Distance from rotor apex [3 blades] or teeter pin [2 blades] to shaft strain gages [positive for upwind rotors] (meters)

0 ShftTilt - Rotor shaft tilt angle (degrees)

2.687 NacCMxn - Downwind distance from the tower-top to the nacelle CM (meters)

0 NacCMyn - Lateral distance from the tower-top to the nacelle CM (meters)

2.45 NacCMzn - Vertical distance from the tower-top to the nacelle CM (meters)

-3.09528 NclMUxn - Downwind distance from the tower-top to the nacelle IMU (meters)

0 NclMUyn - Lateral distance from the tower-top to the nacelle IMU (meters)

2.23336 NclMUzn - Vertical distance from the tower-top to the nacelle IMU (meters)

2.75 Twr2Shft - Vertical distance from the tower-top to the rotor shaft (meters)

115.63 TowerHt - Height of tower above ground level [onshore] or MSL [offshore] (meters)

0 TowerBsHt - Height of tower base above ground level [onshore] or MSL [offshore] (meters)

0 PtfmCMxt - Downwind distance from the ground level [onshore] or MSL [offshore] to the platform CM (meters)

0 PtfmCMyt - Lateral distance from the ground level [onshore] or MSL [offshore] to the platform CM (meters)

0 PtfmCMzt - Vertical distance from the ground level [onshore] or MSL [offshore] to the platform CM (meters)

0 PtfmRefzt - Vertical distance from the ground level [onshore] or MSL [offshore] to the platform reference point (meters)

----- MASS AND INERTIA -----

0 TipMass(1) - Tip-brake mass, blade 1 (kg)

0 TipMass(2) - Tip-brake mass, blade 2 (kg)

0 TipMass(3) - Tip-brake mass, blade 3 (kg) [unused for 2 blades]

105.520E3 HubMass - Hub mass (kg)

325.6709E3 HubIner - Hub inertia about rotor axis [3 blades] or teeter axis [2 blades] (kg m<sup>2</sup>)

1500.5 GenIner - Generator inertia about HSS (kg m<sup>2</sup>)

446.03625E3 NacMass - Nacelle mass (kg)

7326.34645E3 NacYIner - Nacelle inertia about yaw axis (kg m<sup>2</sup>)

0 YawBrMass - Yaw bearing mass (kg)

0 PtfmMass - Platform mass (kg)

0 PtfmRIner - Platform inertia for roll tilt rotation about the platform CM (kg m<sup>2</sup>)

0 PtfmPIner - Platform inertia for pitch tilt rotation about the platform CM (kg m<sup>2</sup>)

0 PtfmYIner - Platform inertia for yaw rotation about the platform CM (kg m<sup>2</sup>)

----- BLADE -----

51 BldNodes - Number of blade nodes (per blade) used for analysis (-)

"DTU\_10MW\_ElastoDyn\_Blades.dat" BldFile(1) - Name of file containing properties for blade 1 (quoted string)

"DTU\_10MW\_ElastoDyn\_Blades.dat" BldFile(2) - Name of file containing properties for blade 2 (quoted string)

"DTU\_10MW\_ElastoDyn\_Blades.dat" BldFile(3) - Name of file containing properties for blade 3 (quoted string) [unused for 2 blades]

----- ROTOR-TEETER -----

0 TeetMod - Rotor-teeter spring/damper model {0: none, 1: standard, 2: user-defined from routine UserTeet} (switch) [unused for 3 blades]

0 TeetDmpP - Rotor-teeter damper position (degrees) [used only for 2 blades and when TeetMod=1]

0 TeetDmp - Rotor-teeter damping constant (N-m/(rad/s)) [used only for 2 blades and when TeetMod=1]

0 TeetCDmp - Rotor-teeter rate-independent Coulomb-damping moment (N-m) [used only for 2 blades and when TeetMod=1]

0 TeetSSStP - Rotor-teeter soft-stop position (degrees) [used only for 2 blades and when TeetMod=1]

0 TeetHStP - Rotor-teeter hard-stop position (degrees) [used only for 2 blades and when TeetMod=1]

0 TeetSSSp - Rotor-teeter soft-stop linear-spring constant (N-m/rad) [used only for 2 blades and when TeetMod=1]

0 TeetHSSp - Rotor-teeter hard-stop linear-spring constant (N-m/rad) [used only for 2 blades and when TeetMod=1]

----- DRIVETRAIN -----

100 GBoxEff - Gearbox efficiency (%)

50.0 GBRatio - Gearbox ratio (-)

2.317025E9 DTTorSpr - Drivetrain torsional spring (N-m/rad)

9240560 DTTorDmp - Drivetrain torsional damper (N-m/(rad/s))

----- FURLING -----

False Furling - Read in additional model properties for furling turbine (flag) [must currently be FALSE]

"unused" FurlFile - Name of file containing furling properties (quoted string) [unused when Furling=False]

----- TOWER -----

20 TwrNodes - Number of tower nodes used for analysis (-)

"DTU\_10MW\_ElastoDyn\_Tower.dat" TwrFile - Name of file containing tower properties (quoted string)

----- OUTPUT -----

True SumPrint - Print summary data to "<RootName>.sum" (flag)

1 OutFile - Switch to determine where output will be placed: {1: in module output file only; 2: in glue code output file only; 3: both} (currently unused)

True TabDelim - Use tab delimiters in text tabular output file? (flag) (currently unused)

"ES10.3E2" OutFmt - Format used for text tabular output (except time). Resulting field should be 10 characters. (quoted string) [not checked for validity!] (currently unused)

0.0 TStart - Time to begin tabular output (s) (currently unused)

1 DecFact - Decimation factor for tabular output {1: output every time step} (-) (currently unused)

0 NTwGages - Number of tower nodes that have strain gages for output [0 to 9] (-)

0 TwrGagNd - List of tower nodes that have strain gages [1 to TwrNodes] (-) [unused if NTwGages=0]

0 NBIGages - Number of blade nodes that have strain gages for output [0 to 9] (-)

BldGagNd - List of blade nodes that have strain gages [1 to BldNodes] (-) [unused if NBIGages=0]

OutList - The next line(s) contains a list of output parameters. See OutListParameters.xlsx for a listing of available output channels, (-)

"RotThrust, RotPwr "

"RotSpeed, BldPitch1, BldPitch3, BldPitch3"

END of input file (the word "END" must appear in the first 3 columns of this last OutList line)

## FAST InflowWind Input File

```
----- InflowWind v3.01.* INPUT FILE -----
Steady uniform wind inflow for DTU 10MW RWT offshore baseline turbine
-----
False Echo - Echo input data to <RootName>.ech (flag)
1 WindType - switch for wind file type (1=steady; 2=uniform; 3=binary TurbSim FF; 4=binary Bladed-
style FF; 5=HAWC format; 6=User defined)
0 PropogationDir - Direction of wind propogation (meteorological rotation from aligned with X (positive
rotates towards -Y) -- degrees)
1 NWindVel - Number of points to output the wind velocity (0 to 9)
0 WindVxiList - List of coordinates in the inertial X direction (m)
0 WindVyiList - List of coordinates in the inertial Y direction (m)
90 WindVziList - List of coordinates in the inertial Z direction (m)
== Parameters for Steady Wind Conditions [used only for WindType = 1] =====
11.4 HWindSpeed - Horizontal windspeed
119 RefHt - Reference height for horizontal wind speed
0 PLExp - Power law exponent
==Parameters for Uniform wind file [used only for WindType = 2] =====
"unused" Filename - Filename of time series data for uniform wind field.
90 RefHt - Reference height for horizontal wind speed
125.88 RefLength - Reference length for linear horizontal and vertical sheer
== Parameters for Binary TurbSim Full-Field files [used only for WindType = 3] =====
"Wind/08ms.wnd" Filename - Name of the Full field wind file to use (.bts)
==Parameters for Binary Bladed-style Full-Field files [used only for WindType = 4] =====
"unused" FilenameRoot - Rootname of the full-field wind file to use (.wnd,.sum)
False TowerFile - Have tower file (.twr) [flag]
==Parameters for HAWC-format binary files [Only used with WindType = 5] =====
"waspl\Output\basic_5u.bin" FileName_u - name of the file containing the u-component fluctuating wind
"waspl\Output\basic_5v.bin" FileName_v - name of the file containing the v-component fluctuating wind
"waspl\Output\basic_5w.bin" FileName_w - name of the file containing the w-component fluctuating wind
64 nx - number of grids in the x direction (in the 3 files above)
32 ny - number of grids in the y direction (in the 3 files above)
32 nz - number of grids in the z direction (in the 3 files above)
16 dx - distance (in meters) between points in the x direction
3 dy - distance (in meters) between points in the y direction
3 dz - distance (in meters) between points in the z direction
90 RefHt - reference height; the height (in meters) of the vertical center of the grid
----- Scaling parameters for turbulence -----
1 ScaleMethod - Turbulence scaling method [0 = none, 1 = direct scaling, 2 = calculate scaling factor based
on a desired standard deviation]
1 SFx - Turbulence scaling factor for the x direction (-) [ScaleMethod=1]
1 SFy - Turbulence scaling factor for the y direction (-) [ScaleMethod=1]
1 SFz - Turbulence scaling factor for the z direction (-) [ScaleMethod=1]
12 SigmaFx - Turbulence standard deviation to calculate scaling from in x direction (m/s) [ScaleMethod=2]
8 SigmaFy - Turbulence standard deviation to calculate scaling from in y direction (m/s) [ScaleMethod=2]
2 SigmaFz - Turbulence standard deviation to calculate scaling from in z direction (m/s) [ScaleMethod=2]
----- Mean wind profile parameters (added to HAWC-format files) -----
5 URef - Mean u-component wind speed at the reference height [m/s]
2 WindProfile - Wind profile type (0=constant;1=logarithmic,2=power law)
0 PLExp - Power law exponent [-] (used only when WindProfile=2)
0.03 Z0 - Surface roughness length [m] (used only when WindProfile=1)
=====OUTPUT=====
False SumPrint - Print summary data to <RootName>.Ifw.sum (flag)
OutList - The next line(s) contains a list of output parameters. See OutListParameters.xlsx for a listing
of available output channels, (-)
"Wind1VelX" X-direction wind velocity at point WindList(1)
END of input file (the word "END" must appear in the first 3 columns of this last OutList line)
-----
```